Modellering van interacties in het stralende nabije-veld voor de analyse van elektromagnetische compatibiliteit en draadloze vermogensoverdracht

Modeling of Radiative Near-Field Interactions for Electromagnetic Compatibility and Wireless Power Transfer Assessment

Gert-Jan Stockman

Promotoren: prof. dr. ir. D. Vande Ginste, prof. dr. ir. H. Rogier
Proefschrift ingediend tot het behalen van de graad van
Doctor in de ingenieurswetenschappen: elektrotechniek

Vakgroep Informatietechnologie
Voorzitter: prof. dr. ir. D. De Zutter
Faculteit Ingenieurswetenschappen en Architectuur
Academiejaar 2015 - 2016

UNIVERSITEIT GENT

ISBN 978-90-8578-918-5
NUR 959
Wettelijk depot: D/2016/10.500/50

Modeling of Radiative Near-Field Interactions for Electromagnetic Compatibility and Wireless Power Transfer Assessment

Gert-Jan Stockman

Dissertation submitted to obtain the academic degree of
Doctor of Electrical Engineering

Publicly defended at Ghent University on August 22, 2016

Supervisors

prof. dr. ir. Dries Vande Ginste
prof. dr. ir. Hendrik Rogier
Electromagnetics group
Department of Information Technology
Faculty of Engineering and Architecture
Ghent University
Technologiepark 15
B-9052 Zwijnaarde, Belgium
http://emweb.intec.ugent.be

Members of the examining board

prof. dr. ir. Rik Van de Walle (chairman)	Ghent University, Belgium
prof. dr. ir. Johan Bauwelinck (secretary)	Ghent University, Belgium
prof. dr. ir. Dries Vande Ginste (supervisor)	Ghent University, Belgium
prof. dr. ir. Hendrik Rogier (supervisor)	Ghent University, Belgium
prof. dr. ir. Flavio Canavero	Politecnico di Torino, Italy
prof. dr. ir. Davy Pissoort	University of Leuven, Belgium
prof. dr. ir. Jan Doutreloigne	Ghent University, Belgium

INTEC

UNIVERSITEIT GENT

Dankwoord

Toen ik mijn studies aan de universiteit aanving, leek het schrijven van een doctoraat verre toekomstmuziek. En toch ligt hier nu voor u, negen jaar later, het resultaat van vier jaar wetenschappelijk onderzoek aan de onderzoeksgroep Elektromagnetisme van de vakgroep Informatietechnologie aan de Universiteit Gent. Uiteraard is dit doctoraat de vrucht van heel wat doorzettingsvermogen, maar minstens even belangrijk zijn de hulp en steun die ik doorheen de jaren van tal van mensen heb mogen ervaren. Doorgaans ben ik een man van weinig woorden. Bij deze gelegenheid wil ik echter een uitzondering maken en enkele mensen persoonlijk bedanken. In het besef dat een dankwoord achteraf haast altijd onvolledig blijkt, wil ik vooreerst iedereen met wie ik ooit aangename contacten of interacties had oprecht bedanken.

In de eerste plaats zou ik graag mijn promotoren bedanken. Zij zijn in het prille begin samen met mij dit avontuur aangegaan en hebben mij bijgestaan tot het einde. Van Prof. dr. ir. Dries Vande Ginste heb ik veel geleerd, zowel op technisch als op praktisch vlak. Dries heeft dit werk zonder twijfel op vele aspecten naar een hoger niveau getild. Hij gaf me steeds de vrijheid mezelf te ontplooien in mijn eigen interessegebied. Dries was kordaat maar rechtvaardig en altijd bijzonder aangenaam in de omgang. Een betere promotor had ik me niet kunnen wensen. Ook bij Prof. dr. ir. Hendrik Rogier kon ik steeds terecht voor strategische input. Met zijn rijke kennis en ervaring in de academische wereld stuurde hij het onderzoek, waar nodig, in de goede richting. De waardevolle ideeën die Hendrik aanbracht hebben de kwaliteit van dit werk mee opgekrikt. Verder wil ik ook Prof. dr. ir. Daniël De Zutter bedanken om mij de kans te bieden onderzoek te verrichten in de hoogtechnologische omgeving die de vakgroep Informatietechnologie is.

Van al mijn collega's had ik het vaakst contact met Niels. Niels heeft een aparte stijl en zijn gevoel voor humor, enthousiasme, positiviteit en folkloristische gedachtegang maakten van hem mijn ideale partner in crime. Hij overtuigde mij om eindelijk het examen radioamateur af te leggen, wat een nieuwe wereld voor mij opende. Antennes bouwen, morsecode leren, satellieten contacteren, beurzen afschuimen, ... Samen vertoeven was steeds een plezier. Ook op professioneel vlak heeft Niels mij aangenaam verrast. Doorheen de vele discussies die we voerden over elektromagnetisme en elektronisch ontwerp heb ik zijn intelligentie mogen ontdekken. Bedankt, Niels, voor alle toffe momenten.

Martijn leerde ik oorspronkelijk kennen als mijn toenmalige thesisstudent. Later werd hij collega en uiteindelijk ook een goede vriend. Samen werden we de vrees van de onderzoeksgroep betreffende stijl en vormgeving van tekst en figuur. Zijn uitmuntende talenknobbel en ijzersterk geheugen vielen meteen op. Zelden heb

ik iemand ontmoet die elk moment uit zijn leven zo smakelijk en gedetailleerd kon navertellen alsof het gisteren was. Martijn bood telkens spontaan zijn hulp aan en bleek ook altijd zeer betrouwbaar. Martijn, oprecht bedankt voor alles.

Met Patrick maakte ik pas later kennis. Hij heeft een aanstekelijk enthousiasme en is erg gepassioneerd in alles wat hij onderneemt. Hij stond altijd klaar voor een goede babbel. Ook van zijn uitgebreide kennis omtrent elektronisch ontwerp heb ik veel kunnen opsteken. Minstens even waardevol waren zijn levenslessen en -verhalen. Ook buiten de werkuren hadden we vaak *contact* op onze vaste frequentie. Patrick, we horen elkaar zeker en vast nog. ON4CAZ DE ON7GLF TU FER ALL ES BEST 73 $\overline{\text{SK}}$ *dit dit*.

Graag wil ik ook de vijf collega's bedanken die ongeveer gelijktijdig met mij hun doctoraat startten en zullen beëindigen. De eerste met wie ik in contact kwam, destijds nog in het Technicum, was Giorgos. Giorgos heeft het met iedereen goed voor en kon, wanneer iets niet meer helemaal duidelijk was, klaarheid scheppen. Ook met Zdravko deelde ik al die jaren een bureau. Zdravko, we had many discussions about several aspects of work and life. You are truly a kindhearted and respectful person and you deserve all the best. I am convinced you will find your way. Sam Lemey heb ik altijd ervaren als een praktisch persoon die van aanpakken weet. Hij denkt vooral op lange termijn en dat komt zijn werk zeker ten goede. Bovenal vond ik Sam een aangenaam en grappig persoon. Ik wil hem bedanken voor de vele hulp die hij mij telkens weer geboden heeft. Verder bedank ik Thijs voor zijn sympathiek karakter en Marco voor de talrijke humoristische momenten.

Overigens wil ik de INTEC_design groep bedanken voor de boeiende tijd die ik er mocht doorbrengen. Tijdens de jaren dat ik er in de labo's heb vertoefd, heb ik een behoorlijk aantal waardevolle vaardigheden ontwikkeld en toffe mensen leren kennen. Daarom had ik in de eerste plaats graag Prof. dr. ir. Johan Bauwelinck bedankt voor de fijne samenwerking tijdens mijn periode aan de universiteit. Joris Van Kerrebrouck verdient een vermelding voor zijn spontane hulp, gastvrijheid en vrijgevigheid. Timothy De Keulenaer wil ik danken voor de interessante gesprekken, en Jan Gillis voor al zijn praktische hulp en amusante persoonlijkheid.

Verder betuig ik mijn oprechte dank aan Bart Spinnewyn. Als studiegenoten waren we uitermate complementair en hebben we elkaar door de soms zeer uitdagende materie geholpen. Niettegenstaande onze wegen op professioneel vlak gescheiden zijn, hebben we altijd contact gehouden en heeft onze vriendschap stand gehouden.

Vervolgens wil ik Isabelle Van der Elstraeten vernoemen, die ons steeds met de glimlach assisteerde en de complexiteit van administratieve kwesties op zich nam. Furthermore, I want to thank Nickolay for all our captivating discussions and the faith he has always had in me. Tim Besard wil ik bedanken voor de hulp bij computergerelateerde problemen en de decennialange vriendschap waarin hij mijn interesse voor zaken als hardware en programmeren al op vroege leeftijd prikkelde. Verder vermeld ik met droefheid wijlen de heer Guy Heylens die op de verdediging

van dit proefschrift beslist aanwezig zou geweest zijn. Tevens bedankt aan Patrick voor de eindeloze gastvrijheid et merci à Françoise pour les bons soins.

Wie zonder twijfel een grote rol spelen in dit verhaal zijn mijn ouders. Ze zijn heel verschillend, maar allebei intelligent op hun eigen manier. Investeren in kennis vinden ze uitermate waardevol, en daarover zaten ze dan ook steevast op dezelfde golflengte. Oprecht bedankt voor de jarenlange stimulans en ondersteuning. Het spreekt voor zich dat ik ook mijn zus, Astrid, en broer, Arno, wil bedanken voor de band die we hebben en hun onvoorwaardelijke steun.

Tenslotte bedank ik de persoon bij wie ik altijd mijzelf kan zijn en die mij permanent en pertinent steunt, zelfs in mijn soms niet-alledaagse hobby's. Eloïse, onze maat van liefde is liefde zonder maat. Met jou ziet de toekomst er zonnig en rooskleurig uit.

Gent, augustus 2016
Gert-Jan Stockman

We zijn zo jong, we zijn zo jong

Luc De Vos

Inhoudsopgave

Samenvatting

Het efficiënt modelleren van elektromagnetische interacties in en tussen elektronische systemen of apparaten is een belangrijk onderzoeksonderwerp dat al vele jaren onderzocht wordt. In dit werk wordt de aandacht gelegd op het efficiënt veldmodelleren van interacties in het stralende nabije-veld (Fresnelregio) en in het verre-veld (Fraunhoferregio). Dit onderzoek speelt een beduidende rol in de ontwikkeling van verscheidene elektronische applicaties. Twee belangrijke aspecten die onderzocht zullen worden in dit werk zijn de beoordeling van het elektromagnetische compatibiliteitsgedrag van elektronische producten en het modelleren van de efficiëntie van draadloze vermogensoverdrachtsystemen. In het algemeen zijn de voorgestelde technieken echter geschikt voor het modelleren van eender welke vorm van elektromagnetische interactie tussen apparaten tot in het stralende nabije-veld.

Omtrent de immuniteit en emissie van elektronische producten zijn diverse regelen wetgevende voorschriften opgesteld. Dergelijke voorschriften worden opgelegd om de elektromagnetische omgeving, waarin deze producten correct kunnen functioneren, te vrijwaren van storingen. Om na te gaan of een bepaald product aan de regels voldoet, worden zogenaamde compliancetesten uitgevoerd die de conformiteit van producten nagaan. In veel van deze testen wordt het product of het apparaat-onder-test in een (semi-)anechoïsche kamer geplaatst waar het elektromagnetische compatibiliteitsgedrag geobserveerd wordt voor verscheidene oriëntaties.

In het domein van elektromagnetische compatibiliteit is er nood aan zogenaamde pre-compliancetesten. Deze maken het namelijk mogelijk de uitkomst van een compliancetest te voorspellen, zonder ze effectief uit te voeren. Precompliancetesten zijn cruciaal gezien het feit dat compliancetesten niet goedkoop zijn, en deze dus idealiter slechts een keer uitgevoerd worden. Bijgevolg zouden potentiële elektromagnetische compatibiliteitsproblemen al opgespoord moeten worden alvorens een compliancetest aan te vangen. Wanneer elektromagnetische compatibiliteitsproblemen pas ontdekt worden in de compliancefase van het ontwerpproces kan dit aanzienlijk duur uitvallen voor een onderneming. Als dit voorvalt, wordt men opnieuw geconfronteerd met ontwerpkosten, testkosten, fabricagekosten en debugtijd. Dit vertraagt de marktintroductietijd van het product wezenlijk en kan zelfs fataal zijn voor bepaalde ondernemingen. Het is dus van het uiterste belang pre-compliancetesten reeds uit te voeren gedurende de eerste fases van het ontwerpproces van een nieuw elektronisch product of systeem.

Er bestaan meettechnieken die toelaten een compliancetest na te bootsen. Hoewel deze metingen door de ontwerpers zelf uitgevoerd kunnen worden (in tegen-

stelling tot metingen in een gecertificeerd elektromagnetische compatibiliteitslab), blijven ze relatief gezien duur en vereisen ze fysieke prototypes, wat niet het geval is wanneer simulaties aangewend worden. Betreurenswaardig zijn veldsimulaties, voornamelijk voor complexe producten, bijzonder tijdrovend. Om metingen na te bootsen in simulatie, en indachtig dat het apparaat-onder-test geroteerd wordt over alle mogelijke hoeken tijdens een compliancetest, moeten telkens volledig nieuwe simulaties uitgevoerd worden voor elke heroriëntering. Dit brengt een hoge computationele kost met zich mee, waardoor dit proces al snel onhandelbaar wordt voor de ontwerper. Aangezien er een onmiskenbare behoefte is aan een snelle en accurate simulatietechniek, wordt er in dit doctoraatsonderzoek bijgevolg een nieuwe methode ontwikkeld die dit probleem aanpakt.

Het formalisme van de nieuwe techniek kan op de volgende manier samengevat worden. Door gebruik te maken van een additietheorema voor de drie-dimensionale Greense functie, samen met een expansie in vlakke golven, kan de interactie tussen apparaten beschreven worden in functie van hun stralingspatronen. Dit laat toe een potentieel zeer complexe geometrie te vervangen door zijn, minder complex, stralingspatroon. De benaderingen die gebruikt worden in dit proces leiden tot een techniek die geldig en accuraat blijft tot in het stralende nabije-veld. Een verdere complexiteitsreductie wordt gerealiseerd door de stralingspatronen te ontbinden in sferische harmonieken. Het probleem waar commerciële veldsimulatoren mee kampen, namelijk dat er voor elke heroriëntatie een compleet nieuwe simulatie uitgevoerd dient te worden, wordt vermeden door deze ontbinding in harmonieken. De transformatie die de stralingspatronen van de apparaten-ondertest omzet van het spatiale- naar het sferischeharmoniekendomein en terug, brengt een veel lagere computationele kost met zich mee. Verder kan het draaien van de apparaten – of meer specifiek van hun stralingspatronen – in het sferischeharmoniekendomein zeer efficiënt gebeuren door gebruik te maken van Wigner-D matrices. Bijgevolg reduceert de voorgestelde methode de simulatietijd van compliancetesten significant.

In het eerste deel van dit werk wordt het formalisme uitgewerkt voor éénpoortsapparaten in zowel anechoïsche als semi-anechoïsche condities. Verder wordt een extensie gemaakt naar tests met meerdere stoorbronnen. Vervolgens breiden we het werk verder uit voor toepassingen op meer complexe, realistische producten door rekening te houden met interacties tussen multipoortapparaten. Dit leidt tot een compleet formalisme dat niet alleen het *inter*-systeem elektromagnetische compatibiliteitsgedrag kan bepalen, maar ook zijn *intra*-systeem tegenhanger. Een combinatie van deze aangewende technieken laat toe complexe, realistische producten te testen in de vroege fases van het ontwerpproces, wat de ontwerper een krachtig instrument geeft om zo vroeg mogelijk elektromagnetische compatibiliteitsproblemen op te sporen. De accuraatheid van de beschreven methode wordt gevalideerd (in meting en simulatie) door gebruik te maken van verscheidene applicatie- en validatievoorbeelden. Verder wordt de simulatietijd sterk gereduceerd, wat de ontwerper helpt in het efficiënt uitvoeren van pre-compliancetesten.

De hierboven beschreven aanpak laat het efficiënt modelleren van elektromagnetische interacties tot in het stralende nabije-veld toe. De efficiëntie van deze methode komt volledig tot zijn recht wanneer interagerende apparaten of systemen worden geherpositioneerd of geheroriënteerd. Vandaar dat deze aanpak ook zijn toepasbaarheid aantoont in andere domeinen, zoals bij het ontwerp van draadloze vermogensoverdrachtsystemen. In deze systemen worden apparaten (zoals sensornetwerken) elektrisch gevoed door gebruik te maken van de elektromagnetische energie, uitgestraald door een zendantenne. Door het vermogen draadloos te leveren, zijn voedingsdraden niet langer nodig, wat meer flexibiliteit biedt aan het product. De uitgestraalde energie wordt typisch opgevangen door een ontvangstantenne en vervolgens omgezet van wisselstroom naar gelijkstroom. Er bestaan verscheidene scenarios waarin de apparaten (die gevoed dienen te worden, of de zendantenne zelf) onderworpen worden aan translatie of rotatie, wat het nieuwe formalisme zeer geschikt maakt om de totale efficiëntie van dergelijke draadloze vermogensoverdrachtsystemen te voorspellen. Het laat ontwerpers toe te begroten of een ontvangstapparaat al dan niet voldoende vermogen zal ontvangen, wat beter inzicht biedt in het ontwerp en de ontwerpmethodologie vereenvoudigt.

In het tweede deel van dit werk wordt bijgevolg de nieuwe modelleertechniek gecombineerd met circuit- en antennetheorie, zodat de efficiëntie van complete draadloze vermogensoverdrachtsystemen, van de wisselstroom aan de zendantenne naar de gelijkstroom aan de ontvangstzijde, accuraat gemodelleerd kan worden. Dit proces omvat bovendien het correct omgaan met de niet-lineariteiten in het systeem die typisch geïntroduceerd worden door de spanningsverdubbelaar en gelijkrichter in de ontvanger, en als doel hebben de wisselstroom om te zetten naar gelijkstroom. Opnieuw wordt de hoge efficiëntie en accuraatheid van de voorgestelde techniek aangetoond door gebruik te maken van praktische applicatie- en validatievoorbeelden. Dit bewijst bijgevolg ook de toepasbaarheid van deze methode als een simulatietechniek voor ontwerpers van draadloze vermogensoverdrachtsystemen.

Summary

The efficient modeling of electromagnetic interactions in an electronic system or between devices is an important research topic that has been investigated for many years. In this work, we focus on the efficient full-wave modeling of interactions in the radiative near-field (Fresnel region) and in the far-field (Fraunhofer region). This research plays an important role in the development of several electronic applications. Two important aspects that will be discussed in this dissertation are the assessment of Electromagnetic Compatibility (EMC) behavior and the modeling of the efficiency of a Wireless Power Transfer (WPT) system, though in general, the proposed techniques are suitable for modeling any form of electromagnetic interaction between devices up until the radiative near-field.

Many regulatory and legislative rules have been put into place with regard to the immunity and emission of electronic products. These are imposed in order to preserve an electromagnetic environment in which electronic applications can function satisfactorily. To verify that a certain product abides by these rules, compliance testing is performed. In many of these tests, the product or Device Under Test (DUT), is placed in a (semi-)anechoic chamber where the EMC behavior is observed for different orientations of the DUT.

In the field of EMC, there is also a need for so-called *pre*-compliance testing. This is a way of predicting the outcome of a compliance test, without actually performing this test physically. Pre-compliance testing is crucial since compliance tests are not cheap and should therefore ideally have to be performed only once. Consequently, potential EMC problems should already have been tracked down before attempting a compliance test. Finding out about EMC problems only in this testing stage of the process can be very expensive for a company in terms of re-design costs, re-testing costs, re-manufacturing costs and debugging time. This will delay the time-to-market substantially and could eventually be deadly for certain enterprises. It is thus of paramount importance to perform pre-compliance testing already during the early design stages of a novel product or system.

Measurement techniques exist that try to mimic a compliance test. Although these measurements can be performed by the designers (as opposed to in a certified EMC lab), they are still relatively expensive and require physical prototypes to be manufactured. When leveraging simulations, these problems do not occur. Unfortunately, performing full-wave simulations, especially for complex products, can be very time-consuming. To mimic this in simulation, keeping in mind that the DUT is rotated over all possible angles during a compliance test, a completely new simulation has to be performed for every reorientation of the DUT, which implies a high computational complexity. This process becomes rapidly untractable for the

designer. As there is a clear need for a simulation technique that is fast as well as accurate, in the present doctoral research, a novel method was developed that tackles this problem.

The formalism of the novel technique can be summarized as follows. Using an addition theorem for the three-dimensional Greens function, together with an expansion into plane waves, the interaction between devices is described in terms of their radiation patterns. This allows to replace a potentially very complex geometry by its, less complex, radiation pattern. The approximations used in this process lead to a technique that is still valid and accurate up until the radiative near-field. A further complexity reduction is made by expanding the radiation patterns into spherical harmonics. This expansion is performed to cope with the issue that commercial full-wave solvers struggle with, i.e. for every reorientation, a completely new simulation is required. The transformation of the radiation patterns of the DUTs, from the spatial domain to the spherical harmonics domain and back, do not entail a high computational cost. Furthermore, rotating the devices – or more specifically their radiation patterns – in the spherical harmonics domain is performed very efficiently by making use of Wigner-D matrices. Consequently, the proposed novel approach significantly reduces the simulation time of a compliance test.

In Part I of this work, this formalism is elaborated for *single*port devices in anechoic as well as semi-anechoic conditions. Moreover, an extension is made to account for multiple non-collocated noise sources, as found in certain compliance tests. Next, we extend the work to be applicable to more complex, real-world products by accounting for interactions between *multi*port devices. This leads to a complete formalism that does not only allow for the assessment of *inter*-system EMC behavior, but also for its *intra*-system counterpart. Combination of the advocated techniques allows complex real-life products to be tested in the early design phase, providing the designer with a powerful tool to track down EMC problems as early as possible. The accuracy of the described method has been validated (in measurement and simulation), using several practical application and validation examples. Additionally, a highly improved simulation speed has been obtained, aiding the designer in efficient pre-compliance testing.

The approach described above allows the efficient modeling of electromagnetic interactions up until the radiative near-field. The efficiency of the method is fully appreciated when interacting devices or systems are being repositioned or reoriented. Hence, this approach has shown its appositeness in other domains as well, such as in the design of WPT systems. In WPT systems, devices (such as sensor networks) are being powered using electromagnetic energy radiated by a transmitting antenna. By providing power wirelessly, the need for power cabling is removed, allowing for more flexibility. Typically, the radiated energy is captured by a receiving antenna and is subsequently converted from Alternating Current (AC) to Direct Current (DC). Many scenarios exist where the devices that need to be powered or the transmitting antenna itself are subject to translation or rotation, making our

formalism very suitable to predict the total efficiency of such a WPT system. It allows designers to predict whether the receiving device will obtain enough power, yielding significant insight and facilitating the design methodology.

Therefore, in Part II of this work, the novel modeling technique is combined with circuit and antenna theory, such that the efficiency of a complete WPT link (from the transmitting antenna's AC power to the DC power of the receiving device) is accurately modeled. This process also involves appropriately dealing with the nonlinearities in the system, typically stemming from the voltage doubler and rectifier circuit connected to the receiving antenna, which converts AC into DC power. Once again, using practical application and validation examples, the high efficiency and accuracy of the proposed technique is demonstrated, also showing its appositeness as a simulation tool for designers of WPT systems.

List of Abbreviations

AC	Alternating Current
ADS	Advanced Design System
CST MWS	Computer Simulation Technology Microwave Studio
CW	Continuous Wave
DC	Direct Current
DDM	Domain Decomposition Method
DUT	Device Under Test
EFIE	Electric Field Integral Equation
EM	electromagnetic
EMC	Electromagnetic Compatibility
EMI	Electromagnetic Interference
FDTD	Finite-Difference Time-Domain
FE	Finite Element
HB	Harmonic Balance
IC	Integrated Circuit
ISM	Industrial, Scientific and Medical
MIMO	Multiple-Input Multiple-Output
MoM	Method of Moments
MU	Mobile User
PCB	Printed Circuit Board
PEC	Perfect Electric Conductor
PO	Physical Optics
PTE	Power Transfer Efficiency
RF	Radio Frequency
RFID	Radio Frequency Identification
SE	Shielding Efficiency
SGH	Standard Gain Horn
SIW	Substrate Integrated Waveguide
SRM	Source Reconstruction Method
VNA	Vector Network Analyzer
WPT	Wireless Power Transfer

List of Symbols

General

$\mathcal{O}$	origin
j	imaginary unit
Ω	Ewald sphere
$\mathcal{I}$	unit dyadic
θ	inclination angle
ϕ	azimuthal angle
L	determines the number of multipoles
P	determines the number of spherical harmonics

Electromagnetic field and properties

f	frequency
ω	angular frequency
λ	wavelength
$\mathbf{r}$, $\mathbf{r}'$	position vector
$\mathbf{j}$	current density vector
$\mathbf{e}$	electric field vector
$\mathbf{h}$	magnetic field vector
ϵ	permittivity
μ	permeability
k	wave number
$\mathbf{k}$	wave vector
Z	characteristic impedance of free space

Special functions

$\mathcal{G}(\cdot,\cdot)$	dyadic Green's function
$j_l(\cdot)$	l-th order spherical Bessel function of the first kind
$h_l^{(2)}(\cdot)$	l-th order spherical Hankel function of the second kind
$P_l(\cdot)$	Legendre polynomial of degree l
$Y_{pq}(\cdot)$	orthornomalized scalar spherical harmonic of degree p and order q
$P_p^q(\cdot)$	associated Legendre polynomial of degree p and order q
$T(\cdot)$	translation operator

Circuit and antenna theory

V_g	generator voltage
Z_g	generator impedance
Z_L	load impedance
I_{sc}	short-circuit current
$\mathbf{F}(\cdot)$	radiation pattern
$\mathbf{F}^{(\cdot)}(\cdot)$	embedded radiation pattern
$\mathbf{F}^{(\cdot),a}(\cdot)$	active radiation pattern

Spherical harmonics

A_{pq}, B_{pq}	spherical harmonics coefficients
$\mathcal{R}$	rotation in the spatial domain
$\mathcal{R}_{\mathrm{SH}}$	rotation in the spherical harmonics domain
$\mathcal{F}$	spherical harmonics expansion
$\mathcal{F}^{-1}$	inverse spherical harmonics expansion
d^r_{pq}	Wigner small d-matrix
D^r_{pq}	Wigner D-matrix
α, β, γ	Euler angles

List of Publications

Articles in international journals

- M. Rossi, G.-J. Stockman, H. Rogier and D. Vande Ginste, "Stochastic analysis of the efficiency of a wireless power transfer system subject to antenna variability and position uncertainties," *Sensors*, vol. 7, Jul. 2016.
- G.-J. Stockman, S. Lemey, H. Rogier and D. Vande Ginste, "Full-wave modeling of interacting multiport devices with arbitrary relative positions and orientations for efficient EMI assessment," *IEEE Transactions on Electromagnetic Compatibility*, vol. 58, no. 4, pp. 1322–1330, Jun. 2016.
- G.-J. Stockman, H. Rogier and D. Vande Ginste, "Dedicated model for the efficient assessment of wireless power transfer in the radiative near-field," *International Journal of Numerical Modelling: Electronic Networks, Devices and Fields*, vol. 29, pp. 380–391, May 2016.
- G.-J. Stockman, H. Rogier and D. Vande Ginste, "Efficient modeling of interactions between radiating devices with arbitrary relative positions and orientations," *IEEE Transactions on Electromagnetic Compatibility*, vol. 56, no. 6, pp. 1313–1321, Dec. 2014.
- A. Dierck, S. Agneessens, F. Declercq, B. Spinnewyn, G.-J. Stockman, P. Van Torre, L. Vallozzi, D. Vande Ginste, J. Vanfleteren, T. Vervust and H. Rogier, "Active textile antennas in professional garments for sensing, localisation and communication," *International Journal of Microwave and Wireless Technologies*, vol. 6, pp. 331–341, Mar. 2014.
- S. Agneessens, P. Van Torre, F. Declercq, B. Spinnewyn, G.-J. Stockman, H. Rogier and D. Vande Ginste, "Design of a wearable, low-cost, through-wall Doppler radar system," *International Journal of Antennas and Propagation*, Special Issue on Conformal Antennas, Article ID 840924, 9 pages, 2012.

Articles in conference proceedings

- G.-J. Stockman, H. Rogier and D. Vande Ginste, "Efficient full-wave modeling of electromagnetic interference in the presence of multiple non-collocated noise sources," *International Conference on Electromagnetics in Advanced Applications (ICEAA 2015)*, Turin, Italy, pp. 175–178, Sep. 2015.

- G.-J. Stockman, H. Rogier and D. Vande Ginste, "Efficient full-wave modeling of radiative near-field interactions in semi-anechoic conditions," *IEEE International Symposium on Electromagnetic Compatibility and EMC Europe (EMC 2015)*, Dresden, Germany, pp. 524–528, Aug. 2015.

- G.-J. Stockman, D. Vande Ginste and H. Rogier, "Efficient modeling of the wireless power transfer efficiency for varying positions and orientations between transmitter and receiver," *IEEE MTT-S International Conference on Numerical Electromagnetic and Multiphysics Modeling and Optimization (NEMO 2015)*, Ottawa, Canada pp. 1–3, Aug. 2015.

- M. Huynen, G.-J. Stockman, F. Declercq, G. Torfs, J. Bauwelinck and D. Vande Ginste, "EMC-aware analysis and design of a low-cost receiver circuit under injection locking and pulling," *IEEE Electrical Design of Advanced Packaging and Systems Symposium (EDAPS 2014)*, Bangalore, India, pp. 121–124, Dec. 2014.

- H. Rogier, S. Agneessens, A. Dierck, B. Spinnewyn, G.-J. Stockman, F. Declercq, P. Van Torre, L. Vallozzi and D. Vande Ginste, "Active textile antennas in professional garments for sensing, localisation and communication," *43rd European Microwave Conference (EuMC)*, Nuremberg, Germany, pp. 850–853, Oct. 2013.

- S. Agneessens, P. Van Torre, F. Declercq, B. Spinnewyn, G.-J. Stockman, H. Rogier and D. Vande Ginste, "A through wall Doppler radar system: active textile antenna design, prototyping and experiment," *IEEE Topical Conference on Wireless Sensors and Sensor Networks (WiSNet 2013)*, Austin, Texas, USA, pp. 16–18, Jan. 2013.

Scientific awards

- Best Poster Award (2nd prize) for the poster entitled "Efficient Modeling of the Wireless Power Transfer Efficiency for Varying Positions and Orientations between Transmitter and Receiver," presented at the *URSI/NARF/IEEE AP-S Joint Symposium*, Twente, Netherlands, Dec. 2015.

- IMEC master's thesis award for the best master thesis in engineering for the work entitled "Design of a coherent optical receiver for passive optical access networks", 2012.

Modeling of Radiative Near-Field Interactions for Electromagnetic Compatibility and Wireless Power Transfer Assessment

1 Introduction

Context

Since the invention of the transistor in the 1940s, the field of electronics has grown exponentially. Additionally, the development of Integrated Circuits (ICs) (1960s), and later on microprocessors (1970s), brought momentum to the field of digital electronics. Nowadays, electronic systems almost always consist of a combination of analog and digital parts. This symbiosis has driven technology to what we know today and has paved the way to advanced applications, improving the quality of life for people all over the world. As applications become more advanced, the design complexity of these systems increases as well. One important aspect in this regard is the data rate of a system. Since the first wired communication link set up by Samuel Morse in the mid-19th century and the first wireless link set up by Guglielmo Marconi late-19th century, engineers have always been looking for ways to increase the rate of wired/wireless data transmission to serve the demands of emerging applications. In practice, this is done by increasing the bandwidth and operating frequency of the electrical systems.

As the operating frequency and bandwidth of electronic applications increased over time, the design methodology of these systems changed. Whereas previously the design used to rely entirely on circuit theory, we have gradually moved to a more hybrid approach combining conventional circuit theory with full-wave simulations. Thereto, designers apply a divide-and-conquer technique in which the circuit is subdivided into parts that can be handled by circuit solvers, relying on Kirchoff's voltage and current laws, and parts that are treated by full-wave solvers [1]. These solvers take the geometry of the circuit or system into account and find the solution of Maxwell's equations for the problem at hand. The advantage is their improved accuracy compared to conventional circuit solvers, which becomes more apparent as the frequency increases. This improved accuracy leads to a better prediction of

the behavior of electronic designs. Prototyping of high-frequency designs is costly, implying the need for such correct predictions in simulation. The downside of these solvers is immediately clear and is found in their complexity and the computational cost to perform full-wave simulations. Using these solvers in an efficient way and making sure that results are correct and reliable has become an art in itself. Electrical engineers need a lot of experience to use these electromagnetic full-wave solvers to their advantage and to correctly interpret the simulation results.

Motivation

With electronic applications being ubiquitous in today's world, it is important to maintain an environment in which electronic products can operate satisfactorily and make sure that their Electromagnetic Compatibility (EMC) behavior is acceptable. Every electronic circuit emits electromagnetic energy which can be picked up by other circuits that are consequently getting disturbed by it. To cope with interference between electronic products, legislative and regulatory requirements have been proposed that limit the emission of devices and at the same time enforce devices to possess a certain degree of immunity against electromagnetic radiation. In order to check if an electronic product meets these compliance requirements, radiation tests are performed in an anechoic or semi-anechoic chamber. In these tests, the Device Under Test (DUT) is illuminated by an antenna to measure the immunity of the device or the radiation originating from the DUT is picked up by a receive antenna. This is done while rotating the DUT such that the EMC behavior is analyzed for all angles. In case of a failed compliance test, i.e. when immunity and/or emission do not meet the standards, the product is rejected and cannot be used or sold. This entails huge consequences for project timelines and budgets. Debugging, re-design, re-manufacturing and re-testing are very costly and unsettle the time-to-market schedule.

To avoid these situations, pre-compliance testing can be performed. In pre-compliance testing, a full compliance lab is mimicked in measurement or simulation. Assuming an efficient model could be developed to predict the actual compliance test, would allow the designer to use it early in the design phase of a product. The advantage of performing pre-compliance testing in the early design phase is that EMC problems are much easier to fix when caught early on. The goal is to predict and solve all potential EMC problems before tape-out, prototyping and, especially, production, in order to arrive at a so-called "first-time-right design".

Considering the interaction between two (or more) separate devices or systems is denoted as an *inter*-system EMC problem. Another important aspect for designers of electrical systems is the *intra*-system EMC behavior. It is not guaranteed that a system, consisting of several sub-systems who all individually meet the EMC requirements, will be free of EMC problems when these subsystems are combined. In particular when the several subsystems are positioned physically close to one

another, interaction between them may degrade the overall system performance. Therefore, an efficient method to model the electromagnetic interaction between devices, systems and subsystems is required, which also allows to accurately and efficiently predict the (inter- or intra-system) EMC behavior when the devices or (sub)systems are in close proximity of each other.

When interactions between devices can be modeled efficiently, this technique is immediately applicable to many other domains as well. One such domain is the design of Wireless Power Transfer (WPT) systems where energy is transmitted wirelessly to, e.g., a sensor network without the need of power cabling. The design of WPT systems is of increasing importance and it is predicted that in the near future, an almost unlimited number of monitoring aplications – structural health, logistics, security, health care and agriculture to name only a few – will require large-scale development of cooperative wireless microsystems with sensing capabilities [2]. Combining the developed electromagnetic interaction modeling formalism to efficiently predict the efficiency of the wireless link between devices, i.e. antennas, in WPT systems, together with circuit and antenna theory (which takes the conversion from Alternating Current (AC) to Direct Current (DC) power into account) leads to a complete characterization of the transmitted AC to received DC power.

Predicting the WPT link efficiency is already possible by using commercial full-wave solvers. These can perform accurate predictions, but as stated before, their disadvantage is the high computational cost they entail. Especially when some of the devices in the system are being rotated or translated, a new simulation of the complete domain is needed for every repositioning or reorientation. This situation is similar to an EMC test where the DUT is rotated over a complete sphere. Hence, leveraging (commercial) full-wave solvers is not convenient for quick testing in the early design phase, where a lot of configurations are required to be tested. Again, in the context of WPT, it would thus be beneficial to develop a formalism that allows to efficiently take repositioning or reorientation into account. Furthermore, to be usable for WPT link assessment, the technique should not only be valid in the far-field (Fraunhofer region), but also up until the radiative near-field (Fresnel region).

State-of-the-art

In the world of computational electromagnetics, several numerical techniques already exist that relax the high computational requirements of the above described problems. To analyze emission, equivalent model or model-reduction techniques can be used [3], [4], and when looking at susceptibility, various hybrid techniques have been proposed. These techniques can, for example, combine full-wave methods with model-reduction techniques [5], [6] or use an extended S-parameter model [7], [8]. Another possibility is by making use of Domain Decomposition Methods (DDMs). These methods solve a complex problem by dividing it into several simpler subproblems. These subproblems are individually treated, each in

the most efficient way, after which the results are recombined to assess the global behavior of the problem [9]–[13].

In the domain of WPT, the research is divided into three groups, based on the distance between the devices in the WPT system. When devices are located very close to each other, i.e. in each other's reactive near-field, an often used method to determine the Power Transfer Efficiency (PTE) is the coupled mode theory. In the region of coupled mode resonance, coupling between devices is strong and thus a high PTE can be obtained [14]–[19]. For devices positioned in each other's radiative near-field (or Fresnel region), which is beyond the coupled mode resonance region, the PTE decreases rapidly with distance. The coupling is much weaker in this region and can be modeled by using a spherical mode expansion [20]. When the devices are spaced far apart, i.e., in each other's far-field (or Fraunhofer region), the PTE is modeled using the traditional Friis formula [21]. Orientation dependence of these systems is then alleviated by designing circularly polarized antennas. The question remains if this far-field approach is still suitable when the antennas are brought into the near-field region [16].

Novel contributions and outline of this work

The goal of this work is to develop an efficient formalism to model electromagnetic interactions between devices or systems. This method should be computationally inexpensive, accurate, and applicable up until the radiative near-field (Fresnel region). In this way the method can be used to model for example the EMC behavior of systems, or to predict the link efficiency of a WPT system.

This dissertation consists of two parts, each focusing on different applications where efficient modeling of electromagnetic interaction is needed. In the first part a solution is proposed to aid pre-compliance testing and predicting EMC behavior. This method mimics EMC tests performed in (semi-)anechoic chambers and predicts the results with high accuracy and low computational cost. Furthermore, it is also applicable for characterizing the intra-system EMC behavior of complex electronic products. The second part of this work tackles the problem of modeling the WPT link efficiency as used in systems to wirelessly power sensor networks. Applying our methodology to this field allows designers of such systems to easily predict the performance of their WPT system.

In more detail, Part I of this thesis focuses on the efficient modeling of inter- and intra-system EMC behavior. In Chapter 2, the general formalism is explained for the simple case of two one-port devices in an anechoic chamber. In this approach, making use of an addition theorem and an expansion into plane waves, the complex geometries of devices in the test are represented by their radiation patterns, reducing the complexity of the problem. Moreover, the radiation patterns themselves are expanded into spherical harmonics. The set of spherical harmonics coefficients can be efficiently rotated, using Wigner-D matrices, allowing to mimic rotations of the devices without additional computational cost. Translations are

possible by making use of the translation operator which also appears in the formalism. Combination of these two features leads to modeling of the interaction between devices with arbitrary relative positions and orientations. After an initial setup, i.e., after obtaining the radiation patterns of the devices in the system (either by simulation or measurement), a pre-compliance test is now efficiently mimicked. Subsequently, in Chapter 3 this formalism is extended to account for multiple non-collocated noise sources in an EMC test. In Chapter 4, by making use of image theory, the extension to tests in semi-anechoic conditions is made. Finally, in Chapter 5, the formalism is reworked to analyze complex multiport circuits such as complete Printed Circuit Boards (PCBs). Thereto, new definitions of radiation patterns for multiports are introduced. These definitions allow to reuse the efficient spherical harmonics strategy and the Wigner-D matrices, as explained in Chapter 2. Using a validation example it is shown that this method indeed yields efficient modeling of potential EMC problems in a real-life scenario.

In Part II, the formalism elaborated in Part I is extended to be of use in a WPT system design environment. The technique is valid up until the radiative near-field, allowing to model devices in close proximity, as is often the case in WPT systems. In Chapter 6, the methodology is combined with circuit theory, describing the aspect of power conversion from AC to DC power. This method is validated and subsequently used to model a real-world application. In Chapter 7, and similar to what was explained in Chapter 2, rotations are included to comply with the study of WPT systems where the devices in the system are reoriented in space.

Finally, the general conclusions and future work are presented in Chapter 8. All of the above mentioned work has been published in international peer-reviewed journals or has been presented at international conferences. Although the underlying theory is sufficiently referenced, the work assumes a basic knowledge in circuit and antenna theory and electromagnetic fields. For further readings on these subjects, we refer to [22], [23] and [24], respectively.

References

[1] D. De Zutter, J. Sercu, T. Dhaene, J. D. Geest, F. J. Demuynck, S. Hammadi, and C. W. Paul, "Recent trends in the integration of circuit optimization and full-wave electromagnetic analysis", *IEEE Transactions on Microwave Theory and Techniques*, vol. 52, no. 1, pp. 245–256, Jan. 2004.

[2] A. Costanzo and D. Masotti, "Smart solutions in smart spaces: Getting the most from far-field wireless power transfer", *IEEE Microwave Magazine*, vol. 17, no. 5, pp. 30–45, May 2016.

[3] P. Li and L. J. Jiang, "Source reconstruction method-based radiated emission characterization for PCBs", *IEEE Transactions on Electromagnetic Compatibility*, vol. 55, no. 5, pp. 933–940, Oct. 2013.

[4] P. Kralicek, W. John, R. De Smedt, K. Vervoort, and H. Garbe, "A voltage controlled emission model of electromagnetic emission of IC for system analysis", in *IEEE International Symposium on Electromagnetic Compatibility*, Montreal, Quebec, 13-17 Aug. 2001, pp. 1197–1202.

[5] I. Erdin, M. Nakhla, and R. Achar, "Circuit analysis of electromagnetic radiation and field coupling effects for networks with embedded full-wave modules", *IEEE Transactions on Electromagnetic Compatibility*, vol. 42, no. 4, pp. 449–460, Nov. 2000.

[6] M. Tang, J. Lu, J. Mao, and L. Jiang, "A systematic electromagnetic-circuit method for EMI analysis of coupled interconnects on dispersive dielectrics", *IEEE Transactions on Microwave Theory and Techniques*, vol. 61, no. 1, pp. 1–13, Jan. 2013.

[7] Y. Bayram and J. Volakis, "Hybrid S-parameters for transmission line networks with linear/nonlinear load terminations subject to arbitrary excitations", *IEEE Transactions on Microwave Theory and Techniques*, vol. 55, no. 5, pp. 941–950, May 2007.

[8] Z. Khan, Y. Bayram, and J. Volakis, "EMI/EMC analysis of printed circuit boards subject to near-zone illuminations", *IEEE Transactions on Electromagnetic Compatibility*, vol. 51, no. 2, pp. 406–408, May 2009.

[9] Y. Shao, Z. Peng, and J.-F. Lee, "Signal integrity analysis of high-speed interconnects by using nonconformal domain decomposition method", *IEEE Transactions on Components, Packaging and Manufacturing Technology*, vol. 2, no. 1, pp. 122–130, Jan. 2012.

[10] Z. Peng, K.-H. Lim, and J.-F. Lee, "Nonconformal domain decomposition methods for solving large multiscale electromagnetic scattering problems", *Proceedings of the IEEE,* vol. 101, no. 2, pp. 298–319, Feb. 2013.

[11] C. Della Giovampaola, E. Martini, A. Toccafondi, and S. Maci, "A hybrid PO/generalized-scattering-matrix approach for estimating the reflector induced mismatch", *IEEE Transactions on Antennas and Propagation*, vol. 60, no. 9, pp. 4316–4325, Sep. 2012.

[12] T. Flisgen, H. Glock, and U. Van Rienen, "Compact time-domain models of complex RF structures based on the real eigenmodes of segments", *IEEE Transactions on Microwave Theory and Techniques*, vol. 61, no. 6, pp. 2282–2294, Jun. 2013.

[13] H. Wu and A. Cangellaris, "A finite-element domain-decomposition methodology for electromagnetic modeling of multilayer high-speed interconnects", *IEEE Transactions on Advanced Packaging*, vol. 31, no. 2, pp. 339–350, May 2008.

[14] I.-J. Yoon and H. Ling, "Investigation of near-field wireless power transfer under multiple transmitters", *IEEE Antennas and Wireless Propagation Letters*, vol. 10, pp. 662–665, 2011.

[15] ——, "Investigation of near-field wireless power transfer in the presence of lossy dielectric materials", *IEEE Transactions on Antennas and Propagation*, vol. 61, no. 1, pp. 482–488, Jan. 2013.

[16] ——, "Design of an electrically small circularly polarised turnstile antenna and its application to near-field wireless power transfer", *IET Microwaves, Antennas Propagation*, vol. 8, no. 5, pp. 308–314, Apr. 2014.

[17] K. Fotopoulou and B. Flynn, "Wireless power transfer in loosely coupled links: Coil misalignment model", *IEEE Transactions on Magnetics*, vol. 47, no. 2, pp. 416–430, Feb. 2011.

[18] B. Cannon, J. Hoburg, D. Stancil, and S. Goldstein, "Magnetic resonant coupling as a potential means for wireless power transfer to multiple small receivers", *IEEE Transactions on Power Electronics*, vol. 24, no. 7, pp. 1819–1825, Jul. 2009.

[19] A. Kurs, R. Moffatt, and M. Soljacic, "Simultaneous mid-range power transfer to multiple devices", *Applied Physics Letters*, vol. 96, no. 4, pp. 044 102–044102–3, Jan. 2010.

[20] J. Lee and S. Nam, "Fundamental aspects of near-field coupling small antennas for wireless power transfer", *IEEE Transactions on Antennas and Propagation*, vol. 58, no. 11, pp. 3442–3449, Nov. 2010.

[21] C. Balanis, *Antenna theory: Analysis and design*. Wiley, 1982.

[22] D. Pozar, *Microwave Engineering*. Wiley, 2004.

[23] C. Balanis, *Antenna Theory: Analysis and Design*. John Wiley & Sons, 2005.

[24] J. Van Bladel, *Electromagnetic Fields*. John Wiley & Sons, 2007.

Part I

Modeling of Electromagnetic Compatibility Behavior

To facilitate pre-compliance testing, there is a need for efficient modeling tools that describe the Electromagnetic Compatibility (EMC) behavior of electronic products, allowing the designer to detect potential EMC problems early in the design phase. In this part, we develop a formalism that efficiently models electromagnetic interactions up until the radiative near-field. In Chapter 2 the formalism is described in the general case of inter-system interactions between one-port devices and in Chapters 3 and 4 extensions are made to also allow for multiple non-collocated noise sources and semi-anechoic conditions. Finally, in Chapter 5, the novel method is adapted to handle intra-system EMC behavior by combining the derived techniques with a multiport circuit theory approach.

2

Efficient Modeling of Interactions between Radiating Devices with Arbitrary Relative Positions and Orientations

Based on "Efficient modeling of interactions between radiating devices with arbitrary relative positions and orientations," Gert-Jan Stockman, Hendrik Rogier and Dries Vande Ginste, *IEEE Transactions on Electromagnetic Compatibility*, vol. 56, no. 6, pp. 1313-1321, December 2014.

★ ★ ★

A novel method to efficiently compute the interaction between two devices is proposed with the aim of accurately reproducing radiated immunity and emission tests in simulations. The technique allows an arbitrary relative position and orientation between the two devices. It relies on a single simulation (or measurement) of the radiation pattern of each device. To take rotation of the devices into account, a spherical harmonics decomposition is applied together with Wigner-D rotation matrices. The resulting procedure is practical, has a low computational cost and shows good agreement with measurements and full-wave simulations.

2.1 Introduction

Analysis of the Electromagnetic Compatibility (EMC) behavior of novel devices and systems is of critical importance, especially given the presence of the vast amount

of electronic products with ever increasing operating frequencies in our society. When studying Electromagnetic Interference (EMI), both emission and susceptibility aspects require careful examination. Compliance tests for the assessment of radiated emission or immunity are often carried out in an anechoic chamber. The Device Under Test (DUT) is then rotated and a new measurement is performed for every angular position. However, also during the design phase (or precompliance phase), it is beneficial to take radiated emission and immunity into account. In the ideal case, this is done via simulations, although often not a trivial task. A single simulation requires large computational resources in order to achieve accurate results. Moreover, every angular position calls for a separate simulation.

To relax these high computational requirements, many methods have been developed to mimic (aspects of) the large electromagnetic problem. In [1], emission is studied and devices are modeled as equivalent sources using the Source Reconstruction Method (SRM). A Printed Circuit Board (PCB), for example, is replaced by an equivalent source containing both the electric and magnetic currents. Another emission model is developed in [2] for Integrated Circuits (ICs), where the electromagnetic field is expanded in multipoles, reducing the number of required problem parameters. When looking at susceptibility, various hybrid techniques have been proposed. In [3], model-reduction techniques are combined with full-wave solvers. In [4], a hybrid method, based on the Finite-Difference Time-Domain (FDTD) algorithm and a field coupling model of transmission lines, is used for the analysis of coupled interconnects on dispersive dielectrics. Furthermore, [5] and [6] discuss susceptibility of transmission line networks with linear/nonlinear load terminations, subject to arbitrary excitations, and PCBs subject to near-zone illuminations via an extended S-parameter model.

Another way to reduce computational resources is by so-called Domain Decomposition Methods (DDMs). Nonconformal Finite Element (FE)-based DDMs to simulate high-speed interconnects and multiscale electromagnetic scattering problems have been reported in [7] and [8], respectively. Furthermore, the interaction between an antenna and a Perfect Electric Conductor (PEC) scatterer has been described via a hybrid Physical Optics (PO)/generalized-scattering-matrix approach [9]. Recently, in [10], a DDM-like approach was suggested to model the interaction between different segments of complex Radio Frequency (RF) structures by using eigenmodal expansions. In [11], multilayer high-speed interconnects are modelled using modal ports. The latter methods do not include radiation.

In this chapter, we will not consider emission or susceptibility separately, but the interaction between radiating devices. The novelty of our method lies in the fact that it is based purely on a single simulation (or measurement) of the radiation patterns of each device. Rotation of the devices is performed via spherical harmonics expansions and Wigner-D matrices. The advantage is that the devices may be moved and rotated over various angles without requiring new simulations (or measurements). As such, the technique is very tractable and opens the way to the efficient reproduction of radiated emission and immunity tests in simulations.

To validate the novel method, simulation and measurement results are presented, demonstrating the accuracy and efficiency of our approach.

This chapter is organized as follows. Section 2.2 explains the formalism. The electromagnetic interaction between two devices is described, as well as how these devices can be rotated over arbitrary angles. Sections 2.3 and 2.4 contain numerical and experimental results to thoroughly validate and illustrate the novel method. The conclusions are presented in Section 2.5. In the sequel, all sources and fields are assumed to be time harmonic with angular frequency ω and time dependencies $e^{j\omega t}$ are suppressed. Unit vectors are denoted with a "hat", e.g. $\hat{\mathbf{v}}$.

2.2 Formalism

2.2.1 Electromagnetic interaction between two devices

We start from the very general problem geometry shown in Fig. 2.1, consisting of two radiating devices, represented by current density sources $\mathbf{j}_{\text{TX}}$ and $\mathbf{j}_{\text{RX}}$ defined in volumes V_{TX} and V_{RX}, respectively. To each device's phase center, $\mathcal{O}_{\text{TX}}$ and

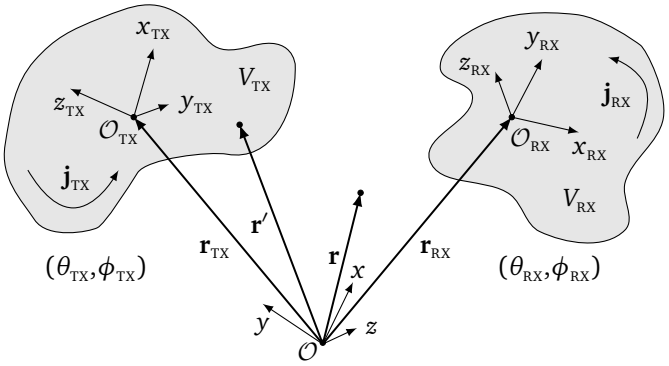

Figure 2.1: Two radiating devices, rotated over arbitrary angles $(\theta_{\text{TX}}, \phi_{\text{TX}})$ and $(\theta_{\text{RX}}, \phi_{\text{RX}})$.

$\mathcal{O}_{\text{RX}}$, a local coordinate system is attached ($(x_{\text{TX}}, y_{\text{TX}}, z_{\text{TX}})$ and $(x_{\text{RX}}, y_{\text{RX}}, z_{\text{RX}})$). The devices may be rotated over arbitrary inclination and azimuthal angles $(\theta_{\text{TX}}, \phi_{\text{TX}})$ and $(\theta_{\text{RX}}, \phi_{\text{RX}})$ with respect to the fixed coordinate system (x, y, z) with origin $\mathcal{O}$. The electric field generated by the sources is given by the Electric Field Integral Equation (EFIE) [12]:

$$\mathbf{e}(\mathbf{r}) = -j\omega\mu \int_V \mathcal{G}(\mathbf{r}, \mathbf{r}') \cdot \mathbf{j}(\mathbf{r}') \, \mathrm{d}\mathbf{r}', \tag{2.1}$$

where $\mathbf{j}(\mathbf{r}')$ represents both current densities $\mathbf{j}_{\text{TX}}(\mathbf{r}')$ and $\mathbf{j}_{\text{RX}}(\mathbf{r}')$. μ is the permeability of the background media, and $\mathcal{G}(\mathbf{r}, \mathbf{r}')$ the three-dimensional dyadic Green's

function given by

$$\mathcal{G}(\mathbf{r},\mathbf{r}') = \Big[\mathcal{I} + \frac{1}{k^2}\nabla\nabla\Big]\frac{e^{-jk|\mathbf{r}-\mathbf{r}'|}}{4\pi|\mathbf{r}-\mathbf{r}'|}. \tag{2.2}$$

Here, $\mathcal{I}$ is the unit dyadic, $k = \omega\sqrt{\epsilon\mu}$ the wavenumber of the background medium and ϵ its permittivity. The integration domain V extends over both devices (denoted as transmitter TX and receiver RX), i.e. $V = V_{\text{TX}} \cup V_{\text{RX}}$. In this chapter we assume that the devices are spaced sufficiently far from each other, such that there is no coupling via the reactive near-field. For such devices, positioned in each other's Fresnel or Fraunhofer region, the field incident on the receiving device can be accurately approximated by restricting V to V_{TX} in (2.1).

We proceed by considering the scalar 3-D Green's function and by making use of Gegenbauer's addition theorem [13]:

$$\frac{e^{-jk|\mathbf{D}+\mathbf{d}|}}{|\mathbf{D}+\mathbf{d}|} = -jk\sum_{l=0}^{\infty}(-1)^l(2l+1)j_l(k|\mathbf{d}|)h_l^{(2)}(k|\mathbf{D}|)P_l(\hat{\mathbf{d}}\cdot\hat{\mathbf{D}}). \tag{2.3}$$

Here, $j_l(\cdot)$ is the l-th order spherical Bessel function of the first kind, $h_l^{(2)}(\cdot)$ the l-th order spherical Hankel function of the second kind and $P_l(\cdot)$ the Legendre polynomial of degree l. The product $j_l(k|\mathbf{d}|)P_l(\hat{\mathbf{d}}\cdot\hat{\mathbf{D}})$ can be expanded into plane waves as [14]

$$4\pi(-j^l)j_l(k|\mathbf{d}|)P_l(\hat{\mathbf{d}}\cdot\hat{\mathbf{D}}) = \iint_{\Omega} e^{-j\mathbf{k}\cdot\mathbf{d}}P_l(\hat{\mathbf{k}}\cdot\hat{\mathbf{D}})\,\mathrm{d}\hat{\mathbf{k}}, \tag{2.4}$$

where we integrate over the Ewald sphere Ω and $\mathbf{k}$ is the wave vector in spherical coordinates:

$$\mathbf{k} = k\,\hat{\mathbf{k}} = k(\sin\theta\cos\phi\,\hat{\mathbf{x}} + \sin\theta\sin\phi\,\hat{\mathbf{y}} + \cos\theta\,\hat{\mathbf{z}}). \tag{2.5}$$

In the configuration under study (Fig. 2.1), $\mathbf{r}_{\text{TX}}$ and $\mathbf{r}_{\text{RX}}$ refer to the positions of the phase centers $\mathcal{O}_{\text{TX}}$ and $\mathcal{O}_{\text{RX}}$ of the transmitter and receiver respectively, with respect to the origin $\mathcal{O}$. Introducing $\mathbf{D} = \mathbf{r}_{\text{TX,RX}} = \mathbf{r}_{\text{RX}} - \mathbf{r}_{\text{TX}}$, $\mathbf{d} = (\mathbf{r}-\mathbf{r}_{\text{RX}}) - (\mathbf{r}'-\mathbf{r}_{\text{TX}})$ and thus $(\mathbf{D}+\mathbf{d}) = (\mathbf{r}-\mathbf{r}')$ into (2.3) and (2.4) yields an expression for the kernel of the EFIE (2.1):

$$\frac{e^{-jk|\mathbf{r}-\mathbf{r}'|}}{|\mathbf{r}-\mathbf{r}'|} = \frac{-jk}{4\pi}\iint_{\Omega} e^{-j\mathbf{k}\cdot(\mathbf{r}-\mathbf{r}_{\text{RX}})}T(\mathbf{r}_{\text{TX,RX}},\hat{\mathbf{k}})e^{+j\mathbf{k}\cdot(\mathbf{r}'-\mathbf{r}_{\text{TX}})}\,\mathrm{d}\hat{\mathbf{k}}. \tag{2.6}$$

The operator $T(\mathbf{r}_{\text{TX,RX}},\hat{\mathbf{k}})$ is calculated as

$$T(\mathbf{r}_{\text{TX,RX}},\hat{\mathbf{k}}) \approx \sum_{l=0}^{L}(2l+1)j^{-l}h_l^{(2)}(k|\mathbf{r}_{\text{TX,RX}}|)P_l(\hat{\mathbf{k}}\cdot\hat{\mathbf{r}}_{\text{TX,RX}}). \tag{2.7}$$

The interchange of summation and integration, which was performed to obtain (2.6), is only allowed if the infinite sum is truncated to a finite number of terms L. This number determines the accuracy and traditional guidelines to select it can be used [13]. Note that, for (2.6) to be valid, $|\mathbf{d}| < |\mathbf{D}|$ or equivalently $|(\mathbf{r}-\mathbf{r}_{\text{RX}})-(\mathbf{r}'-\mathbf{r}_{\text{TX}})| < |\mathbf{r}_{\text{TX,RX}}|$ must hold. Using the EFIE (2.1) and the kernel (2.6), we obtain an approximate expression for the electric field incident on the receiver, caused by the transmitter:

$$\mathbf{e}^{\text{inc}}(\mathbf{r}) \approx -\frac{\omega k}{4\pi}\iint_{\Omega} e^{-j\mathbf{k}\cdot(\mathbf{r}-\mathbf{r}_{\text{RX}})} T(\mathbf{r}_{\text{TX,RX}},\hat{\mathbf{k}})\left[\mathcal{I}-\hat{\mathbf{k}}\hat{\mathbf{k}}\right]\cdot\mathbf{N}_{\text{TX}}(\hat{\mathbf{k}})\,\mathrm{d}\hat{\mathbf{k}}, \tag{2.8}$$

where $\mathbf{N}_{\text{TX}}(\hat{\mathbf{k}})$ is given by

$$\mathbf{N}_{\text{TX}}(\hat{\mathbf{k}}) = \frac{\mu}{4\pi}\int_{V_{\text{TX}}} e^{j\mathbf{k}\cdot(\mathbf{r}'-\mathbf{r}_{\text{TX}})}\mathbf{j}(\mathbf{r}')\,\mathrm{d}\mathbf{r}'. \tag{2.9}$$

We define the radiation pattern $\mathbf{F}_{\text{TX}}(\hat{\mathbf{k}})$ of the transmitting device as

$$\begin{aligned}\mathbf{F}_{\text{TX}}(\hat{\mathbf{k}}) &= F_{\text{TX},\theta}(\hat{\mathbf{k}})\hat{\theta} + F_{\text{TX},\phi}(\hat{\mathbf{k}})\hat{\phi}\\ &= j\omega\hat{\mathbf{k}}\times[\hat{\mathbf{k}}\times\mathbf{N}_{\text{TX}}(\hat{\mathbf{k}})],\end{aligned} \tag{2.10}$$

and hence,

$$\begin{aligned}\left[\mathcal{I}-\hat{\mathbf{k}}\hat{\mathbf{k}}\right]\cdot\mathbf{N}_{\text{TX}}(\hat{\mathbf{k}}) &= \mathbf{N}_{\text{TX}}(\hat{\mathbf{k}}) - \hat{\mathbf{k}}[\hat{\mathbf{k}}\cdot\mathbf{N}_{\text{TX}}(\hat{\mathbf{k}})]\\ &= -\hat{\mathbf{k}}\times[\hat{\mathbf{k}}\times\mathbf{N}_{\text{TX}}(\hat{\mathbf{k}})]\\ &= -\frac{1}{j\omega}\mathbf{F}_{\text{TX}}(\hat{\mathbf{k}}).\end{aligned} \tag{2.11}$$

Consequently, the incident electric field (2.8) can be written in terms of $\mathbf{F}_{\text{TX}}(\hat{\mathbf{k}})$.

Assume now, for simplicity, that the transmitter and receiver are one-port devices. Then, an equivalent circuit representation [12] of this configuration is shown in Fig. 2.2, where Z_{TX} and Z_{RX} are the radiation impedances of the transmitter and receiver respectively. The transmitter is driven by means of a Thévenin generator

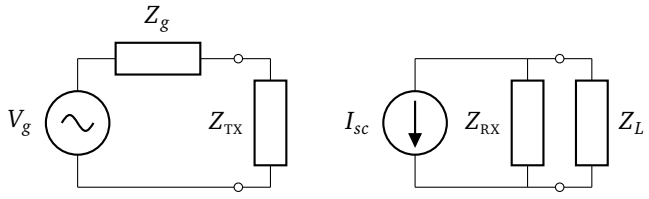

Figure 2.2: Equivalent circuit of the two interacting devices.

composed of a sinusoidal voltage source V_g with internal impedance Z_g. The Norton equivalent of the receiver consists of a load impedance Z_L and a short-circuit current I_{sc}, computed as

$$I_{sc} = -\frac{1}{V_0} \int_{V_{\text{RX}}} \mathbf{e}^{\text{inc}}(\mathbf{r}) \cdot \mathbf{j}(\mathbf{r}) \, \mathrm{d}\mathbf{r}, \tag{2.12}$$

where V_0 is the pertinent normalization factor, evolving from the reciprocity theorem, depending on the normalized radiation pattern when operating the antenna in transmit mode (see [15] for a detailed explanation). Defining the radiation pattern $\mathbf{F}_{\text{RX}}(\hat{\mathbf{k}})$ of the receiver in a similar way as (2.10) and substituting (2.8) and (2.11) into (2.12), yields the following expression for the short-circuit current:

$$I_{sc} \approx -\frac{1}{ZV_0} \iint_{\Omega} T(\mathbf{r}_{\text{TX,RX}}, \hat{\mathbf{k}}) \mathbf{F}_{\text{TX}}(\hat{\mathbf{k}}) \cdot \mathbf{F}_{\text{RX}}(-\hat{\mathbf{k}}) \, \mathrm{d}\hat{\mathbf{k}}, \tag{2.13}$$

where $Z = \sqrt{\frac{\mu}{\epsilon}}$ is the wave impedance of the background medium.

In the context of EMC, an interesting conclusion is now readily derived from (2.13): to calculate the influence of a transmitting (noisy) device on a receiving (susceptible) device, it is sufficient to have access to either their measured or simulated radiation patterns. This is true for any relative position between the two devices, indicated by $\mathbf{r}_{\text{TX,RX}}$, as long as there is no coupling via the reactive near-field, hence $|\mathbf{r}_{\text{TX,RX}}|$ should be larger than, say, at least a sixth of the wavelength.

2.2.2 Rotation of the devices

Now we extend the above results, to turn them into a formalism that is of practical use and of critical importance in the domain of EMC, i.e. to reproduce immunity and emission tests in a simulation. During such tests, the behavior of DUTs is observed while they are being *rotated*. We will show that the outcome of such a test can be predicted by means of simple measurement or simulation of the radiation patterns of the transmitting and receiving devices.

In a spherical coordinate system, the two scalar components of a radiation pattern $\mathbf{F}(\hat{\mathbf{k}}) = F_\theta(\hat{\mathbf{k}})\hat{\theta} + F_\phi(\hat{\mathbf{k}})\hat{\phi}$ may be decomposed into spherical harmonics A_{pq} and B_{pq} as follows [16]:

$$F_\theta(\theta,\phi) = \sum_{p=0}^{P} \sum_{|q|\le p} \Big[A_{pq} \frac{\mathrm{d}Y_{pq}(\theta,\phi)}{\mathrm{d}\theta} + B_{pq} \frac{qY_{pq}(\theta,\phi)}{\sin\theta} \Big] \tag{2.14a}$$

$$F_\phi(\theta,\phi) = j \sum_{p=0}^{P} \sum_{|q|\le p} \Big[A_{pq} \frac{qY_{pq}(\theta,\phi)}{\sin\theta} + B_{pq} \frac{\mathrm{d}Y_{pq}(\theta,\phi)}{\mathrm{d}\theta} \Big], \tag{2.14b}$$

where, for reasons of clarity, the notation $\hat{\mathbf{k}}$ has been replaced by (θ, ϕ) and with P again a parameter that determines the accuracy. Furthermore, $Y_{pq}(\theta, \phi)$ are the orthonormalized scalar spherical harmonics given by [17]

$$Y_{pq}(\theta, \phi) = \sqrt{\frac{(2p+1)}{4\pi}\frac{(p-q)!}{(p+q)!}} P_p^q(\cos\theta) e^{jq\phi}, \tag{2.15}$$

where $P_p^q(\cdot)$ is the associated Legendre polynomial of degree p and order q. As shown in Section 2.3 and explained in [18], for practical purposes, P may be chosen equal to L.

The above decomposition into spherical harmonics allows for an easy rotation of the DUTs. A rotated version $\mathbf{F}^{\mathcal{R}}(\theta, \phi)$ of the original $\mathbf{F}(\theta, \phi)$ is efficiently computed by following the scheme represented in Fig. 2.3. The transformation $\mathcal{R}$ represents

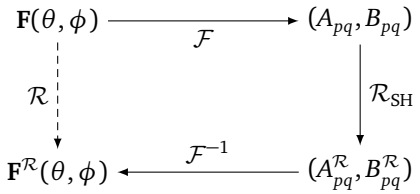

Figure 2.3: Rotation of $\mathbf{F}(\theta, \phi)$ to $\mathbf{F}^{\mathcal{R}}(\theta, \phi)$ using the spherical harmonics domain.

the desired rotation in the spatial domain. $\mathcal{F}$ denotes the expansion into spherical harmonics, as derived in Appendix A, whereas $\mathcal{F}^{-1}$ is the inverse transformation (2.14). In a more compact notation the transformation $\mathcal{F}$ can be written as:

$$\begin{aligned}\mathcal{F} \longleftrightarrow \begin{Bmatrix} A_{pq} \\ B_{pq} \end{Bmatrix} = \frac{-1}{p(p+1)} \int_0^{2\pi} \int_0^{\pi} \Bigg[q \begin{Bmatrix} jF_\phi(\theta,\phi) \\ -F_\theta(\theta,\phi) \end{Bmatrix} Y_{pq}^*(\theta,\phi) \\ + \sin\theta \begin{Bmatrix} -F_\theta(\theta,\phi) \\ jF_\phi(\theta,\phi) \end{Bmatrix} \frac{\mathrm{d}Y_{pq}^*(\theta,\phi)}{\mathrm{d}\theta} \Bigg] \mathrm{d}\theta \mathrm{d}\phi,\end{aligned} \tag{2.16}$$

while the inverse transformation $\mathcal{F}^{-1}$ is given by

$$\mathcal{F}^{-1} \longleftrightarrow \begin{Bmatrix} F_\theta(\theta,\phi) \\ F_\phi(\theta,\phi) \end{Bmatrix} = \sum_{p=0}^{P} \sum_{|q|\le p} \Bigg[\begin{Bmatrix} A_{pq} \\ jB_{pq} \end{Bmatrix} \frac{\mathrm{d}Y_{pq}(\theta,\phi)}{\mathrm{d}\theta} + \begin{Bmatrix} B_{pq} \\ jA_{pq} \end{Bmatrix} \frac{qY_{pq}(\theta,\phi)}{\sin\theta} \Bigg], \tag{2.17}$$

where $*$ denotes the complex conjugate.

The rotation itself is performed in the spherical harmonics domain by the transformation $\mathcal{R}_{SH}$ that makes use of Wigner D-matrices, as follows: the rotated coeffi-

cients of the spherical harmonics expansion are calculated as [19]

$$\mathcal{R}_{\mathrm{SH}} \longleftrightarrow \begin{Bmatrix} A^{\mathcal{R}}_{pq} \\ B^{\mathcal{R}}_{pq} \end{Bmatrix} = \begin{Bmatrix} A_{pq} \\ B_{pq} \end{Bmatrix} \sum_{|r|\leq p} e^{-jq\gamma} d^r_{pq}(\beta) e^{-jr\alpha}, \tag{2.18}$$

with the Wigner D-matrix $D^r_{pq}(\cdot)$ given by [20]

$$D^r_{pq}(\alpha,\beta,\gamma) = e^{-jq\gamma} d^r_{pq}(\beta) e^{-jr\alpha}, \tag{2.19}$$

and where $d^r_{pq}(\beta)$ is the Wigner small d-matrix, given by

$$\begin{aligned} d^r_{pq}(\beta) =& (-1)^{r-q} \sqrt{(p+r)!(p-r)!(p+q)!(p-q)!} \\ & \cdot \sum_s (-1)^s \frac{\left(\cos\frac{\beta}{2}\right)^{2(p-s)+q-r} \left(\sin\frac{\beta}{2}\right)^{2s-q+r}}{(p+q-s)!s!(r-q+s)!(p-r-s)!}. \end{aligned} \tag{2.20}$$

Here, the range of s is determined by the condition that all factorials are nonnegative, thus $s \in [\max(0, q-r), \min(p+q, p-r)]$. In (2.18)-(2.20), α, β and γ are the standard Euler angles that define the rotation using the $z-y-z$ convention in a right-handed frame as shown in Fig. 2.4. To go from an original radiation pattern $\mathbf{F}(\theta,\phi)$ in the coordinate system (x,y,z) to a rotated version $\mathbf{F}^{\mathcal{R}}(\theta,\phi)$ in the coordinate system $(x^{\mathcal{R}}, y^{\mathcal{R}}, z^{\mathcal{R}})$, we first rotate by an angle α about the z-axis, then by an angle β about the new y'-axis and finally by an angle γ about the new

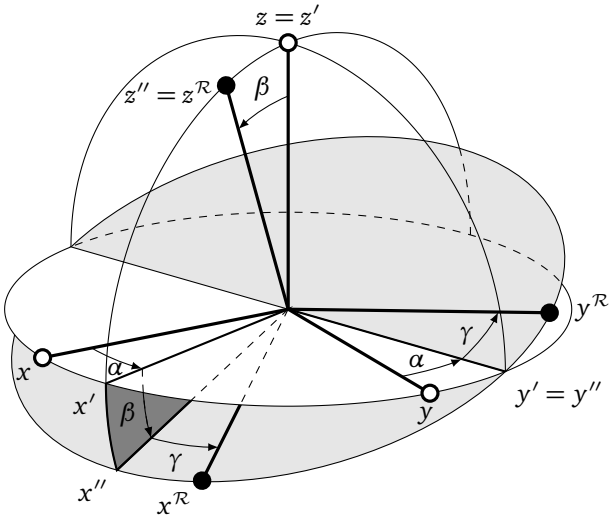

Figure 2.4: Euler angles α, β and γ in the $z-y-z$ convention when rotating from coordinate system (x,y,z) to $(x^{\mathcal{R}}, y^{\mathcal{R}}, z^{\mathcal{R}})$.

z''-axis. The accompanying rotation matrix $\mathcal{R}$ is given by

$$\begin{aligned}\mathcal{R} =& \mathcal{R}_{z'',\gamma} \cdot \mathcal{R}_{y',\beta} \cdot \mathcal{R}_{z,\alpha} = \mathcal{R}_{z,\alpha} \cdot \mathcal{R}_{y,\beta} \cdot \mathcal{R}_{z,\gamma} \\ =& \begin{bmatrix} \cos\alpha & -\sin\alpha & 0 \\ \sin\alpha & \cos\alpha & 0 \\ 0 & 0 & 1 \end{bmatrix} \cdot \begin{bmatrix} \cos\beta & 0 & \sin\beta \\ 0 & 1 & 0 \\ -\sin\beta & 0 & \cos\beta \end{bmatrix} \cdot \begin{bmatrix} \cos\gamma & -\sin\gamma & 0 \\ \sin\gamma & \cos\gamma & 0 \\ 0 & 0 & 1 \end{bmatrix}. \end{aligned} \quad (2.21)$$

Starting from a proper reference orientation, any target orientation can be reached. For example, in the case of Fig. 2.4, the Euler angles (α, β, γ) are readily related to the inclination and azimuthal angles θ and ϕ, by choosing $\alpha = \phi$, $\beta = \theta$ and $\gamma = 0$.

The advantage of the spherical harmonics expansion is now evident. When two devices are rotated over arbitrary angles, only (the coefficients of) the original non-rotated radiation patterns are needed to perform a simulation. Via (2.13) and the scheme represented in Fig. 2.3 the interaction between devices is efficiently calculated for any set of rotations and positions of the devices. When leveraging traditional simulation tools or measurements, a new computation or measurement is needed for every rotation or repositioning.

2.3 Validation Examples

2.3.1 Simulation example

To validate the formalism, we conduct a numerical experiment where transmitter and receiver are both half-wavelength dipoles, as seen in Fig. 2.5. The obtained short circuit current I_{sc} from the advocated spherical harmonics method is numerically compared to a reference solution, i.e. a Method of Moments (MoM) for arbitrary thin wires [21]. In this example, the distance between the dipoles is chosen to be $|\mathbf{r}_{\mathrm{TX,RX}}| = \lambda = 1\,\mathrm{m}$ and the wire thickness equals $10^{-4}\lambda$. The MoM simulation uses five segments to model the half-wavelength dipole and the short-circuit current is calculated directly by inverting the full MoM matrix equation. The transmitting dipole is excited with $V_g = 1\,\mathrm{V}$ between its terminals and $Z_g = Z_L = 0\,\Omega$. More information on the MoM for thin wire antennas can be found in Appendix B.

To verify the novel spherical harmonics method, we only need the dipole's radiation pattern $\mathbf{F}(\theta, \phi)$. This can, e.g., be obtained via a new MoM simulation for a *single* dipole, leading to the current density $\mathbf{j}(\mathbf{r})$ on its wires. Using (2.9) and (2.10), the radiation pattern of the half-wavelength dipole is now found.

This radiation pattern is now decomposed into spherical harmonics by (2.16) and afterwards rotated using (2.18). We have used $P = L = 2$. Subsequently, the rotated radiation patterns $\mathbf{F}^{\mathcal{R}}(\theta, \phi)$ are reconstructed using (2.17) and finally substituted into (2.13) to calculate the short-circuit current I_{sc}. The short-circuit current obtained from the MoM simulation and the novel spherical harmonics method are compared in Fig. 2.6, where the transmitter is rotated over Euler angles $\alpha = \beta = \gamma$,

varying from 0 till 2π, while the receiver remains fixed. Additionally, the short-circuit current is also computed via a traditional approach leveraging the well-known Friis formula [22]. An excellent agreement between the novel method and the MoM simulation as well as a superior accuracy compared to the Friis formula are observed. This is due to the higher-order multipole interactions which are accounted for in the novel formalism, whereas the Friis formula only leads to accurate results when the devices are situated in each other's far field. The MoM simulation for all angles took 40.56 s whereas the novel method only took 0.52 s. Hence, an impressive speed-up factor of about 80 is achieved. In addition to the much shorter simulation times, only the $(P+1)^2$ coefficients A_{pq} and B_{pq} have to be stored to simulate any situation with relative position and orientation. All simulations have been carried out on an Intel® Core™ i7-2600 processor running at 3.40 GHz and with 16 GB of memory.

2.3.2 Measurement example

To further validate the method and to demonstrate its applicability, a measurement has been performed that mimics an EMC test. In an anechoic chamber a Standard Gain Horn (SGH) has a fixed position in space and acts as the transmitter. A microstrip patch antenna acts as the receiver and is mounted on a rotatable arm (driven by the Orbit/FR AL-4164-4MC Positioner Controller), in line with the main lobe of the SGH and with their phase centers at the same height. The setup is schematically shown in Fig. 2.7. The patch antenna is rotated over angles θ and ϕ while the SGH transmits a Continuous Wave (CW) signal and the incoming power at the patch antenna is measured for every orientation. This incoming power is

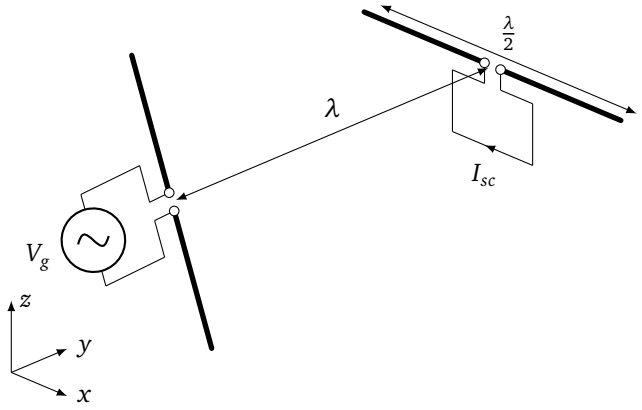

Figure 2.5: Configuration for the simulation example where here the transmitter (left) is rotated over Euler angles $\alpha = \beta = \gamma = 3\pi/4$ w.r.t. the receiver (right). Transmitter and receiver are both half-wavelength dipoles, separated by a distance $|\mathbf{r}_{\text{TX,RX}}| = \lambda$, and $Z_L = Z_g = 0\,\Omega$.

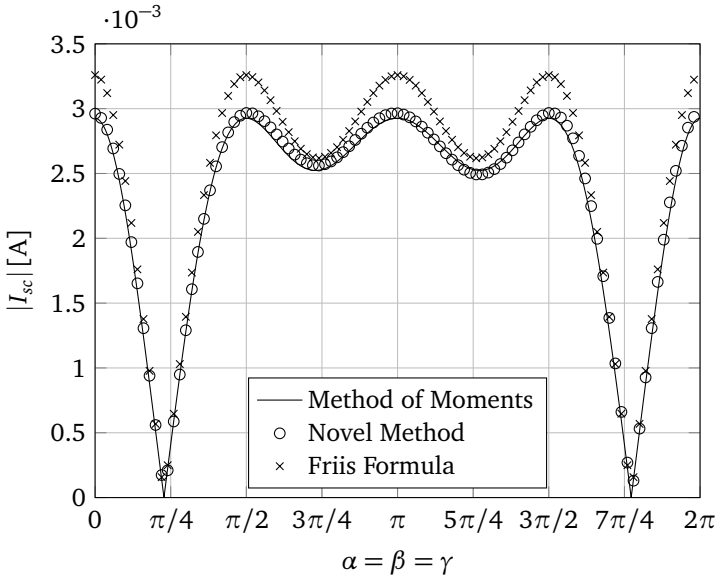

Figure 2.6: Amplitude of the short-circuit current at the port of the receiving dipole, induced by a transmitting dipole, rotated over Euler angles $\alpha = \beta = \gamma$ (see also Fig. 2.5).

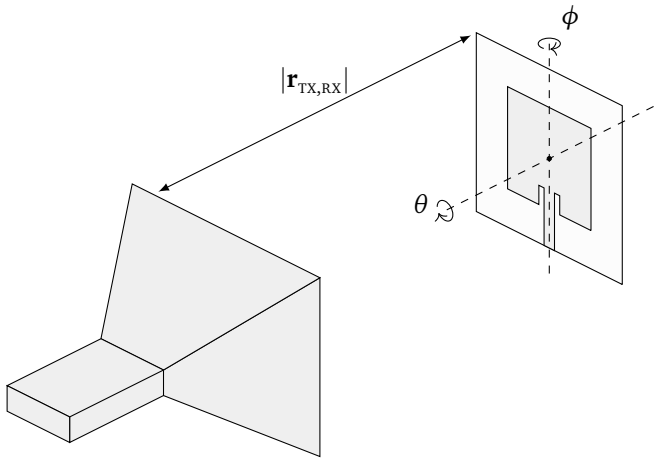

Figure 2.7: Measurement setup in the anechoic chamber where a SGH acts as transmitter and a patch antenna as receiver.

compared to a simulation using simulated radiation patterns and the spherical harmonics method. The incoming power P_{RX} can easily be calculated from the simulated short-circuit current (2.13).

The SGH used in the measurement operates in the band $1.12 - 1.7\,\text{GHz}$. Its dimensions are: $a = 560\,\text{mm}$, $b = 420\,\text{mm}$, $\rho_1 = 490\,\text{mm}$ and $\rho_2 = 550\,\text{mm}$ (see Appendix C). As a receiver, an inset-fed microstrip patch antenna resonating at 1.5 GHz has been designed and manufactured. A Vector Network Analyzer (VNA), i.e. the PNA-X N5242A of Agilent Technologies, is used to generate and measure the signals. It is set to output a CW signal of 10 dBm at 1.5 GHz to the SGH. To accurately compare these measurements with simulation, this power is needed directly at the terminals of the devices. To this end, the loss of the coaxial cables connecting the devices with the VNA as well as the mismatch at the input ports have been taken into account. We also varied the distance between transmitter and receiver, adopting the following values: $|\mathbf{r}_{\text{TX,RX}}| = \{5\lambda, 10\lambda, 15\lambda, 20\lambda\}$. Note that $|\mathbf{r}_{\text{TX,RX}}| = 5\lambda$ corresponds to 1 m. This is the minimal distance at which the two devices can be placed in the anechoic chamber, such that they can still be rotated. The radiation pattern of the SGH has been calculated analytically (see Appendix A). The patch antenna was designed with the 3-D planar full-wave solver Momentum from Advanced Design System (ADS) of Agilent Technologies and the radiation pattern has also been simulated with this package.

The results can be seen in Figs. 2.8 and 2.9, where P_{RX} is the received power at the patch antenna's port. Due to the larger electrical size of the antennas compared to the previous simulation example, we made use of $P = L = 10$. A very good agreement between the results of the novel method and the measurements is obtained for all distances $|\mathbf{r}_{\text{TX,RX}}|$. In Fig. 2.8, ϕ is fixed at zero and θ is swept from $-\pi/2$ to $\pi/2$. Note that $\phi = 0$ and $\theta = 0$ corresponds to the situation where the two devices are perfectly lined up along their broadsides. In Fig. 2.9, θ is fixed and ϕ is swept from $-\pi/2$ to $\pi/2$. For ϕ approaching $\pm\pi/2$, the field emitted by the SGH impinges under a grazing angle of incidence onto the patch. ADS-Momentum assumes an infinite ground plane, whilst the real ground plane of the manufactured patch antenna is relatively small. This explains of course the difference between the two methods at these grazing angles. The simulation time of this example was in the order of minutes while the measurement, even with the automatic positioning system, took a couple of hours.

2.4 Application Example

To further demonstrate the practical applicability and the high efficiency of the novel method, a more complex example is considered here. It consists of a small thin-wire electric dipole antenna with length 4 cm inside a PEC metallic shielding enclosure. The enclosure is a 50 cm side cubic box with a horizontal aperture in the front plane having dimensions 20 cm × 5 cm, as depicted in Fig. 2.10. The dipole antenna inside the enclosure is excited and another identical dipole an-

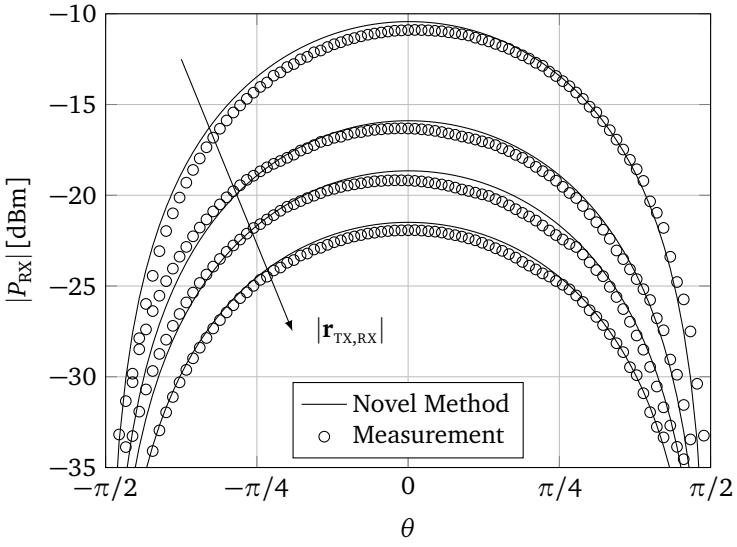

Figure 2.8: Received power at the microstrip patch antenna induced by a SGH for a fixed $\phi = 0$ and separated by a distance $|\mathbf{r}_{TX,RX}| = \{5\lambda, 10\lambda, 15\lambda, 20\lambda\}$.

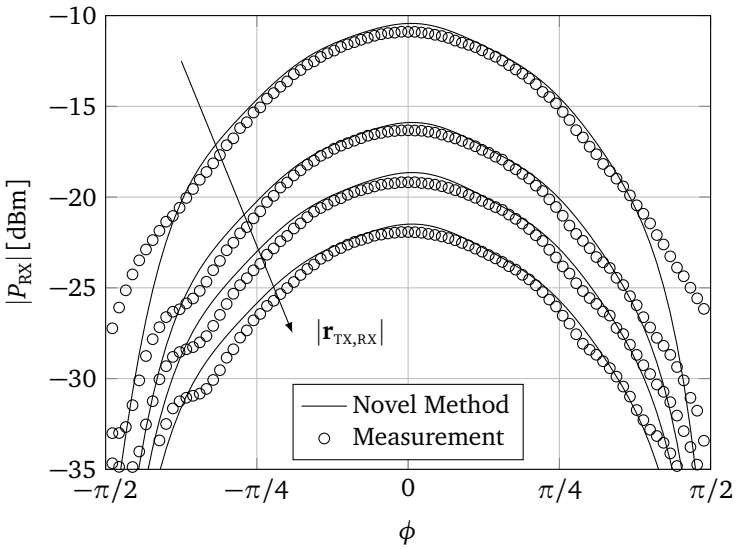

Figure 2.9: Received power at the microstrip patch antenna induced by a SGH for a fixed $\theta = 0$ and separated by a distance $|\mathbf{r}_{TX,RX}| = \{5\lambda, 10\lambda, 15\lambda, 20\lambda\}$.

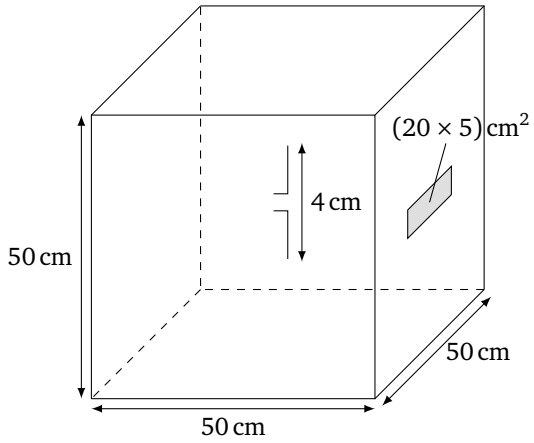

Figure 2.10: Small thin-wire electrical dipole antenna inside a PEC metallic shielding enclosure. The enclosure is a 50 cm side cubic box with a horizontal aperture in the front plane.

tenna, placed in front of the slot, acts as a receiver. The distance between the dipole's phase centers is 3.25 m, such that the receiving dipole is 3 m away from the horizontal aperture in the front plane. The radiation patterns of the dipole antenna with and without the shielding enclosure are calculated using Computer Simulation Technology Microwave Studio (CST MWS) and are used as input for our novel method, allowing to efficiently calculate the short-circuit currents induced in the receiving dipole using (2.13). This is done for a transmitter with and without the shielding enclosure leading to short-circuit currents $I_{sc,1}$ and $I_{sc,2}$ respectively. Comparing the amplitude of both these currents yields the Shielding Efficiency (SE), which is defined as

$$\mathrm{SE}\,[\mathrm{dB}] = 20\log_{10}\left(\frac{|I_{sc,2}|}{|I_{sc,1}|}\right). \tag{2.22}$$

The SE calculated over a broad frequency range is shown in Fig. 2.11. For the highest frequency, i.e. 1 GHz, the order of expansion is $P = L = 18$. The obtained SE with the novel method yields excellent agreement with the results shown in Fig. 5 of [23]. Below 200 MHz, some small artifacts are visible, which are due to the radiation pattern simulations with CST MWS, suffering from inaccuracies as the bounding box is too small compared to the wavelength. Positioning the absorbing boundary conditions further away from the enclosure leads to unacceptably long simulaton times or even insufficient memory. We now also compute the SE on a spherical dome centered about the x-axis for a frequency of $f = 500$ MHz (see Fig. 2.12). To this end, the phase center of the receiving dipole antenna is moved over the spherical dome while the alignment of the antenna is always kept vertical, i.e. parallel to the z-axis. The dome is sectioned off from a sphere with radius

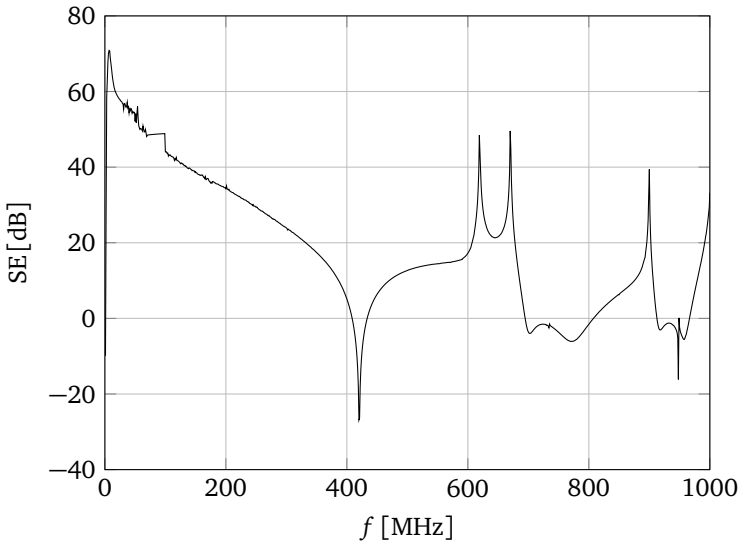

Figure 2.11: SE as a function of frequency for a 50 cm side cubic box with a 20 cm × 5 cm horizontal aperture centered in the front plane.

$|\mathbf{r}_{\mathrm{TX,RX}}| = 3.25\,\mathrm{m}$ and is defined by $-\pi/4 \leq \psi \leq \pi/4$ and $-\pi/2 \leq \chi \leq \pi/2$ with $\psi = -\phi$ and $\chi = \pi/2 - \theta$, corresponding to a solid angle of π. The dimensions of the dipole antenna and enclosure are the same as in Fig. 2.10. The SE is calculated for $181 \times 91 = 16471$ samples on the spherical dome and the result is shown in Fig. 2.13. Computing the SE using CST MWS for one sample of (ψ, χ) takes about 10 minutes when the discretization is set to 10 cells per wavelength. Hence, for all 181×91 samples, about 100 days would be needed. The novel method is much faster in that it only needs the single-element radiation patterns from CST MWS, which takes 112 s (for the same discretization and solver settings). Furthermore, calculating the SE itself takes 8.36 ms per sample, leading to a total computation time of $112\,\mathrm{s} + 181 \times 91 \times 8.36\,\mathrm{ms} = 249.7\,\mathrm{s}$. This application example clearly shows that, especially for complex structures where the radiation pattern of the DUT is not easily derived, significant improvements in calculation time are obtained.

2.5 Conclusions

In this chapter, a novel method has been developed that opens the way towards an efficient and accurate reproduction of immunity and emission tests in simulations. The method starts from a single simulation (or measurement) of the DUT's radiation pattern. These devices may be moved and rotated over arbitrary inclination and azimuthal angles, as long as there is no interaction with the reactive near-field. The rotation is performed by expanding the radiation patterns into spherical

harmonics and using the Wigner-D rotation matrices on the obtained coefficients of this expansion. The advantage of the proposed method is that for every rotation or repositioning, the interaction between devices is easily calculated without the need for a new computation or measurement, as is the case for traditional simulations or measurements. The method was thoroughly validated and illustrated via numerical and experimental examples.

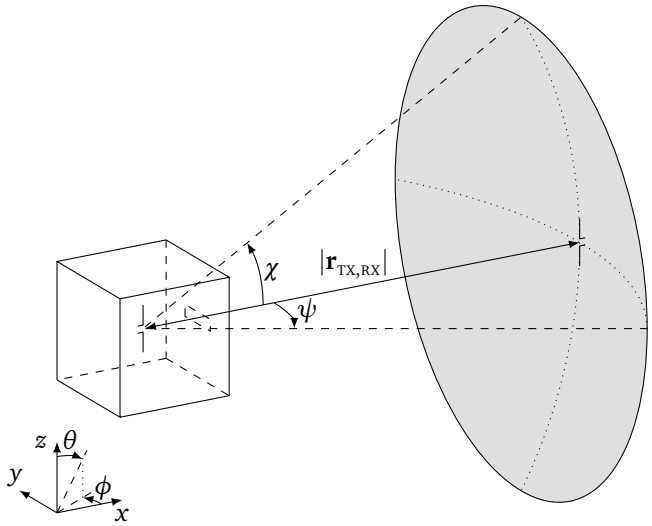

Figure 2.12: Spherical dome on which the SE is calculated with $|\mathbf{r}_{TX,RX}| = 3.25\,\text{m}$, $-\pi/4 \leq \psi \leq \pi/4$ and $-\pi/2 \leq \chi \leq \pi/2$ with $\psi = -\phi$ and $\chi = \pi/2 - \theta$. The orientation of the receiving dipole is always kept vertical, i.e. parallel to the z-axis.

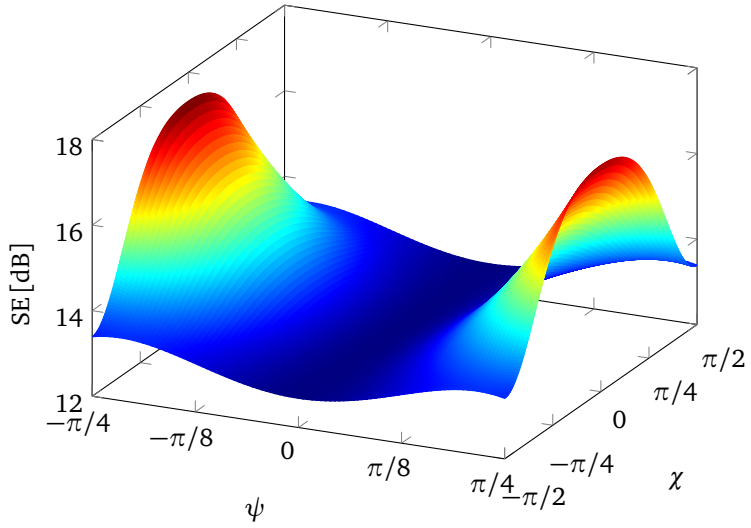

Figure 2.13: SE calculated on the spherical dome for a frequency of $f = 500\,\mathrm{MHz}$ (see Fig. 2.12). The number of samples equals 181×91.

References

[1] P. Li and L. J. Jiang, "Source reconstruction method-based radiated emission characterization for PCBs", *IEEE Transactions on Electromagnetic Compatibility*, vol. 55, no. 5, pp. 933–940, Oct. 2013.

[2] P. Kralicek, W. John, R. De Smedt, K. Vervoort, and H. Garbe, "A voltage controlled emission model of electromagnetic emission of IC for system analysis", in *IEEE International Symposium on Electromagnetic Compatibility*, Montreal, Quebec, 13-17 Aug. 2001, pp. 1197–1202.

[3] I. Erdin, M. Nakhla, and R. Achar, "Circuit analysis of electromagnetic radiation and field coupling effects for networks with embedded full-wave modules", *IEEE Transactions on Electromagnetic Compatibility*, vol. 42, no. 4, pp. 449–460, Nov. 2000.

[4] M. Tang, J. Lu, J. Mao, and L. Jiang, "A systematic electromagnetic-circuit method for EMI analysis of coupled interconnects on dispersive dielectrics", *IEEE Transactions on Microwave Theory and Techniques*, vol. 61, no. 1, pp. 1–13, Jan. 2013.

[5] Y. Bayram and J. Volakis, "Hybrid S-parameters for transmission line networks with linear/nonlinear load terminations subject to arbitrary excitations", *IEEE Transactions on Microwave Theory and Techniques*, vol. 55, no. 5, pp. 941–950, May 2007.

[6] Z. Khan, Y. Bayram, and J. Volakis, "EMI/EMC analysis of printed circuit boards subject to near-zone illuminations", *IEEE Transactions on Electromagnetic Compatibility*, vol. 51, no. 2, pp. 406–408, May 2009.

[7] Y. Shao, Z. Peng, and J.-F. Lee, "Signal integrity analysis of high-speed interconnects by using nonconformal domain decomposition method", *IEEE Transactions on Components, Packaging and Manufacturing Technology*, vol. 2, no. 1, pp. 122–130, Jan. 2012.

[8] Z. Peng, K.-H. Lim, and J.-F. Lee, "Nonconformal domain decomposition methods for solving large multiscale electromagnetic scattering problems", *Proceedings of the IEEE*, vol. 101, no. 2, pp. 298–319, Feb. 2013.

[9] C. Della Giovampaola, E. Martini, A. Toccafondi, and S. Maci, "A hybrid PO/generalized-scattering-matrix approach for estimating the reflector induced mismatch", *IEEE Transactions on Antennas and Propagation*, vol. 60, no. 9, pp. 4316–4325, Sep. 2012.

[10] T. Flisgen, H. Glock, and U. Van Rienen, "Compact time-domain models of complex RF structures based on the real eigenmodes of segments", *IEEE Transactions on Microwave Theory and Techniques*, vol. 61, no. 6, pp. 2282–2294, Jun. 2013.

[11] H. Wu and A. Cangellaris, "A finite-element domain-decomposition methodology for electromagnetic modeling of multilayer high-speed interconnects", *IEEE Transactions on Advanced Packaging*, vol. 31, no. 2, pp. 339–350, May 2008.

[12] J. Van Bladel, *Electromagnetic Fields*. John Wiley & Sons, 2007.

[13] W. C. Chew, J.-M. Jin, E. Michielssen, and J. Song, *Fast and efficient algorithms in computational electromagnetics*. Artech House Publishers, 2001.

[14] J. Stratton, *Electromagnetic Theory*. McGraw-Hill, 1941.

[15] J. Van Bladel, "On the equivalent circuit of a receiving antenna", *IEEE Antennas and Propagation Magazine*, vol. 44, no. 1, pp. 164–165, Feb. 2002.

[16] J. Rahola, F. Belloni, and A. Richter, "Modelling of radiation patterns using scalar spherical harmonics with vector coefficients", in *3rd European Conference on Antennas and Propagation, EuCAP*, Berlin, Germany, 23-27 Mar. 2009, pp. 3361–3365.

[17] *NIST digital library of mathematical functions*, http://dlmf.nist.gov/, Release 1.0.5 of 2012-10-01.

[18] T. F. Eibert, "A diagonalized multilevel fast multipole method with spherical harmonics expansion of the k-space integrals", *IEEE Transactions on Antennas and Propagation*, vol. 53, no. 2, pp. 814–817, Feb. 2005.

[19] R. Hoover, A. Maciejewski, and R. Roberts, "Pose detection of 3-D objects using images sampled on SO(3), spherical harmonics, and Wigner-D matrices", in *IEEE International Conference on Automation Science and Engineering, CASE.*, Arlington, Virginia, 23-26 Aug. 2008, pp. 47–52.

[20] Z. Gimbutas and L. Greengard, "A fast and stable method for rotating spherical harmonic expansions", *Journal of Computational Physics*, vol. 228, pp. 5621–5627, May 2009.

[21] W. C. Gibson, *The Method of Moments in Electromagnetics*. Chapman & Hall/CRC, 2008, ch. 4, pp. 73–79.

[22] C. Balanis, *Antenna Theory: Analysis and Design*. John Wiley & Sons, 2005.

[23] W. Wallyn, D. De Zutter, and H. Rogier, "Prediction of the shielding and resonant behavior of multisection enclosures based on magnetic current modeling", *IEEE Transactions on Electromagnetic Compatibility*, vol. 44, no. 1, pp. 130–138, Feb. 2002.

3

Efficient Full-Wave Modeling of Electromagnetic Interference in the Presence of Multiple Non-Collocated Noise Sources

Based on "Efficient full-wave modeling of electromagnetic interference in the presence of multiple non-collocated noise sources," Gert-Jan Stockman, Hendrik Rogier and Dries Vande Ginste, *Proceedings of the International Conference on Electromagnetics in Advanced Applications*, pp. 175-178, September 2015.

★ ★ ★

In this chapter a novel method is discussed that is of practical use for analyzing the electromagnetic compatibility behavior of electronic systems. The aim is to develop an efficient technique that mimics radiated immunity and emission tests in the presence of multiple non-collocated noise sources in simulation. The proposed method is simple in that it only relies on the simulated (or measured) radiation pattern of the devices in the system while allowing arbitrary positions. Rotation of the devices is performed by a spherical harmonics decomposition of the radiation patterns together with the application of Wigner-D rotation matrices. The adopted assumption is that the devices are spaced sufficiently far from each other such that there is no coupling via the reactive near-field. The proposed procedure shows good agreement with measurements and full-wave simulations while at the same time having a low computational cost.

3.1 Introduction

Examining the Electromagnetic Compatibility (EMC) behavior of devices in an electronic system is of great importance in today's electronic equipment, not only to pass regulatory and legislative laws concerning the radiated emission and immunity relative to other electronic devices, but also to ensure proper operation of different components internally in such a system. Compliance tests that characterize these properties of a device are performed in an anechoic chamber. In such a test, the device under test is rotated over different angles, while a measurement is performed for every angular position. The disadvantage of this method is that it is costly and time-consuming. Furthermore it can only be performed after devices are already prototyped. It would be benificial to take radiated emission and immunity into account during the design phase (or pre-compliance phase). This is usually done using simulations, but requires large computational resources and seperate simulations for every angular position.

In this contribution, we develop a formalism that efficiently models the interaction of multiple non-collocated noise sources on another device, based on work performed in [1]. The different devices in the system are allowed to interact via each other's radiative near field. The proposed formalism only relies on the radiation patterns of the devices present in the system and their mutual positions and orientations.

3.2 Formalism

Consider the general problem geometry of the case with multiple non-collocated sources (N) and one receiving device in Fig. 3.1. The devices are represented by their current density sources $\mathbf{j}^1_{\text{TX}}(\mathbf{r}'), \cdots, \mathbf{j}^N_{\text{TX}}(\mathbf{r}')$ for the transmitters and $\mathbf{j}_{\text{RX}}(\mathbf{r}')$ for the receiver. They are defined in volumes $V^1_{\text{TX}}, ..., V^N_{\text{TX}}$ and V_{RX}, respectively, with their appropriate phase centers $\mathcal{O}^1_{\text{TX}}, ..., \mathcal{O}^N_{\text{TX}}$ and $\mathcal{O}_{\text{RX}}$. The electric field generated by the transmitters is given by the Electric Field Integral Equation (EFIE):

$$\mathbf{e}(\mathbf{r}) = -j\omega\mu \int_V \mathcal{G}(\mathbf{r}, \mathbf{r}') \cdot \mathbf{j}(\mathbf{r}') \, \mathrm{d}\mathbf{r}', \tag{3.1}$$

where $\mathbf{j}(\mathbf{r}')$ represents the current densities $\mathbf{j}^1_{\text{TX}}(\mathbf{r}'), \cdots, \mathbf{j}^N_{\text{TX}}(\mathbf{r}')$ on the transmitters and $\mathbf{j}_{\text{RX}}(\mathbf{r}')$ on the receiver. μ is the permeability of the background media, and $\mathcal{G}(\mathbf{r}, \mathbf{r}')$ the three-dimensional dyadic Green's function. The integration domain V extends over all devices, i.e. $V = (V^1_{\text{TX}} \cup \cdots \cup V^N_{\text{TX}}) \cup V_{\text{RX}}$. In this chapter we assume that the devices are spaced sufficiently far from each other, such that there is no coupling via the reactive near-field.

For such devices, positioned in each other's Fresnel or Fraunhofer region, the field incident on the receiving device can be accurately approximated by restricting V to $V_{\text{TX}} = \bigcup_{i=1}^{N} V^i_{\text{TX}}$ in (3.1). By applying Gegenbauer's addition theorem [2] to the

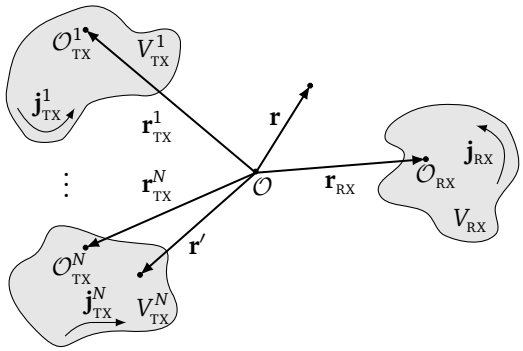

Figure 3.1: General configuration of interacting devices.

scalar 3-D Green's function and employing a plane wave expansion, the incoming electric field can be written in terms of incoming plane waves and outgoing plane waves:

$$\mathbf{e}^{\text{inc}}(\mathbf{r}) = -\frac{\omega\mu k}{(4\pi)^2}\sum_{i=1}^{N}\iint_{\Omega} e^{-j\mathbf{k}\cdot(\mathbf{r}-\mathbf{r}_{\text{RX}})}T(\mathbf{r}_{\text{TX,RX}}^i,\hat{\mathbf{k}})\Big[\mathcal{I}-\hat{\mathbf{k}}\hat{\mathbf{k}}\Big]\cdot\int_{V_{\text{TX}}^i} e^{j\mathbf{k}\cdot(\mathbf{r}'-\mathbf{r}_{\text{TX}}^i)}\mathbf{j}(\mathbf{r}')\,\mathrm{d}\mathbf{r}'\,\mathrm{d}\hat{\mathbf{k}}, \tag{3.2}$$

where we defined $\mathbf{r}_{\text{TX,RX}}^i = \mathbf{r}_{\text{RX}} - \mathbf{r}_{\text{TX}}^i$. Also, we integrate over the Ewald sphere Ω and $\mathbf{k} = k(\sin\theta\cos\phi\,\hat{\mathbf{x}} + \sin\theta\sin\phi\,\hat{\mathbf{y}} + \cos\theta\,\hat{\mathbf{z}})$ is the wave vector in spherical coordinates, with $k = \omega\sqrt{\epsilon\mu}$ the wavenumber of the background medium and ϵ its permittivity. Furthermore, $\mathcal{I}$ is the unit dyadic and $T(\mathbf{r}_{\text{TX,RX}}^i,\hat{\mathbf{k}}) = \sum_{l=0}^{\infty}(2l+1)j^{-l}h_l^{(2)}(k|\mathbf{r}_{\text{TX,RX}}^i|)P_l(\hat{\mathbf{k}}\cdot\hat{\mathbf{r}}_{\text{TX,RX}}^i)$ the translation operator where $h_l^{(2)}(\cdot)$ is the l-th order spherical Hankel function of the second kind and $P_l(\cdot)$ the Legendre polynomial of degree l. The radiation pattern of any transmitting antenna i is defined as

$$\mathbf{F}_{\text{TX}}^i(\hat{\mathbf{k}}) = \frac{j\omega\mu}{4\pi}\hat{\mathbf{k}}\times\Big[\hat{\mathbf{k}}\times\int_{V_{\text{TX}}^i} e^{j\mathbf{k}\cdot(\mathbf{r}'-\mathbf{r}_{\text{TX}}^i)}\mathbf{j}(\mathbf{r}')\,\mathrm{d}\mathbf{r}'\Big], \tag{3.3}$$

and similarly for the radiation pattern of the receiver.

Using these, the incident electric field (3.2) can be written in terms of the radiation patterns of the devices in the system. Assume now, for simplicity, that the transmitters and receiver are one-port devices. Then, an equivalent circuit representation of this configuration is as shown in Fig. 3.2, where Z_{TX}^i and Z_{RX} are the radiation impedances of transmitter i and the receiver respectively. Transmitter i is driven by means of a Thévenin generator composed of a sinusoidal voltage source V_g^i with internal impedance Z_g^i. The Norton equivalent of the receiver consists of a load

impedance Z_L and a short-circuit current I_{sc}. Using the modified expression for the incoming electric field, we obtain a simplified expression for the short-circuit current induced on the receiver by multiple transmitters [3]:

$$I_{sc} = -\frac{1}{ZV_0} \iint_{\Omega} \sum_{i=1}^{N} T(\mathbf{r}^i_{\mathrm{TX,RX}}, \hat{\mathbf{k}}) \mathbf{F}^i_{\mathrm{TX}}(\hat{\mathbf{k}}) \cdot \mathbf{F}_{\mathrm{RX}}(-\hat{\mathbf{k}}) \, \mathrm{d}\hat{\mathbf{k}}, \tag{3.4}$$

where $Z = \sqrt{\frac{\mu}{\epsilon}}$ is the wave impedance of the background medium and V_0 the pertinent normalization factor, evolving from the reciprocity theorem, depending on the normalized radiation pattern when operating antenna i is in transmit mode. As the antennas' radiation patterns scale with V_0, this parameter can be chosen to be 1 V.

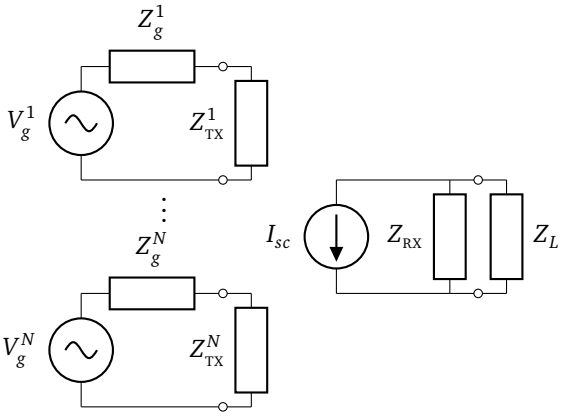

Figure 3.2: Equivalent circuit of the interaction between devices when there are multiple transmitters.

In practice, (3.4) can only be approximated since the infinite sum that occurs in the translation operator has to be truncated to a finite number of multipoles L. How to select this number, and what accuracy it entails is explained in [2].

In summary we can say that in order to calculate the influence of transmitting (noisy) devices on a receiving (susceptible) device, only the measured or simulated radiation patterns of the devices are needed. Furthermore, these devices may be positioned anywhere in space, as long as there is no coupling via the reactive near-field. This leads to very efficient calculations for multiple transmitter scenarios, in comparison to full-wave solutions, especially when one or more of the devices is repeatedly repositioned in space.

We will now expand the above method into a formalism that is of practical use for the analysis of the EMC behavior of devices and systems. To mimic compliance tests for the assessment of radiated emission or immunity in anechoic chambers,

we need the ability to efficiently rotate the devices about their phase center. This can be done by applying the appropriate rotation $\mathcal{R}$ to the radiation patterns of the devices. The rotation is efficiently performed in the spherical harmonics domain ($\mathcal{R}_{SH}$), as shown in Fig 3.3. The transformation to the spherical harmonics domain $\mathcal{F}$ and its inverse $\mathcal{F}^{-1}$ are given by (3.5) and (3.6), respectively:

$$\begin{Bmatrix} A_{pq} \\ B_{pq} \end{Bmatrix} = \frac{-1}{p(p+1)} \int_0^{2\pi} \int_0^{\pi} \Bigg[q \begin{Bmatrix} jF_\phi(\theta,\phi) \\ -F_\theta(\theta,\phi) \end{Bmatrix} Y^*_{pq}(\theta,\phi) + \sin\theta \begin{Bmatrix} -F_\theta(\theta,\phi) \\ jF_\phi(\theta,\phi) \end{Bmatrix} \frac{\mathrm{d}Y^*_{pq}(\theta,\phi)}{\mathrm{d}\theta} \Bigg] \mathrm{d}\theta \mathrm{d}\phi, \tag{3.5}$$

$$\begin{Bmatrix} F_\theta(\theta,\phi) \\ F_\phi(\theta,\phi) \end{Bmatrix} = \sum_{p=0}^{P} \sum_{|q|\leq p} \Bigg[\begin{Bmatrix} A_{pq} \\ jB_{pq} \end{Bmatrix} \frac{\mathrm{d}Y_{pq}(\theta,\phi)}{\mathrm{d}\theta} + \begin{Bmatrix} B_{pq} \\ jA_{pq} \end{Bmatrix} \frac{qY_{pq}(\theta,\phi)}{\sin\theta} \Bigg]. \tag{3.6}$$

Here, $Y_{pq}(\theta,\phi)$ are the orthonormalized scalar spherical harmonics and P is a parameter that determines the accuracy. In Fig. 3.3, the transformation $\mathcal{R}$ represents the desired rotation in the spatial domain. The rotation itself is performed in the spherical harmonics domain by the transformation $\mathcal{R}_{SH}$ that makes use of Wigner D-matrices. The rotated coefficients of the spherical harmonics expansion are calculated as

$$\begin{Bmatrix} A^{\mathcal{R}}_{pq} \\ B^{\mathcal{R}}_{pq} \end{Bmatrix} = \begin{Bmatrix} A_{pq} \\ B_{pq} \end{Bmatrix} \sum_{|r|\leq p} e^{-jq\gamma} d^r_{pq}(\beta) e^{-jr\alpha}, \tag{3.7}$$

with $d^r_{pq}(\beta)$ the Wigner small d-matrix, given by

$$d^r_{pq}(\beta) = (-1)^{r-q} \sqrt{(p+r)!(p-r)!(p+q)!(p-q)!} \cdot \sum_s (-1)^s \frac{\left(\cos\frac{\beta}{2}\right)^{2(p-s)+q-r} \left(\sin\frac{\beta}{2}\right)^{2s-q+r}}{(p+q-s)!s!(r-q+s)!(p-r-s)!}. \tag{3.8}$$

Here, the range of s is determined by the condition that all factorials are nonnegative, thus $s \in [\max(0, q-r), \min(p+q, p-r)]$. In (3.7)-(3.8), α, β and γ are the

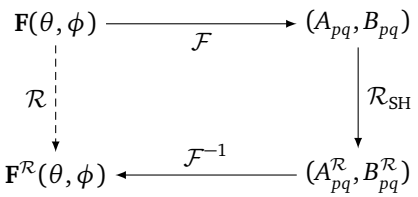

Figure 3.3: Rotation of $\mathbf{F}(\theta,\phi)$ to $\mathbf{F}^{\mathcal{R}}(\theta,\phi)$ using the spherical harmonics domain.

standard Euler angles that define the rotation using the $z-y-z$ convention in a right-handed frame. The Euler angles (α, β, γ) are readily related to the desired inclination and azimuthal angles θ and ϕ, by choosing $\alpha = \phi$, $\beta = \theta$ and $\gamma = 0$.

3.3 Validation Example

In order to validate the formalism, a numerical experiment is performed with half-wavelength dipole antennas. In this example, as shown in Fig. 3.4, two transmitters are placed at positions $\mathbf{r}_{\text{TX}}^1 = \lambda\hat{\mathbf{x}}$ and $\mathbf{r}_{\text{TX}}^2 = -\lambda\hat{\mathbf{x}}$ while the receiver is located at $\mathbf{r}_{\text{RX}} = \lambda\hat{\mathbf{y}}$. The short-circuit current I_{sc} obtained with our method as shown in (3.4)

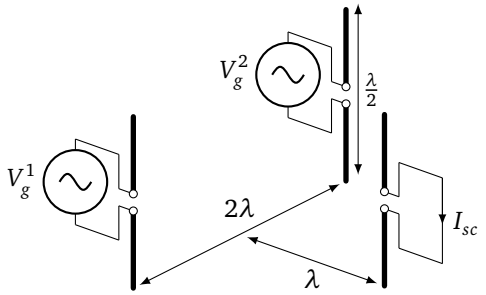

Figure 3.4: Configuration of the validation example with two transmitters and one receiver.

is compared to the Method of Moments (MoM) reference solution for arbitrary thin wires (see Appendix B and [4]). The wire thickness used in this example equals $10^{-4}\lambda$ and the MoM simulation uses five segments to model one dipole. The example in Fig. 3.4 is comparable to the equivalent circuit shown in Fig. 3.2 with $N = 2$ and $Z_g^1 = Z_g^2 = Z_L = 0\,\Omega$. The excitation voltages between the terminals of the transmitters are chosen $V_g^1 = V_g^2 = 1\,\text{V}$. In the MoM simulation, the short-circuit current is calculated directly by inverting the full MoM matrix equation.

To verify our novel method, with rotations performed using spherical harmonics, we start from the dipole's radiation pattern $\mathbf{F}(\theta, \phi)$. This radiation pattern is obtained via a MoM simulation for a *single* dipole. This radiation pattern is decomposed into spherical harmonics by (3.5) and afterwards rotated using (3.7). Subsequently, the rotated radiation patterns $\mathbf{F}^{\mathcal{R}}(\theta, \phi)$ are reconstructed using (3.6) and finally substituted into (3.4) to calculate the short-circuit current I_{sc}. For this example we rotate the receiving dipole over Euler angles $\alpha = \beta = \gamma$, varying from 0 till 2π for which we use $P = L = 2$. A comparison between the short-circuit current obtained from the MoM simulation and the novel spherical harmonics method is given in Fig. 3.5, where an excellent agreement is observed. The MoM simulation over all angles took 84.73 s whereas the novel method only took 1.63 s. Hence, an impressive speed-up factor of about 50 is achieved. In addition to the much shorter simulation times, only the $(P+1)^2$ coefficients A_{pq} and B_{pq} have to be stored to

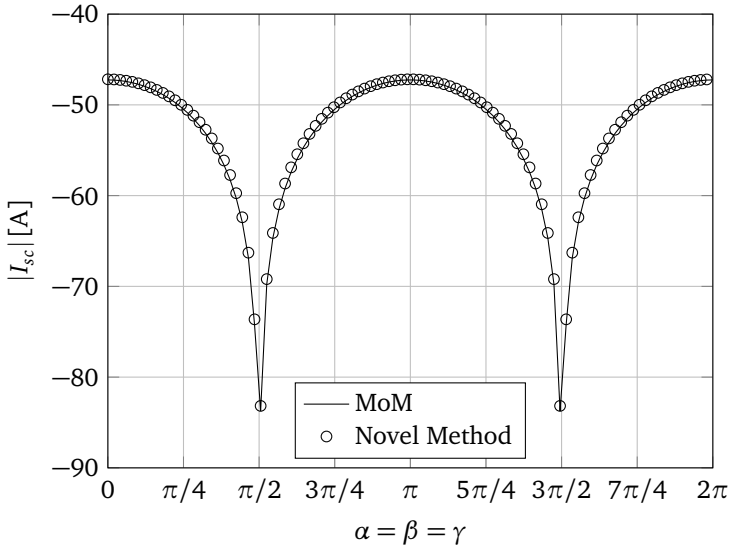

Figure 3.5: Amplitude of the short-circuit current at the port of the receiving dipole. The receiving dipole is rotated over Euler angles $\alpha = \beta = \gamma$.

simulate any situation with relative position and orientation. All simulations have been carried out on an Intel® Core™ i7-2600 processor running at 3.40 GHz and with 16 GB of memory.

3.4 Application Example

To demonstrate the practicability of the developed formalism, a measurement has been performed in an anechoic chamber. In this example, a Standard Gain Horn (SGH) acts as the receiver, while two microstrip patch antennas act as two non-collocated noise sources. The measurement setup is shown in Fig. 3.6. The two microstrip patch antennas are placed symmetrically around the SGH, and are rotated about 68 degrees towards the SGH. The distance between the two phase centers of the patch antennas is $d_{\text{patch–patch}} = 2.55\,\text{m}$, while the distance between the phase center of a patch antenna and the phase center of the SGH equals $d_{\text{patch–SGH}} = 3.45\,\text{m}$. During the measurement, the polarisation of the transmitter is altered by rotating the SGH around the axis of its main beam from $-\pi$ to π. For every orientation, the scattering parameters between the antennas are measured for comparison with simulation. The SGH and patch antennas are all designed to radiate at 1.5 GHz. In simulation, the rotation is performed using spherical harmonics and Wigner-D rotation matrices. The radiation patterns of the SGH and patch antennas are obtained from an analytical solution and a simulation with the 3-D planar full wave solver Momentum from Advanced Design System (ADS) of

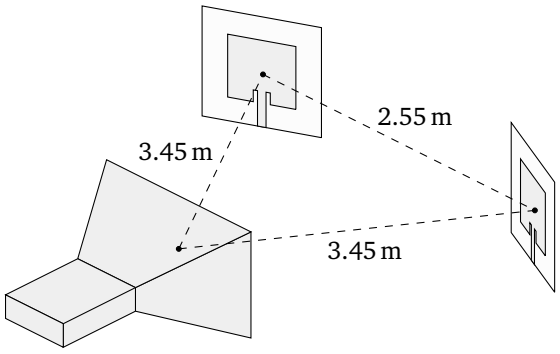

Figure 3.6: Measurement setup where a SGH is influenced by two patch antennas acting as non-collocated noise sources.

Keysight Technologies, respectively. The obtained link between one of the patch antennas and the SGH is shown in Fig. 3.7, where $P = L = 5$. An excellent agree-

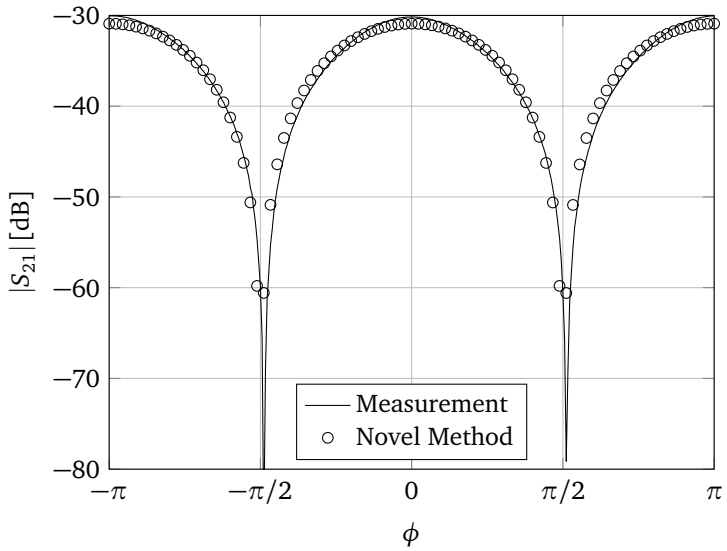

Figure 3.7: The measured and simulated ($P = L = 5$) link between one of the noise sources and the SGH. The SGH is rotated over $-\pi \leq \phi \leq \pi$.

ment between measurement and simulation is obtained. For $\phi = 0$ the difference between measurement and simulation is even smaller than 1 dB.

3.5 Conclusions

In this chapter we have presented a method that allows to determine the electromagnetic interference induced on a device in the presence of multiple non-collocated noise sources. The method solely relies on a single measurement or simulation of the radiation patterns of the devices in the system. Afterwards, the devices can, as long as there is no coupling via the reactive near-field, be positioned anywhere in space and given an arbitrary orientation without requiring completely new simulations, reducing the computational complexity of our method as compared to a full-wave solver.

References

[1] G.-J. Stockman, H. Rogier, and D. Vande Ginste, "Efficient modeling of interactions between radiating devices with arbitrary relative positions and orientations", *IEEE Transactions on Electromagnetic Compatibility*, vol. 56, no. 6, pp. 1313–1321, Dec. 2014.

[2] W. C. Chew, J.-M. Jin, E. Michielssen, and J. Song, *Fast and efficient algorithms in computational electromagnetics*. Artech House Publishers, 2001.

[3] J. Van Bladel, "On the equivalent circuit of a receiving antenna", *IEEE Antennas and Propagation Magazine*, vol. 44, no. 1, pp. 164–165, Feb. 2002.

[4] W. C. Gibson, *The Method of Moments in Electromagnetics*. Chapman & Hall/CRC, 2008, ch. 4, pp. 73–79.

4

Efficient Full-Wave Modeling of Radiative Near-Field Interactions in Semi-Anechoic Conditions

Based on "Efficient full-wave modeling of radiative near-field interactions in semi-anechoic conditions," Gert-Jan Stockman, Hendrik Rogier and Dries Vande Ginste, *Proceedings of the IEEE International Symposium on Electromagnetic Compatibility and EMC Europe*, pp. 524-528, August 2015.

★ ★ ★

In this chapter, a full-wave method to efficiently compute the electromagnetic interaction between two devices placed in semi-anechoic conditions is proposed. The aim of this research is the accurate and efficient reproduction of radiated immunity and emission tests in simulation. The employed technique relies on a single simulation (or measurement) of the radiation pattern of each device and allows an arbitrary relative position between the devices. The resulting procedure is practical, has a low computational cost, and shows good agreement with reference solutions.

4.1 Introduction

Design of electronic applications requires profound inspection of the Electromagnetic Compatibility (EMC) behavior of the system, not only to obtain reliable and

robust design, but also to pass legislative and regulatory requirements. Looking at Electromagnetic Interference (EMI), both radiated emission and susceptibility aspects require careful examination. Compliance tests for the assessment of radiated emission or immunity are often carried out in an anechoic chamber. The Device Under Test (DUT) is then rotated and a new measurement is performed for every angular position. Semi-anechoic chambers are used as well, especially for measurements at lower frequencies (low kHz or even low Hz range). Standards for this low range do not specify a need for absorption or anechoic behavior since the current absorber technology cannot deliver absorption for these frequencies [1]. Furthermore semi-anechoic chambers are much more practical when performing tests on large objects such as cars.

The goal is to take radiated emission and immunity into account during the design phase (or pre-compliance phase). In the ideal case, this is done via simulations, although often not a trivial task. A single simulation requires large computational resources in order to achieve accurate results.

To relax these high computational requirements, many methods have been developed to mimic (aspects of) the large electromagnetic problem. In [2] and [3] different emission models are described. When looking at susceptibility, various hybrid techniques have been proposed. In [4], model-reduction techniques are combined with full-wave solvers. In [5], a hybrid method, based on the Finite-Difference Time-Domain (FDTD) algorithm and a field coupling model of transmission lines are employed. Furthermore, [6] and [7] discuss susceptibility of transmission line networks with linear/nonlinear load terminations. Another way to reduce computational resources is by so-called Domain Decomposition Methods (DDMs). Nonconformal Finite Element (FE)-based DDMs have been reported in [8] and [9]. Furthermore, interactions have also been described via a hybrid Physical Optics (PO)/generalized-scattering-matrix approach [10]. Recently, in [11], a DDM-like approach was suggested to model interactions by using eigenmodal expansions. In [12], multilayer high-speed interconnects are modelled using modal ports.

In this chapter, we will not consider emission or susceptibility separately, but the electromagnetic interaction between radiating devices. The novelty of our method lies in the fact that it is based purely on a single simulation (or measurement) of the radiation patterns of each individual device. Besides reducing the computational burden of modeling an entire set-up, another advantage is that the devices may be moved without requiring new simulations (or measurements). As such, the technique is very tractable and opens the way to the efficient reproduction of radiated emission and immunity tests in simulations.

Work related to this topic has already been performed in [13]. The modeling of the interaction between two single-port radiating devices (in the radiative near-field, also known as the Fresnel region) that have arbitrary relative positions and orientations in free space (anechoic conditions) was described. The difference w.r.t. this work is that we expand the formalism to account for *semi*-anechoic conditions,

maintaining the efficiency and accuracy of the advocated method.

In Section 4.2, the electromagnetic interaction between devices in semi-anechoic conditions is described and the formalism to efficiently calculate them is explained. Section 4.3 contains a validation example to prove the correctness of our technique, whereas in Section 4.4 some application examples are considered, showing its applicability. The conclusion to this work is given in Section 4.5.

In the sequel, all sources and fields are assumed to be time harmonic with angular frequency ω and time dependencies $e^{j\omega t}$ are suppressed. Unit vectors are denoted with a "hat", e.g. $\hat{\mathbf{v}}$.

4.2 Formalism

The general problem geometry for the case of a transmitting and receiving device placed in semi-anechoic conditions is shown in Fig. 4.1. The devices are represented by their current density sources $\mathbf{j}_{\text{TX}}(\mathbf{r}')$ for the transmitter and $\mathbf{j}_{\text{RX}}(\mathbf{r}')$ for the receiver. Due to the presence of the Perfect Electric Conductor (PEC) floor, an image source mirrored around the PEC floor (Fig. 4.2) is presented by means of the current density $\mathbf{j}^m_{\text{TX}}(\mathbf{r}'')$. Throughout the rest of this chapter, the superscript m will be used to denote the mirrored fictitious device. The transmitter, mirrored transmitter and receiver are defined in volumes V_{TX},V^m_{TX} and V_{RX}, respectively and appropriate phase centers $\mathcal{O}_{\text{TX}}$, $\mathcal{O}^m_{\text{TX}}$ and $\mathcal{O}_{\text{RX}}$ are attached to them. The electric field

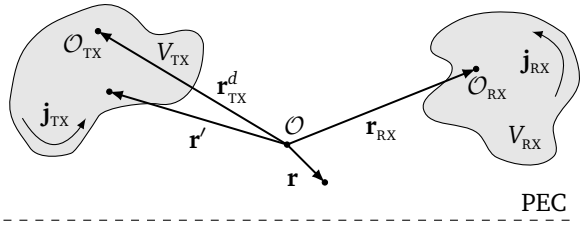

Figure 4.1: General configuration of interacting devices in a semi-anechoic chamber.

generated by the transmitter is given by the Electric Field Integral Equation (EFIE) [14]:

$$\mathbf{e}(\mathbf{r}) = -j\omega\mu \int_V \mathcal{G}_{\text{semi}}(\mathbf{r},\mathbf{r}') \cdot \mathbf{j}(\mathbf{r}')\, \mathrm{d}\mathbf{r}', \tag{4.1}$$

where $\mathbf{j}(\mathbf{r}')$ represents the current densities on all of the devices ($\mathbf{j}_{\text{TX}}(\mathbf{r}')$, $\mathbf{j}^m_{\text{TX}}(\mathbf{r}'')$ and $\mathbf{j}_{\text{RX}}(\mathbf{r}')$). μ is the permeability of the background media, and $\mathcal{G}_{\text{semi}}(\mathbf{r},\mathbf{r}')$ the three-

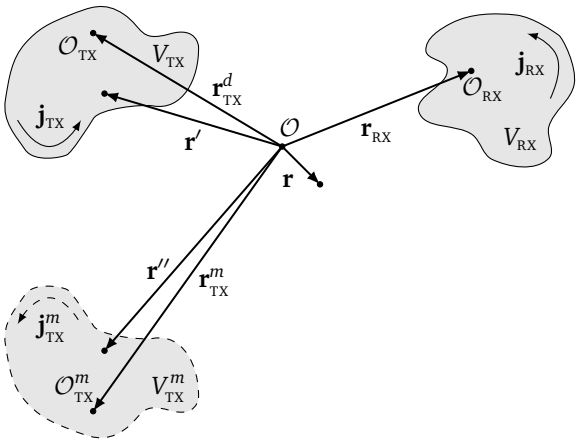

Figure 4.2: Equivalent configuration of the interacting devices in a semi-anechoic chamber (Fig. 4.1). The PEC floor is replaced by a mirrored image source.

dimensional dyadic Green's function in the semi-anechoic case, which equals

$$\mathcal{G}_{\mathrm{semi}}(\mathbf{r},\mathbf{r}') = \mathcal{G}_{\mathrm{anechoic}}(\mathbf{r},\mathbf{r}') + \mathcal{G}_{\mathrm{mirror}}(\mathbf{r},\mathbf{r}') \tag{4.2}$$

$$= \Big[\mathcal{I} + \frac{1}{k^2}\nabla\nabla\Big]\Big(\frac{e^{-jk|\mathbf{r}-\mathbf{r}'|}}{4\pi|\mathbf{r}-\mathbf{r}'|} - \frac{e^{-jk|\mathbf{r}-\mathbf{r}''|}}{4\pi|\mathbf{r}-\mathbf{r}''|}\Big), \tag{4.3}$$

with $\mathbf{r}'' = \mathbf{r}' - 2z'\hat{\mathbf{z}}$ and $z' = \mathbf{r}'\cdot\hat{\mathbf{z}}$ when the origin of the coordinate system is chosen to reside on the PEC plane.

The integration domain V in (4.1) extends over all devices, i.e. $V = V_{\mathrm{TX}} \cup V^m_{\mathrm{TX}} \cup V_{\mathrm{RX}}$. In this contribution, we assume that the devices are spaced sufficiently far from each other, such that there is no coupling via the reactive near-field. For such devices, positioned in each other's Fresnel or Fraunhofer region, the field incident on the receiving device can be accurately approximated by restricting V to $V_{\mathrm{TX}} \cup V^m_{\mathrm{TX}}$ in (4.1). By applying Gegenbauer's addition theorem [15] to the scalar 3-D Green's function and employing a plane wave expansion [16], the incoming electric field is written in terms of incoming and outgoing plane waves:

$$\begin{aligned}\mathbf{e}^{\mathrm{inc}}(\mathbf{r}) = -\frac{\omega\mu k}{(4\pi)^2}\iint_{\Omega} e^{-j\mathbf{k}\cdot(\mathbf{r}-\mathbf{r}_{\mathrm{RX}})}\Big[\mathcal{I}-\hat{\mathbf{k}}\hat{\mathbf{k}}\Big] \\ \cdot\Big[T(\mathbf{r}^d_{\mathrm{TX,RX}},\hat{\mathbf{k}})\int_{V_{\mathrm{TX}}} e^{j\mathbf{k}\cdot(\mathbf{r}'-\mathbf{r}_{\mathrm{TX}})}\mathbf{j}_{\mathrm{TX}}(\mathbf{r}')\,\mathrm{d}\mathbf{r}' \\ + T(\mathbf{r}^m_{\mathrm{TX,RX}},\hat{\mathbf{k}})\int_{V^m_{\mathrm{TX}}} e^{j\mathbf{k}\cdot(\mathbf{r}''-\mathbf{r}^m_{\mathrm{TX}})}\mathbf{j}^m_{\mathrm{TX}}(\mathbf{r}'')\,\mathrm{d}\mathbf{r}''\Big]\,\mathrm{d}\hat{\mathbf{k}},\end{aligned} \tag{4.4}$$

where we defined $\mathbf{r}^i_{\text{TX,RX}} = \mathbf{r}_{\text{RX}} - \mathbf{r}^i_{\text{TX}}$ with $i = \{m, d\}$. The superscript d refers to the direct transmitter, whereas superscript m refers to its image mirrored w.r.t. the PEC plane. According to image theory, the current density of the mirrored device $\mathbf{j}^m_{\text{TX}}(\mathbf{r}'')$ is linked to that of the direct transmitter $\mathbf{j}_{\text{TX}}(\mathbf{r}')$ as

$$\mathbf{j}^m_{\text{TX}}(\mathbf{r}'') = -\mathbf{j}_{\text{TX},t}(\mathbf{r}') + j_{\text{TX},z}(\mathbf{r}')\hat{\mathbf{z}}, \tag{4.5}$$

where the subscript t stands for the components tangential to the PEC plane. Furthermore, in (4.4), we integrate over the Ewald sphere Ω and $\mathbf{k}$ is the wave vector in spherical coordinates:

$$\mathbf{k} = k\hat{\mathbf{k}} = k(\sin\theta\cos\phi\,\hat{\mathbf{x}} + \sin\theta\sin\phi\,\hat{\mathbf{y}} + \cos\theta\,\hat{\mathbf{z}}), \tag{4.6}$$

with $k = \omega\sqrt{\epsilon\mu}$ the wavenumber of the background medium and ϵ its permittivity. Also, $\mathcal{I}$ is the unit dyadic and $T(\mathbf{r}^i_{\text{TX,RX}}, \hat{\mathbf{k}})$ the translation operator defined as

$$T(\mathbf{r}^i_{\text{TX,RX}}, \hat{\mathbf{k}}) = \sum_{l=0}^{\infty}(2l+1)j^{-l}h^{(2)}_l(k|\mathbf{r}^i_{\text{TX,RX}}|)P_l(\hat{\mathbf{k}}\cdot\hat{\mathbf{r}}^i_{\text{TX,RX}}), \tag{4.7}$$

where $h^{(2)}_l(\cdot)$ the l-th order spherical Hankel function of the second kind and $P_l(\cdot)$ the Legendre polynomial of degree l. The radiation pattern of the (mirrored) transmitting device is defined as

$$\mathbf{F}^i_{\text{TX}}(\hat{\mathbf{k}}) = \frac{j\omega\mu}{4\pi}\hat{\mathbf{k}}\times\Big[\hat{\mathbf{k}}\times\int_{V^i_{\text{TX}}} e^{j\mathbf{k}\cdot(\mathbf{r}'-\mathbf{r}^i_{\text{TX}})}\mathbf{j}^i_{\text{TX}}(\mathbf{r}')\,\mathrm{d}\mathbf{r}'\Big], \tag{4.8}$$

and the radiation pattern of the receiver can be written in a similar way.

Using these expressions, the incident electric field (4.4) is written in terms of the radiation patterns of the devices and a simplified expression for the short-circuit current induced on the receiver is obtained [17]:

$$I_{sc} = -\frac{1}{ZV_0}\sum_{i=\{d,m\}}\iint_{\Omega} T(\mathbf{r}^i_{\text{TX,RX}}, \hat{\mathbf{k}})\mathbf{F}^i_{\text{TX}}(\hat{\mathbf{k}})\cdot\mathbf{F}_{\text{RX}}(-\hat{\mathbf{k}})\,\mathrm{d}\hat{\mathbf{k}}, \tag{4.9}$$

where $Z = \sqrt{\frac{\mu}{\epsilon}}$ is the wave impedance of the background medium and V_0 a pertinent normalization factor, which evolves from the reciprocity theorem and depends on the normalized radiation pattern when antenna i is operating in transmit mode. As the antennas' radiation patterns scale with V_0, this parameter can be chosen to be 1 V.

In practice, (4.9) can only be approximated since the infinite sum that occurs in the translation operator (4.7) has to be truncated to a finite number of multipoles L. [15] explains how to select this number and the accuracy it entails.

It is interesting to note that in order to calculate the influence of transmitting (noisy) devices on a receiving (susceptible) device, in semi-anechoic conditions,

only the measured or simulated radiation patterns of the two devices are needed. The radiation pattern of the transmitter $\mathbf{F}^d_{\text{TX}}(\hat{\mathbf{k}})$ and the fictitious transmitter $\mathbf{F}^m_{\text{TX}}(\hat{\mathbf{k}})$ are linked to each other since the radiation pattern simply needs to be mirrored with respect to the PEC plane. Furthermore, the devices may be positioned anywhere in space, as long as there is no coupling via the reactive near-field. This leads to very efficient calculations in semi-anechoic conditions, in comparison to full-wave solutions, especially when one or both of the devices are repeatedly repositioned in space, i.e. when $\mathbf{r}^i_{\text{TX,RX}}$ is varied. The expression for the short-circuit current (4.9) can be modified to account only for purely anechoic conditions, by simply omitting the term that corresponds to the contribution of the mirrored device.

4.3 Validation Example

In order to validate the explained method, a numerical experiment is conducted where transmitter and receiver are both half-wavelength dipole antennas. The antennas are placed parallel to each other at a height of $h = 1\,\text{m}$ above an infinite PEC plane and separated by $d = 3\,\text{m}$ as shown in Fig. 4.3. The short-circuit current

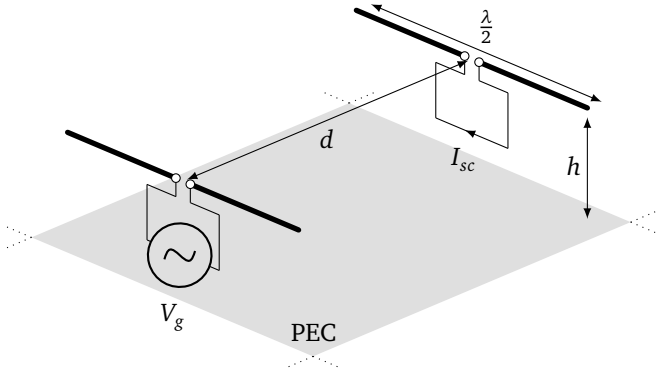

Figure 4.3: Two parallel half-wavelength dipole antennas (separated by a distance $d = 3\,\text{m}$) are placed in an semi-anechoic chamber with a height of $h = 1\,\text{m}$ above the infinite PEC floor.

I_{sc} calculated with our full-wave method (4.9) is compared to a reference solution obtained by a Method of Moments (MoM) for arbitrary thin wires (see Appendix B and [18]), but adapted to also account for the PEC plate. The thickness of the wires equals $10^{-4}\lambda$ and five segments are used to model a half-wavelength dipole. The transmitter is excited with $V_g = 1\,\text{V}$ between its terminals. The short-circuit current is found by inverting the full MoM matrix equation. The frequency (and thus also the physical length of the antenna) is swept and a comparison of the short-circuit current between the full-wave method and the MoM is made in Fig. 4.4. The radiation patterns used in the full-wave method are calculated from a straightforward MoM simulation for a single dipole. The number of multipoles used is $L = 5$. For

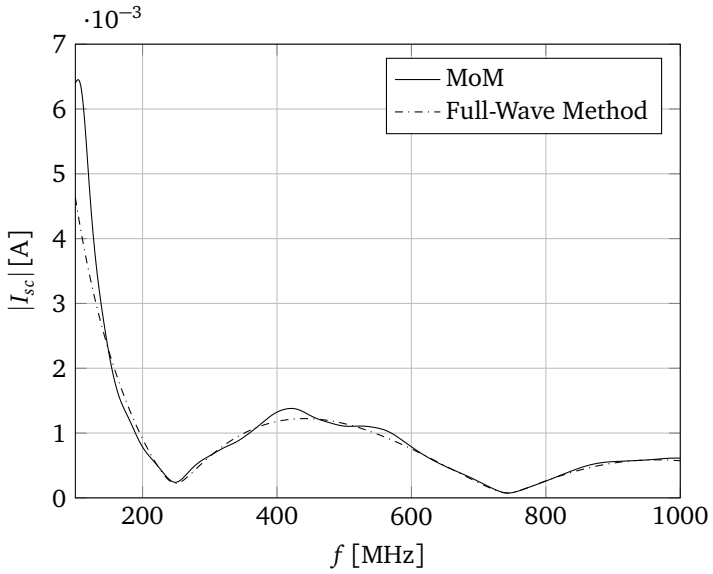

Figure 4.4: Comparison of the amplitude of the short-circuit current at the receiving dipole between the full-wave method and the traditional MoM.

low frequencies, and thus long wavelengths, the error starts to grow. The reason is that the electrical size of the antennas grows relative to their separation distance, which remains fixed to 3 m. The result is that the devices come in proximity of each other's *reactive* near field and the devices become tightly coupled. The same reasoning should be used for the transmitter and its mirrored version, who also become coupled. Traditionally, devices are considered to be in each other's *radiative* near-field, for distances between them not smaller than, say, $\lambda/6$ [19]. Then, they may be treated as being uncoupled and our formalism is valid. For coupled devices, the approximation made on the integration domain in (4.1) is no longer valid and a multiport formalism is necessary (see Chapter 5).

4.4 Application Example

4.4.1 Shielding efficiency

A small thin-wire electric dipole antenna with a length of 4 cm is put inside a PEC shielding enclosure. The enclosure is a 50 cm side cubic box with a horizontal aperture in the front plane having dimensions 20 cm × 5 cm, as depicted in Fig. 4.5. The dipole antenna inside the enclosure is excited and another identical dipole antenna, placed 3 m in front of the slot, acts as a receiver. The bottom of the box is placed at a height of 1 m above a PEC floor. As a first step, Computer Simulation Technology Microwave Studio (CST MWS) is used to calculate the radiation pat-

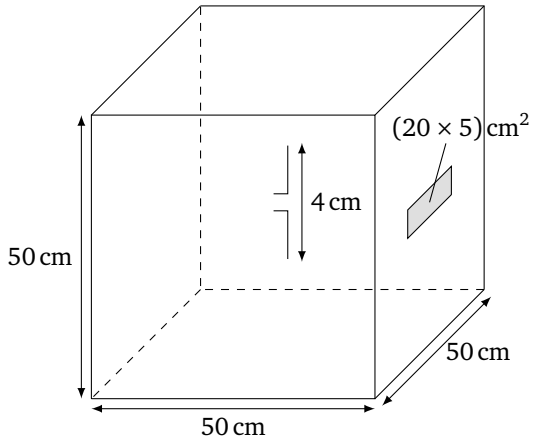

Figure 4.5: Small thin-wire electrical dipole antenna inside a PEC metallic shielding enclosure. The enclosure is a 50 cm side cubic box with a horizontal aperture in the front plane.

terns of the dipole antenna with and without the shielding enclosure (and without PEC plate). Subsequently, these radiation patterns are used as input for our full-wave method, allowing to efficiently calculate the short-circuit currents induced in the receiving dipole using (4.9). The short-circuit currents induced in the receiving antenna, are calculated with and without the shielding enclosure at the transmitter, leading to the currents $I_{sc,1}$ and $I_{sc,2}$ respectively. The Shielding Efficiency (SE) is defined as the ratio of the amplitude of these currents:

$$\mathrm{SE}\,[\mathrm{dB}] = 20\log_{10}\left(\frac{|I_{sc,2}|}{|I_{sc,1}|}\right). \tag{4.10}$$

The SE calculated over a broad frequency range is shown in Fig. 4.6. Besides a computation where the PEC plate is considered, the anechoic case, i.e. the box is put in free space, where the term that accounts for the mirrored device is ommited in (4.9), is also calculated and shown. For the highest frequency, i.e. 1 GHz, the order of expansion is $L = 18$. For the anechoic case, the obtained SE yields excellent agreement with the results shown in Fig. 5 of [20], proving the correctness of our method once again. Below 200 MHz, some small artifacts are visible, which are due to the radiation pattern simulations with CST MWS, suffering from inaccuracies as the bounding box is too small compared to the wavelength. Positioning the absorbing boundary conditions further away from the enclosure leads to unacceptably long simulaton times or even insufficient memory. This is also the reason why a complete set-up, including the receiving dipole antenna, cannot be simulated using CST MWS.

In the semi-anechoic case, the SE results are different, but the resonance peaks are not influenced. This is expected as these peaks only depend on the dimensions of

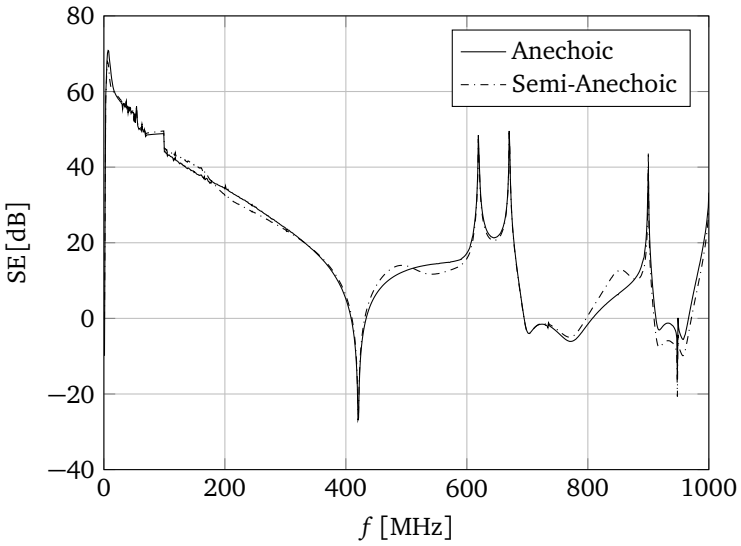

Figure 4.6: SE as a function of frequency for a 50 cm side cubic box with a 20 cm × 5 cm horizontal aperture centered in the front plane.

the cavity. To better show the difference between the anechoic and semi-anechoic conditions, the result is shown for a limited frequency range in Fig. 4.7. Differences of up to 5 dB are observed, showing the importance of being able to properly account for the PEC plane during EMC testing.

4.4.2 Fading in a semi-anechoic chamber

In a second example, we apply our theory to two identical inset-fed microstrip patch antennas, designed to resonate at 1.5 GHz. The antennas are placed $h = 1.75$ m above the PEC floor. The setup configuration is shown in Fig. 4.8. The distance d between the two antennas is varied within the range $[5\lambda, 10\lambda]$, and the influence of the reflection on the PEC floor is observed. To apply our method, the order of expansion is chosen to be $L = 10$. The radiation patterns of the antennas are extracted from the 3-D planar full-wave solver Momentum from Advanced Design System (ADS) of Keysight Technologies, since they were designed using this software package. The result is shown in Fig. 4.9. As expected, due to constructive and destructive interference of the multipath present in this scenario, fading is observed in the link between the two devices.

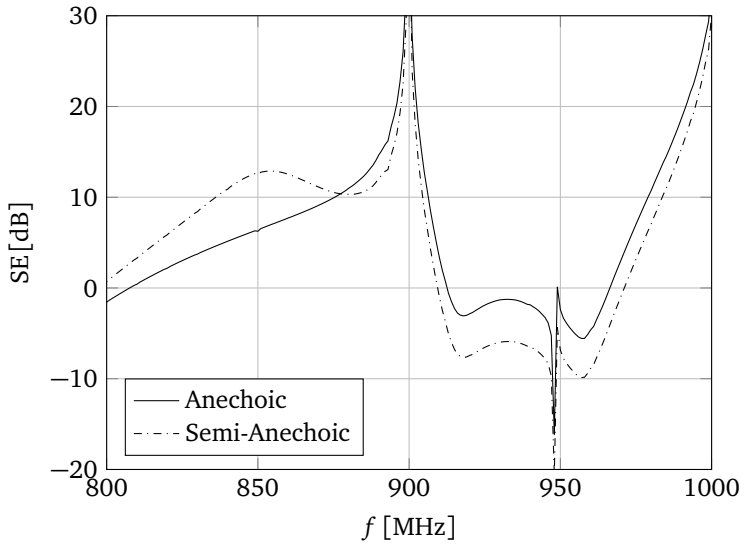

Figure 4.7: Limited frequency range of the result shown in Fig. 4.6.

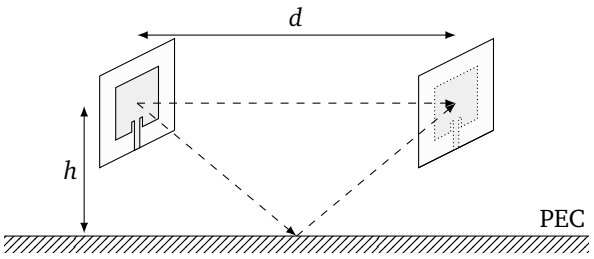

Figure 4.8: Setup of two inset-fed microstrip patch antennas in a semi-anechoic chamber.

4.5 Conclusions

The method developed in this chapter allows for the efficient and accurate reproduction of immunity and emission tests in semi-anechoic conditions. The method relies on a single simulation or measurement of the radiation patterns of the devices, as such avoiding to have to model an entire (electrically large) set-up. Another advantage this method has over traditional simulations or measurements is that a repositioning of the devices does not entail a completely new computation or measurement. The correctness of the method was shown using a numerical validation. Practical examples were given to show the method's applicability.

Right now, the approach is only accurate as long as the coupling between the devices remains small. In other words, the devices should not reside in each others

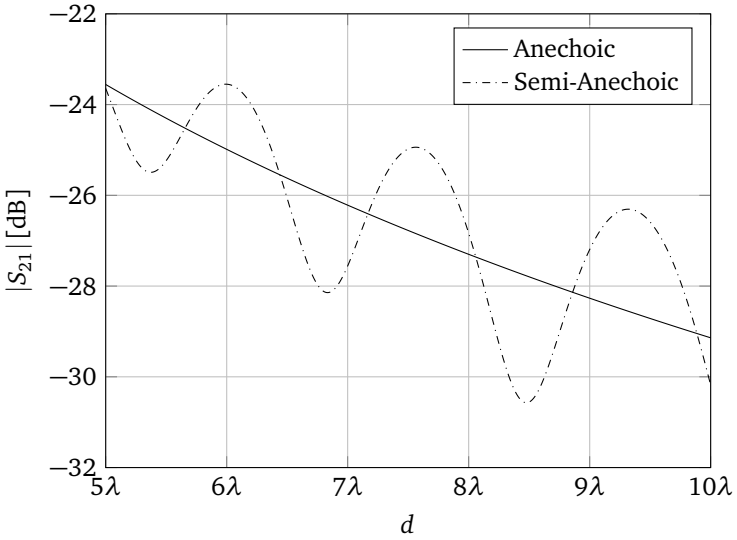

Figure 4.9: Comparison of the configuration shown in Fig. 4.8 with and without PEC plate.

reactive near field. As they approach this zone, the coupling cannot be neglected anymore and a multiport approach to the problem is necessary, as will be explained in Chapter 5.

References

[1] M. Wiles and V. Rodriguez, "Choosing the right chamber for your test requirements", *EMC Directory & Design Guide*, May 2010.

[2] P. Li and L. J. Jiang, "Source reconstruction method-based radiated emission characterization for PCBs", *IEEE Transactions on Electromagnetic Compatibility*, vol. 55, no. 5, pp. 933–940, Oct. 2013.

[3] P. Kralicek, W. John, R. De Smedt, K. Vervoort, and H. Garbe, "A voltage controlled emission model of electromagnetic emission of IC for system analysis", in *IEEE International Symposium on Electromagnetic Compatibility*, Montreal, Quebec, 13-17 Aug. 2001, pp. 1197–1202.

[4] I. Erdin, M. Nakhla, and R. Achar, "Circuit analysis of electromagnetic radiation and field coupling effects for networks with embedded full-wave modules", *IEEE Transactions on Electromagnetic Compatibility*, vol. 42, no. 4, pp. 449–460, Nov. 2000.

[5] M. Tang, J. Lu, J. Mao, and L. Jiang, "A systematic electromagnetic-circuit method for EMI analysis of coupled interconnects on dispersive dielectrics", *IEEE Transactions on Microwave Theory and Techniques*, vol. 61, no. 1, pp. 1–13, Jan. 2013.

[6] Y. Bayram and J. Volakis, "Hybrid S-parameters for transmission line networks with linear/nonlinear load terminations subject to arbitrary excitations", *IEEE Transactions on Microwave Theory and Techniques*, vol. 55, no. 5, pp. 941–950, May 2007.

[7] Z. Khan, Y. Bayram, and J. Volakis, "EMI/EMC analysis of printed circuit boards subject to near-zone illuminations", *IEEE Transactions on Electromagnetic Compatibility*, vol. 51, no. 2, pp. 406–408, May 2009.

[8] Y. Shao, Z. Peng, and J.-F. Lee, "Signal integrity analysis of high-speed interconnects by using nonconformal domain decomposition method", *IEEE Transactions on Components, Packaging and Manufacturing Technology*, vol. 2, no. 1, pp. 122–130, Jan. 2012.

[9] Z. Peng, K.-H. Lim, and J.-F. Lee, "Nonconformal domain decomposition methods for solving large multiscale electromagnetic scattering problems", *Proceedings of the IEEE*, vol. 101, no. 2, pp. 298–319, Feb. 2013.

[10] C. Della Giovampaola, E. Martini, A. Toccafondi, and S. Maci, "A hybrid PO/generalized-scattering-matrix approach for estimating the reflector induced mismatch", *IEEE Transactions on Antennas and Propagation*, vol. 60, no. 9, pp. 4316–4325, Sep. 2012.

[11] T. Flisgen, H. Glock, and U. Van Rienen, "Compact time-domain models of complex RF structures based on the real eigenmodes of segments", *IEEE Transactions on Microwave Theory and Techniques*, vol. 61, no. 6, pp. 2282–2294, Jun. 2013.

[12] H. Wu and A. Cangellaris, "A finite-element domain-decomposition methodology for electromagnetic modeling of multilayer high-speed interconnects", *IEEE Transactions on Advanced Packaging*, vol. 31, no. 2, pp. 339–350, May 2008.

[13] G.-J. Stockman, H. Rogier, and D. Vande Ginste, "Efficient modeling of interactions between radiating devices with arbitrary relative positions and orientations", *IEEE Transactions on Electromagnetic Compatibility*, vol. 56, no. 6, pp. 1313–1321, Dec. 2014.

[14] J. Van Bladel, *Electromagnetic Fields*. John Wiley & Sons, 2007.

[15] W. C. Chew, J.-M. Jin, E. Michielssen, and J. Song, *Fast and efficient algorithms in computational electromagnetics*. Artech House Publishers, 2001.

[16] J. Stratton, *Electromagnetic Theory*. McGraw-Hill, 1941.

[17] J. Van Bladel, "On the equivalent circuit of a receiving antenna", *IEEE Antennas and Propagation Magazine*, vol. 44, no. 1, pp. 164–165, Feb. 2002.

[18] W. C. Gibson, *The Method of Moments in Electromagnetics*. Chapman & Hall/CRC, 2008, ch. 4, pp. 73–79.

[19] C. Balanis, *Antenna Theory: Analysis and Design*. John Wiley & Sons, 2005.

[20] W. Wallyn, D. De Zutter, and H. Rogier, "Prediction of the shielding and resonant behavior of multisection enclosures based on magnetic current modeling", *IEEE Transactions on Electromagnetic Compatibility*, vol. 44, no. 1, pp. 130–138, Feb. 2002.

5

Full-Wave Modeling of Interacting Multiport Devices with Arbitrary Relative Positions and Orientations for Efficient EMI Assessment

Based on "Full-Wave modeling of interacting multiport devices with arbitrary relative positions and orientations for efficient EMI assessment," Gert-Jan Stockman, Sam Lemey, Hendrik Rogier and Dries Vande Ginste, *Accepted for publication in the IEEE Transactions on Electromagnetic Compatibility*.

★★★

A novel method to accurately and efficiently model the interaction between radiating devices is proposed. Whereas previous work of the authors dealt with singleport devices (antennas), this chapter constitutes an important extension to actual multiport devices, as such paving the way for electromagnetic interference assessment of real-life (sub)systems early in their design cycle. The method solely relies on the knowledge of the radiation patterns of the different ports of the devices, which can either be measured or simulated using a solver of choice. These patterns are then used to compute the electromagnetic interaction between the devices that may be positioned in each other's radiative near-field (Fresnel region) or far-field (Fraunhofer region). Furthermore, in the model, their relative positions and orientations can be altered at a very low computational cost. The technique is thoroughly validated and illustrated, demonstrating its appositeness to study the electromagnetic compatibility behavior of the multiport devices.

5.1 Introduction

Knowledge of the Electromagnetic Compatibility (EMC) behavior of devices and systems is of the utmost importance in high-speed, high-sensitivity and also general electronic applications. Concerning Electromagnetic Interference (EMI) and EMC aspects, it is critical to design reliable and robust products, and also to pass legislative and regulatory requirements. Traditionally, the radiated emission or immunity behavior is characterized in an anechoic or semi-anechoic chamber, where the Device Under Test (DUT) is rotated, and a new measurement is performed for every angular position. Nowadays, it is well-known that the success or failure of a product regarding EMC, is already partially determined during the design phase (or pre-compliance phase). Computer-aided design can take radiated emission and immunity into account numerically early enough during the development of the product, but this is not a trivial task since even a single simulation often requires a large amount of computational resources in order to achieve reliable results. Moreover, to study the entire EMC behavior, the analysis needs to happen for many angular positions of the DUT, and a lot of (computationally expensive) simulations are needed.

Of course, several numerical techniques exist that relax these high computational requirements. First of all, to analyze emission, equivalent model or model-reduction techniques may reduce the complexity of the problem [1], [2]. Furthermore, when looking at susceptibility, various hybrid techniques have been proposed that combine full-wave methods with model-reduction techniques [3], [4] or that use an extended S-parameter model [5], [6]. Another way to deal with the high computational demands is by using Domain Decomposition Methods (DDMs). These methods tackle a problem by dividing it into several subproblems, which are individually solved in an efficient way, and afterwards recombined to assess the global behavior [7]–[11].

In previous work [12], [13], a formalism to efficiently model electromagnetic (EM) interactions between two singleport devices in (semi-)anechoic conditions was presented. This approach is valid for devices that are positioned in each other's far-field (Fraunhofer region) or radiative near-field (Fresnel region). In [14], this approach was extended to allow for any number of singleport devices.

In this chapter, we extend the formalism for *single*port to *multi*port devices. Such a multiport device may consist of physically separate devices, e.g. an array of antennas, or it can just as well be an electronic circuit (with multiple ports) on a Printed Circuit Board (PCB). The main difference with previous approaches is that, now, crosstalk between ports can be taken into account. This enables efficient intra-system modeling of the EMI (both emission and susceptibility) of several subsystems constituting an entire system, and also inter-system modeling of real-life complex products, thus characterizing their EMC behavior early in the design cycle. The novel method requires only a single simulation (or measurement) of the radiation patterns of each multiport. Moreover, rotation of these multiports is made tractable by leveraging a spherical harmonics expansion together with Wigner-D matrices. Furthermore, efficient repositioning of devices relative to each other is possible, also without a high computational cost. The advocated method is carefully validated concerning its accuracy and efficiency, and a state-of-the-art application example shows its appositeness.

This chapter is organized as follows. In Section 5.2 the novel extended formalism which describes the EM interaction between multiports as well as their rotation over arbitrary angles is explained. Sections 5.3 and 5.4 give a thorough validation and illustration. Conclusions are presented in Section 5.5. In the sequel, all sources and fields are assumed to be time harmonic with angular frequency ω and time dependencies $e^{j\omega t}$ are suppressed. Unit vectors are denoted with a "hat", e.g. $\hat{\mathbf{v}}$.

5.2 Formalism

5.2.1 Problem description

Consider the general problem geometry of two multiport devices (Fig. 5.1). An N-port and an M-port are arbitrarely positioned in space and they are electromagnetically interacting with each other. Each multiport device is assigned a phase center, $\mathcal{O}_{\text{TX}}$ or $\mathcal{O}_{\text{RX}}$, at positions $\mathbf{r}_{\text{TX}}$ and $\mathbf{r}_{\text{RX}}$ respectively. These phase centers are the points from/about which translations and rotations of the multiport devices will be performed later on.

When considering, e.g., the N-port as a transmitting (TX) device, i.e., the source of the disturbance, the goal is to efficiently and accurately compute its influence at all ports of the receiving (RX) M-port, i.e., the victim of the disturbance.

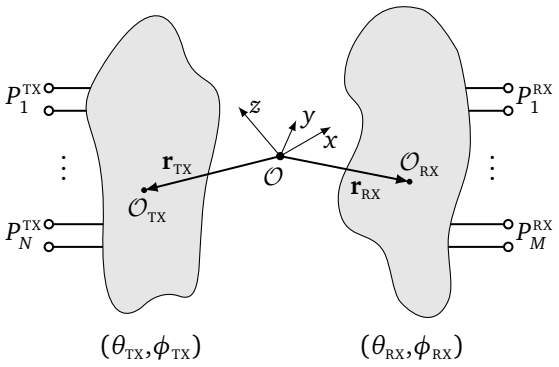

Figure 5.1: Schematic representation of an N-port device interacting with an M-port device. Each multiport device may be rotated over arbitrary angles (θ_{TX}, ϕ_{TX}) and (θ_{RX}, ϕ_{RX}) about their respective phase centers $\mathcal{O}_{TX}$ and $\mathcal{O}_{RX}$.

5.2.2 Electromagnetic interaction between multiport devices

In [12] and [13] it was shown, for *single*port devices ($N = M = 1$), placed in each other's radiative near-field (Fresnel zone), that the short-circuit current induced at the port of the receiving device is given by

$$I_{sc} = \frac{-1}{Z_c V_0} \iint_{\Omega} T(\mathbf{r}_{TX,RX}, \hat{\mathbf{k}}) \mathbf{F}_{TX}(\hat{\mathbf{k}}) \cdot \mathbf{F}_{RX}(-\hat{\mathbf{k}}) \, \mathrm{d}\hat{\mathbf{k}}. \tag{5.1}$$

Here, Z_c is the wave impedance of the background medium and V_0 is a pertinent normalization factor. The integration in (5.1) is performed over the Ewald sphere Ω. $\mathbf{F}_{TX}(\hat{\mathbf{k}})$ and $\mathbf{F}_{RX}(\hat{\mathbf{k}})$ represent the radiation patterns of the transmitting and receiving device in the direction $\hat{\mathbf{k}} = \sin\theta\cos\phi\,\hat{\mathbf{x}} + \sin\theta\sin\phi\,\hat{\mathbf{y}} + \cos\theta\,\hat{\mathbf{z}}$, i.e., the unit wave vector in spherical coordinates. The translation operator $T(\mathbf{r}_{TX,RX}, \hat{\mathbf{k}})$ is given by

$$T(\mathbf{r}_{TX,RX}, \hat{\mathbf{k}}) \approx \sum_{l=0}^{L} (2l+1) j^{-l} h_l^{(2)}(k|\mathbf{r}_{TX,RX}|) P_l(\hat{\mathbf{k}} \cdot \hat{\mathbf{r}}_{TX,RX}). \tag{5.2}$$

Here, $h_l^{(2)}(\cdot)$ is the l-th order spherical Hankel function of the second kind and $P_l(\cdot)$ the Legendre polynomial of degree l. The number of multipoles L truncates the sum and determines its accuracy. Traditional guidelines to select this number can be used [15]. The vector $\mathbf{r}_{TX,RX} = \mathbf{r}_{RX} - \mathbf{r}_{TX}$ represents the relative positions between the devices' phase centers.

Consequently, for interacting *multi*ports as shown in Fig. 5.1, the short-circuit cur-

rent $I_{sc}^{(m)}$ induced at port P_m^{RX} of the receiving multiport is given by

$$I_{sc}^{(m)} = \frac{-1}{Z_c V_{0,m}} \iint_{\Omega} T(\mathbf{r}_{\mathrm{TX,RX}}, \hat{\mathbf{k}}) \mathbf{F}_{\mathrm{TX}}(\hat{\mathbf{k}}) \cdot \mathbf{F}_{\mathrm{RX}}^{(m)}(-\hat{\mathbf{k}}) \, \mathrm{d}\hat{\mathbf{k}}. \tag{5.3}$$

It is very important to note that in (5.3), the radiation vector $\mathbf{F}_{\mathrm{TX}}(\hat{\mathbf{k}})$ is the *total* radiation pattern of the transmitting multiport device, taken into account the excitation at each of its N ports. In contrast, $\mathbf{F}_{\mathrm{RX}}^{(m)}(-\hat{\mathbf{k}})$ is the m-th *embedded* radiation pattern of the multiport. As this is quite different and more intricate than was the case for singleport devices [12], [13], the entire Sections 5.2.4 and 5.2.5 will be devoted to the computation of these radiation patterns.

5.2.3 Translation and rotation of the devices

The translation operation $T(\mathbf{r}_{\mathrm{TX,RX}}, \hat{\mathbf{k}})$ enables the repositioning of devices relative to each other, by simply altering their phase centers and thus $\mathbf{r}_{\mathrm{TX,RX}}$. For each repositioning, only the translation operator has to be recalculated. This does not entail a high computational cost, as compared to a new simulation (needed by other full-wave methods) or a new measurement. This will be demonstrated further in Sections 5.3 and 5.4.

Furthermore, rotation of devices, typically needed during EMI assessment, can be performed at a low cost as well, by making use of a spherical harmonics expansion. Consider a multiport device with an embedded radiation pattern $\mathbf{F}^{(m)}(\hat{\mathbf{k}})$ $(m = 1, ..., M)$. Then, the rotated embedded radiation pattern $\mathbf{F}^{(m),\mathcal{R}}(\hat{\mathbf{k}})$, for any arbitrary orientation of the multiport, is efficiently computed by going to the spherical harmonics domain, following the scheme shown in Fig. 5.2. The transforma-

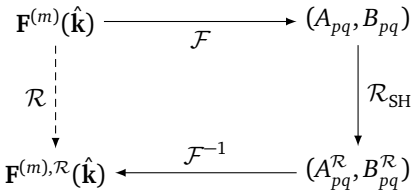

Figure 5.2: Rotation of $\mathbf{F}^{(m)}(\hat{\mathbf{k}})$ to $\mathbf{F}^{(m),\mathcal{R}}(\hat{\mathbf{k}})$ using the spherical harmonics domain.

tion $\mathcal{R}$ mapping $\mathbf{F}^{(m)}(\hat{\mathbf{k}})$ onto its rotated version $\mathbf{F}^{(m),\mathcal{R}}(\hat{\mathbf{k}})$ in the spatial domain, is equivalent to a transformation $\mathcal{R}_{\mathrm{SH}}$, converting a set of coefficients (A_{pq}, B_{pq}) into a new set of coefficients $(A_{pq}^{\mathcal{R}}, B_{pq}^{\mathcal{R}})$ in the spherical harmonics domain. The rotation $\mathcal{R}_{\mathrm{SH}}$ itself is performed using Wigner-D matrices [16], [17]:

$$\mathcal{R}_{\mathrm{SH}} \longleftrightarrow \begin{Bmatrix} A_{pq}^{\mathcal{R}} \\ B_{pq}^{\mathcal{R}} \end{Bmatrix} = \begin{Bmatrix} A_{pq} \\ B_{pq} \end{Bmatrix} \sum_{|r| \leq p} e^{-jq\gamma} d_{pq}^{r}(\beta) e^{-jr\alpha}, \tag{5.4}$$

with $d^r_{pq}(\beta)$ the Wigner small d-matrix, given by

$$d^r_{pq}(\beta) = (-1)^{r-q}\sqrt{(p+r)!(p-r)!(p+q)!(p-q)!}$$
$$\cdot\sum_s (-1)^s \frac{\left(\cos\frac{\beta}{2}\right)^{2(p-s)+q-r}\left(\sin\frac{\beta}{2}\right)^{2s-q+r}}{(p+q-s)!s!(r-q+s)!(p-r-s)!}. \tag{5.5}$$

Here, the range of s is determined by the condition that all factorials are non-negative, thus $s \in [\max(0, q-r), \min(p+q, p-r)]$. α, β and γ are the standard Euler angles that define the rotation using the $z-y-z$ convention in a right-handed frame (Fig. 5.3). To go from an original radiation pattern $\mathbf{F}^{(m)}(\hat{\mathbf{k}})$ in the

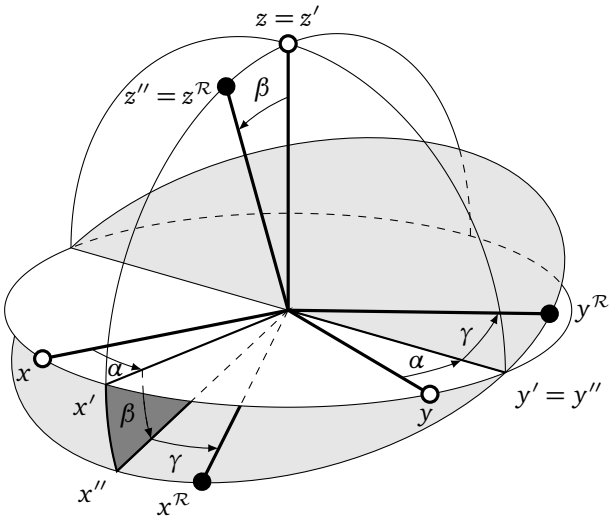

Figure 5.3: Euler angles α, β and γ in the $z-y-z$ convention when rotating from coordinate system (x, y, z) to $(x^{\mathcal{R}}, y^{\mathcal{R}}, z^{\mathcal{R}})$.

coordinate system (x, y, z) to a rotated version $\mathbf{F}^{(m),\mathcal{R}}(\hat{\mathbf{k}})$ in the coordinate system $(x^{\mathcal{R}}, y^{\mathcal{R}}, z^{\mathcal{R}})$, we first rotate by an angle α about the z-axis, then by an angle β about the new y'-axis and finally by an angle γ about the new z''-axis. Starting from a proper reference orientation, any target orientation can be reached. For example, in the case of Fig. 5.3, the Euler angles (α, β, γ) are readily related to the inclination and azimuthal angles θ and ϕ, by choosing $\alpha = \phi$, $\beta = \theta$ and $\gamma = 0$.

To switch between the spatial domain and the spherical harmonics domain, and thus, to obtain the spherical harmonics coefficients A_{pq} and B_{pq} from a radiation pattern $\mathbf{F}^{(m)}(\hat{\mathbf{k}}) = F^{(m)}_\theta(\hat{\mathbf{k}})\hat{\theta} + F^{(m)}_\phi(\hat{\mathbf{k}})\hat{\phi}$ (in a spherical coordinate system) or vice

versa, the transformations $\mathcal{F}$ and its inverse $\mathcal{F}^{-1}$ are used [18]:

$$\mathcal{F} \longleftrightarrow \begin{Bmatrix} A_{pq} \\ B_{pq} \end{Bmatrix} = \frac{-1}{p(p+1)} \int_0^{2\pi} \int_0^{\pi} \Bigg[q \begin{Bmatrix} jF_\phi(\theta,\phi) \\ -F_\theta(\theta,\phi) \end{Bmatrix} Y_{pq}^*(\theta,\phi) + \sin\theta \begin{Bmatrix} -F_\theta(\theta,\phi) \\ jF_\phi(\theta,\phi) \end{Bmatrix} \frac{\mathrm{d}Y_{pq}^*(\theta,\phi)}{\mathrm{d}\theta} \Bigg] \mathrm{d}\theta\,\mathrm{d}\phi, \tag{5.6}$$

$$\mathcal{F}^{-1} \longleftrightarrow \begin{Bmatrix} F_\theta(\theta,\phi) \\ F_\phi(\theta,\phi) \end{Bmatrix} = \sum_{p=0}^{P} \sum_{|q|\le p} \Bigg[\begin{Bmatrix} A_{pq} \\ jB_{pq} \end{Bmatrix} \frac{\mathrm{d}Y_{pq}(\theta,\phi)}{\mathrm{d}\theta} + \begin{Bmatrix} B_{pq} \\ jA_{pq} \end{Bmatrix} \frac{qY_{pq}(\theta,\phi)}{\sin\theta} \Bigg]. \tag{5.7}$$

Here, P is a parameter that determines the accuracy and for practical purposes it can be chosen equal to L [19]. Furthermore, $Y_{pq}(\theta,\phi)$ are the orthonormalized scalar spherical harmonics [20]:

$$Y_{pq}(\theta,\phi) = \sqrt{\frac{(2p+1)}{4\pi}\frac{(p-q)!}{(p+q)!}} P_p^q(\cos\theta) e^{jq\phi}, \tag{5.8}$$

where $P_p^q(\cdot)$ is the associated Legendre polynomial of degree p and order q.

As will be illustrated in Sections 5.3 and 5.4, leveraging (5.6) and (5.7) together with (5.4) allows for the efficient rotation $\mathcal{R}$ of multiport devices without the need for a completely new (expensive) simulation or measurement.

5.2.4 Circuit description

In Figs. 5.4 and 5.5, the equivalent circuit models of a multiport device in transmit mode as well as in receive mode are shown. The gray area represents the device itself, similar as in Fig. 5.1. In this work, the equivalent Thévenin model is used in transmit mode, while the Norton equivalent is chosen in receive mode, but other choices could be made as well. Denote

$$\mathbf{V} = \begin{bmatrix} V_1 \\ \vdots \\ V_N \end{bmatrix} \quad \text{and} \quad \mathbf{I} = \begin{bmatrix} I_1 \\ \vdots \\ I_N \end{bmatrix} \tag{5.9}$$

the vectors of voltages V_n at port P_n and currents I_n flowing into port P_n ($n = 1,\ldots,N$). It is seen from Fig. 5.4 that an N-port device in transmit mode is characterized by an N-port impedance matrix $\mathcal{Z}$:

$$\mathcal{Z} = \begin{bmatrix} Z_{11} & \cdots & Z_{1N} \\ \vdots & \ddots & \vdots \\ Z_{N1} & \cdots & Z_{NN} \end{bmatrix}, \tag{5.10}$$

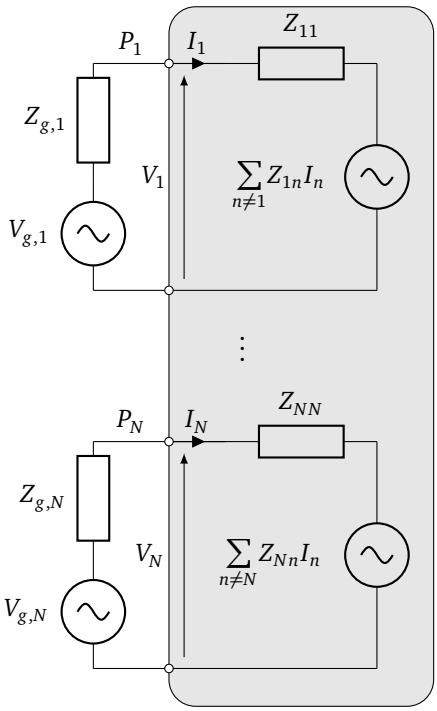

Figure 5.4: Equivalent Thévenin model of an N-port in transmit mode.

where $\mathbf{V}$ and $\mathbf{I}$ are linked through $\mathcal{Z}$ as

$$\mathbf{V} = \mathcal{Z} \cdot \mathbf{I}. \tag{5.11}$$

In receive mode, using the Norton equivalent formulation, the N-port device is characterized by the admittance matrix $\mathcal{Y}$, which is the inverse of the impedance matrix $\mathcal{Z}$, together with an extra term $\mathbf{I_{sc}}$ containing the induced short circuit currents:

$$\mathcal{Y} = \mathcal{Z}^{-1} = \begin{bmatrix} Y_{11} & \cdots & Y_{1N} \\ \vdots & \ddots & \vdots \\ Y_{N1} & \cdots & Y_{NN} \end{bmatrix}, \quad \mathbf{I_{sc}} = \begin{bmatrix} I_{sc}^{(1)} \\ \vdots \\ I_{sc}^{(N)} \end{bmatrix}, \tag{5.12}$$

which are linked through

$$\mathbf{I} = \mathbf{I_{sc}} + \mathcal{Y} \cdot \mathbf{V}. \tag{5.13}$$

The elements of the device's impedance matrix $\mathcal{Z}$ are found by exciting each port successively by a 1 A current source, leaving all other ports open, and measuring the voltage at all ports. In this manner Z_{nm} represents the voltage induced in the open-circuited port P_n, due to a 1 A current excitation at port P_m $(n, m = 1, ..., N)$.

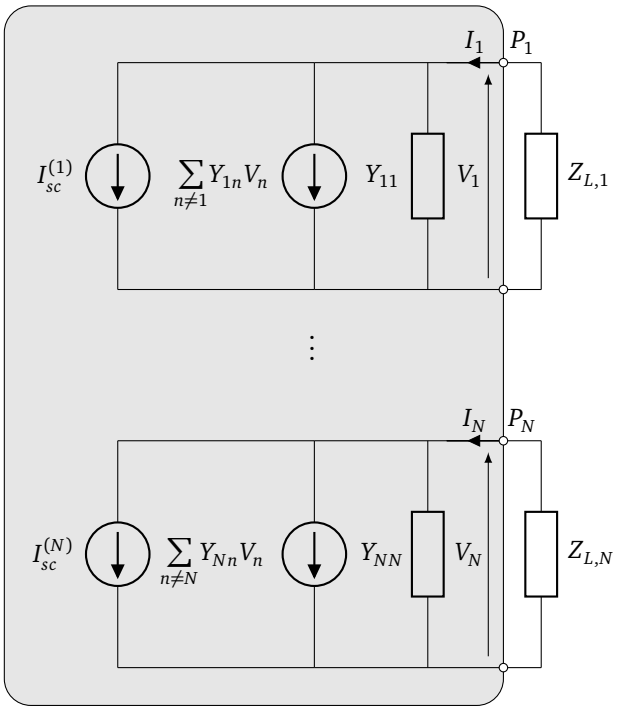

Figure 5.5: Equivalent Norton model of an N-port in receive mode.

A radiation vector $\mathbf{F}^{(n)}(\hat{\mathbf{k}})$ is obtained by exciting port P_n by a 1 V voltage source and short-circuiting the other ports, as shown in Fig. 5.6. This radiation pattern is called the *embedded element pattern* of port P_n of the multiport device, and the coupling with all other ports is correctly taken into account. Note that, when a transmitting N-port is excited simultaneously at several of its N ports, yielding several nonzero embedded radiation patterns $\mathbf{F}^{(n)}(\hat{\mathbf{k}})$, the influence on a receiving M-port, and in particular its induced short-circuit current at port m, is given by (5.3), where the *total* element pattern $\mathbf{F}_{\text{TX}}(\hat{\mathbf{k}})$ has to be used, as further explained in the next section.

5.2.5 Active element pattern

To determine the radiation patterns of a particular port of a multiport device, one has to carefully deal with the terminations at the other ports. Whereas $\mathbf{F}^{(n)}(\hat{\mathbf{k}})$ at port P_n is defined when all other ports are short-circuited, sometimes other formulations are more suitable. For example, to measure radiation patterns over a broad frequency range, accurate 50 Ω terminations are more readily available than short-circuits. It is thus useful to define the so-called *active element pattern*, which represents the radiation pattern $\mathbf{F}^{(n),a}(\hat{\mathbf{k}})$ for excitation of port n with a Thévenin

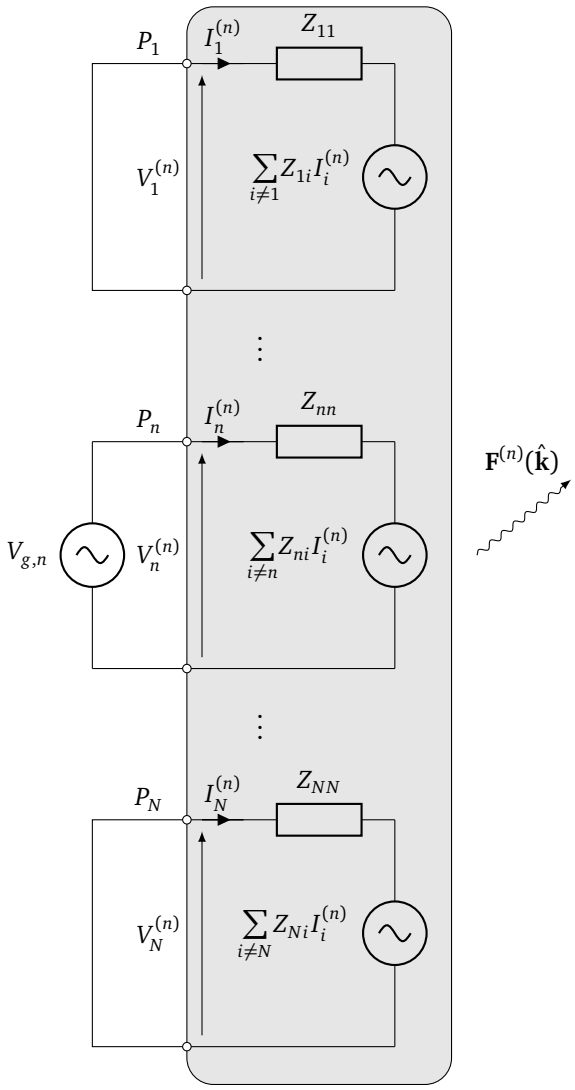

Figure 5.6: Generation of the n-th *embedded* radiation vector $\mathbf{F}^{(n)}(\hat{\mathbf{k}})$ of an N-port ($n = 1,...,N$).

generator, while all other ports are terminated by a nonzero (typically 50 Ω) load, as is seen in Fig. 5.7. If only the active radiation patterns are available, a conversion

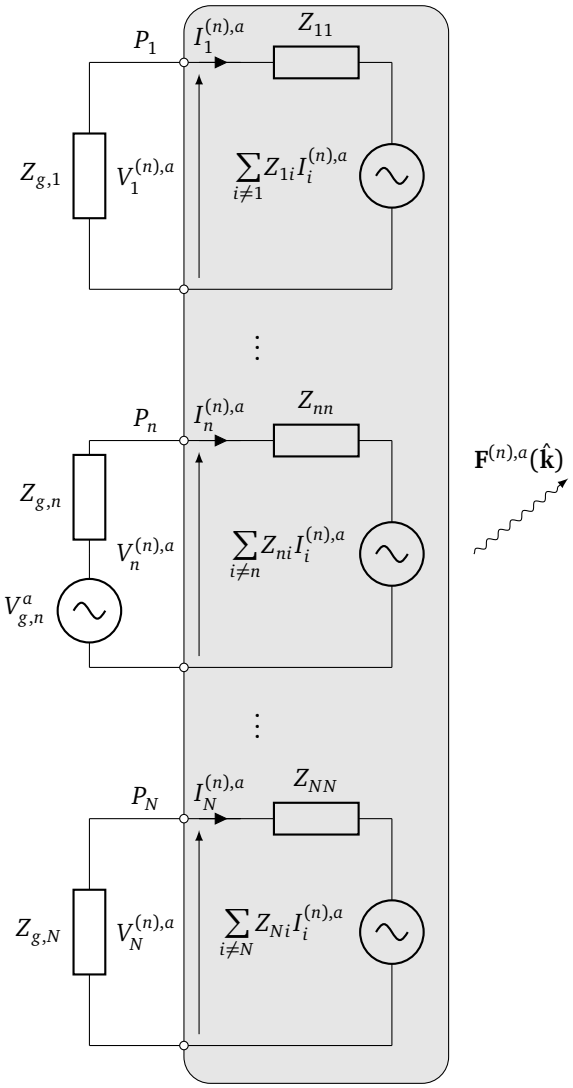

Figure 5.7: Generation of the n-th *active* radiation vector $\mathbf{F}^{(n),a}(\hat{\mathbf{k}})$ of an N-port ($n = 1, ..., N$).

to the embedded patterns is found from Figs. 5.6 and 5.7 by using the superposition principle:

$$\mathbf{F}^{(n),a}(\hat{\mathbf{k}}) = \frac{V_1^{(n),a}}{V_1^{(1)}}\mathbf{F}^{(1)}(\hat{\mathbf{k}}) + ... + \frac{V_N^{(n),a}}{V_N^{(N)}}\mathbf{F}^{(N)}(\hat{\mathbf{k}}), \tag{5.14}$$

where

$$\begin{cases} V_m^{(n),a} = V_{g,n}^a \delta_{nm} - Z_{g,n} I_m^{(n),a} \\ V_n^{(n)} \quad = V_{g,n} \end{cases} \tag{5.15}$$

and with δ_{nm} the Kronecker delta. Substitution of (5.15) into (5.14) yields

$$\mathbf{F}^{(n),a}(\hat{\mathbf{k}}) = \sum_{m=1}^{N} \frac{V_{g,n}^a \delta_{nm} - Z_{g,n}}{V_{g,n}} I_m^{(n),a} \mathbf{F}^{(n)}(\hat{\mathbf{k}}). \tag{5.16}$$

In vector notation, we express the relation between the active radiation patterns $\mathbf{F}^{(\cdot),a}(\hat{\mathbf{k}})$ and the embedded radiation patterns $\mathbf{F}^{(\cdot)}(\hat{\mathbf{k}})$ as

$$\begin{bmatrix} \mathbf{F}^{(1),a}(\hat{\mathbf{k}}) \\ \vdots \\ \mathbf{F}^{(N),a}(\hat{\mathbf{k}}) \end{bmatrix} = \operatorname*{diag}_{i=1}^{N} \left(\frac{1}{V_{g,i}} \right) \left(\operatorname*{diag}_{i=1}^{N} \left(V_{g,i}^a \right) - \operatorname*{diag}_{i=1}^{N} \left(Z_{g,i} \right) \cdot \mathcal{I}^a \right) \begin{bmatrix} \mathbf{F}^{(1)}(\hat{\mathbf{k}}) \\ \vdots \\ \mathbf{F}^{(N)}(\hat{\mathbf{k}}) \end{bmatrix}, \tag{5.17}$$

where diag$(\cdot)$ represents a diagonal matrix. $\mathcal{I}^a$ is the active current matrix given by

$$\mathcal{I}^a = \begin{bmatrix} I_1^{(1),a} & \cdots & I_N^{(1),a} \\ \vdots & \ddots & \vdots \\ I_1^{(N),a} & \cdots & I_N^{(N),a} \end{bmatrix}, \tag{5.18}$$

and governed by Kirchoff's law:

$$\operatorname*{diag}_{i=1}^{N} \left(V_{g,i}^a \right) = \left(\mathcal{Z} + \operatorname*{diag}_{i=1}^{N} \left(Z_{g,i} \right) \right) \cdot \mathcal{I}^a. \tag{5.19}$$

Substitution of (5.19) into (5.17) yields the embedded radiation vectors $\mathbf{F}^{(\cdot)}(\hat{\mathbf{k}})$ as a function of the active radiation vectors $\mathbf{F}^{(\cdot),a}(\hat{\mathbf{k}})$:

$$\begin{bmatrix} \mathbf{F}^{(1)}(\hat{\mathbf{k}}) \\ \vdots \\ \mathbf{F}^{(N)}(\hat{\mathbf{k}}) \end{bmatrix} = \operatorname*{diag}_{i=1}^{N} \left(\frac{V_{g,i}}{V_{g,i}^a} \right) \left[\mathcal{E} - \left(\operatorname*{diag}_{i=1}^{N} \left(\frac{1}{Z_{g,i}} \right) \cdot \mathcal{Z} + \mathcal{E} \right)^{-1} \right]^{-1} \begin{bmatrix} \mathbf{F}^{(1),a}(\hat{\mathbf{k}}) \\ \vdots \\ \mathbf{F}^{(N),a}(\hat{\mathbf{k}}) \end{bmatrix}, \tag{5.20}$$

where $\mathcal{E}$ is the $N \times N$ identity matrix.

The *total* radiation $\mathbf{F}_{\text{TX}}(\hat{\mathbf{k}})$, used in (5.3), emitted by a transmiting device that is excited by multiple Thévenin generators at several or at all of its N ports, is now easily found by adding up the pertinent active radiation patterns.

For completeness, we mention that (the crosstalk between the ports of) a multiport device is often more conveniently described by a scattering matrix, again typically

with respect to $50\,\Omega$ reference impedances. For an N-port network, the scattering matrix is defined by

$$\begin{bmatrix} b_1 \\ \vdots \\ b_N \end{bmatrix} = \begin{bmatrix} S_{11} & \cdots & S_{1N} \\ \vdots & \ddots & \vdots \\ S_{N1} & \cdots & S_{NN} \end{bmatrix} \begin{bmatrix} a_1 \\ \vdots \\ a_N \end{bmatrix} \tag{5.21}$$

or $\mathbf{b} = \mathcal{S} \cdot \mathbf{a}$ in a more compact notation, where a_n and b_n represent the forward and reverse voltage wave amplitudes at the n-th port, respectively. The forward and reverse waves from (5.21) are related to the voltages and currents introduced in (5.9) by $V_n = \sqrt{Z_0}(a_n + b_n)$ and $I_n = (a_n - b_n)/\sqrt{Z_0}$, where Z_0 is the reference impedance of the ports, typically $50\,\Omega$. Nonetheless, the multiport's scattering matrix $\mathcal{S}$ and its impedance matrix $\mathcal{Z}$ (5.11) can be converted into one another as follows [21]:

$$\mathcal{S} = (\mathcal{Z} + Z_0\mathcal{E})^{-1}(\mathcal{Z} - Z_0\mathcal{E}) \tag{5.22}$$

$$\mathcal{Z} = Z_0(\mathcal{E} + \mathcal{S})(\mathcal{E} - \mathcal{S})^{-1}, \tag{5.23}$$

where Z_0 is the reference impedance (e.g. $50\,\Omega$).

5.3 Validation Example

To validate the proposed method, a numerical example is proposed where the transmitter and the receiver are both antenna arrays, each consisting of two half-wavelength dipoles spaced $\lambda/10$ apart (wavelength $\lambda = 1\,\text{m}$). The distance between the antenna arrays is $|\mathbf{r}_{\text{TX,RX}}| = 3\lambda$ and the antennas' wire thickness is chosen to be $10^{-4}\lambda$. The receiving antenna array is rotated over Euler angles $\beta = \frac{2}{3}\alpha = \frac{2}{3}\gamma$, with β varying from 0 to 2π, while the transmitting array remains fixed. In Fig. 5.8, a snapshot of this setup for $\beta = 3\pi/4$ is shown.

The short-circuit currents $I_{sc}^{(1)}$ and $I_{sc}^{(2)}$, calculated with our proposed formalism, are compared to a reference solution. This reference solution is obtained from a Method of Moments (MoM) solver for arbitrary thin wires (see Appendix B and [22]). In the MoM simulation, one half-wavelength dipole is modeled using five segments and the short-circuit currents are calculated by directly inverting the full MoM matrix equation. The dipoles in the transmitting array are excited with $V_{g,1} = V_{g,2} = 1\,\text{V}$ between their terminals, and $Z_{g,1} = Z_{g,2} = 0\,\Omega$.

Contrary to the MoM, our method does not require the computation and inversion of a complete matrix equation for every new relative orientation between transmitting and receiving array. The novel method only requires a single computation of the embedded radiation patterns $\mathbf{F}^{(1)}(\hat{\mathbf{k}})$ and $\mathbf{F}^{(2)}(\hat{\mathbf{k}})$ of the dipole array. Here, we obtained these radiation patterns using a MoM simulation for a single dipole

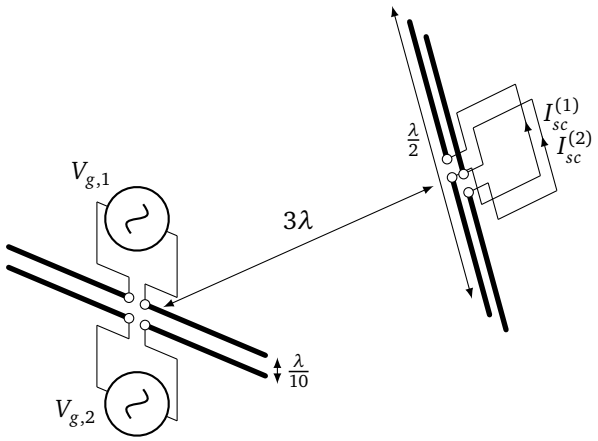

Figure 5.8: Configuration of the validation example where the receiving array (right) is rotated over Euler angles $\beta = \frac{2}{3}\alpha = \frac{2}{3}\gamma$ with $\beta = 3\pi/4$ w.r.t. the transmitting array (left).

array. Once the radiation patterns are available, they are decomposed into spherical harmonics. After this initial setup, simulations can be performed for different relative orientations or positions without a large computational cost as compared to a full MoM simulation.

The results obtained from the MoM simulation and from our novel multiport method are compared in Fig. 5.9 for 361 samples of β to obtain a one-degree resolution. The short-circuit currents $I_{sc}^{(1)}$ and $I_{sc}^{(2)}$ are equal due to the symmetry of the problem geometry. For this example we have used $P = L = 5$ in the calculation of the translation operator and the spherical harmonics. An excellent agreement between the novel method and the MoM simulation is observed. The MoM simulation for all 361 angles took 624 s, whereas the novel method only took 1.3 s of setup time plus 14.9 s of calculation time for all 361 rotated configurations. In total, this corresponds to a speed-up factor of about 38. All simulations have been carried out on an Intel® Core™ i7-2600 processor running at 3.40 GHz and with 16 GB of memory.

5.4 Application Example

In this application example, the two interacting multiport devices in the system are a transmitting Substrate Integrated Waveguide (SIW) three-element antenna array (culprit) and a receiving two-port slotted microstrip line (victim). The three-element antenna array was designed to set up a stable, high data rate ultra-short-range 3×3 multiple-input multiple-output (MIMO) wireless communication link between an access point integrated inside or underneath the worktop of a desk, and a Mobile User (MU) positioned on top of that worktop [23]. Such an approach

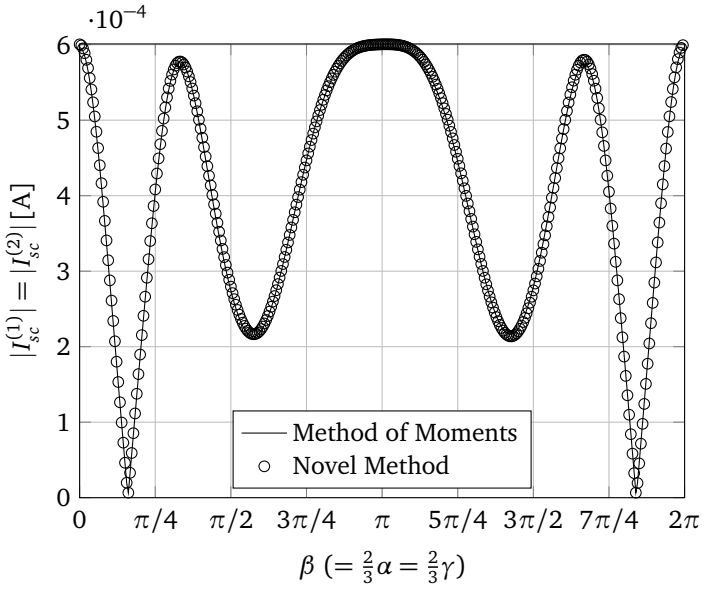

Figure 5.9: Amplitude of the short-circuit currents $I_{sc}^{(1)} = I_{sc}^{(2)}$ at the ports of the receiving dipole, induced by a transmitting dipole array, rotated over Euler angles β $(= \frac{2}{3}\alpha = \frac{2}{3}\gamma)$ (see also Fig. 5.8).

could be adopted in a meeting room, to provide an ultra-high data-rate wireless connection at each seat, replacing wired docking stations. The three-element antenna array consists of three identical ultra-wideband antenna elements, arranged such that the array exhibits threefold rotational symmetry. This specific geometry exploits both spatial and polarization diversity to provide a high multiplexing gain in proximity of the designated working area of the MU.

The microstrip line in the system represents a part of a PCB inside the MU's device (e.g. a laptop) that is put on the table above the three-element antenna. In this manner, a real-life EMI situation, where circuitry inside the laptop is affected by the wireless data link, is considered. Using our novel method, potential EMC problems can now be detected very efficiently during design. The microstrip has dimensions of 17.5 mm $\times$1.6 mm and is placed on a substrate ($\epsilon_r = 3.66$ and $\tan\delta = 0.004$) with 1.6 mm thickness. There is a slot present in the ground plane that has the same dimensions as the microstrip, but it is perpendicular to it. The microstrip is directed toward, and the slot is directed away from the three-element array as shown in Fig. 5.10.

In a real-life scenario, the laptop (and thus the microstrip) may assume several positions w.r.t. the three-element array. This is here reproduced in simulation by rotation of the microstrip about the z-axis or thus by varying α in (5.4) (see also Figs. 5.3 and 5.10). In this example 361 samples for α between 0 to 2π

are chosen, to obtain a one-degree resolution. The interaction between the three-element array and the microstrip for each of these samples is calculated for a frequency of $f = 5\,\text{GHz}$ using the formalism explained in this chapter, and compared with full-wave simulations in Computer Simulation Technology Microwave Studio (CST MWS). The radiation patterns themselves, needed in our approach, are also obtained using CST MWS to make a fair comparison of the simulation times. The simulated radiation patterns are the active radiation patterns and for the receiving device (microstrip), they are converted using (5.20) to obtain the embedded radiation patterns required in (5.3). Further, the impedance matrices $\mathcal{Z}$ of the two multiport devices are obtained via (5.23) after an S-parameter simulation, using again CST MWS. The two multiport devices are placed 100 mm apart, which is less than 2λ, and the number of multipoles is chosen $P = L = 8$.

With our novel method, we can now easily compute the interaction between the two devices. In order to compare it to the results of the CST MWS full-wave simulations, we convert our results (i.e., the short-circuit current) to S-parameters as well, using standard circuit theory techniques [21]. In particular, a 5×5 S-parameter matrix is obtained, describing the interaction between all five ports in the system. In Fig. 5.11, a good agreement for $|S_{14}|$, $|S_{24}|$ and $|S_{34}|$ between our method and the full-wave simulations is shown for all angles α. The port numbering is indicated on Fig. 5.10. Note that the other S-parameters may be derived from these results based on symmetry.

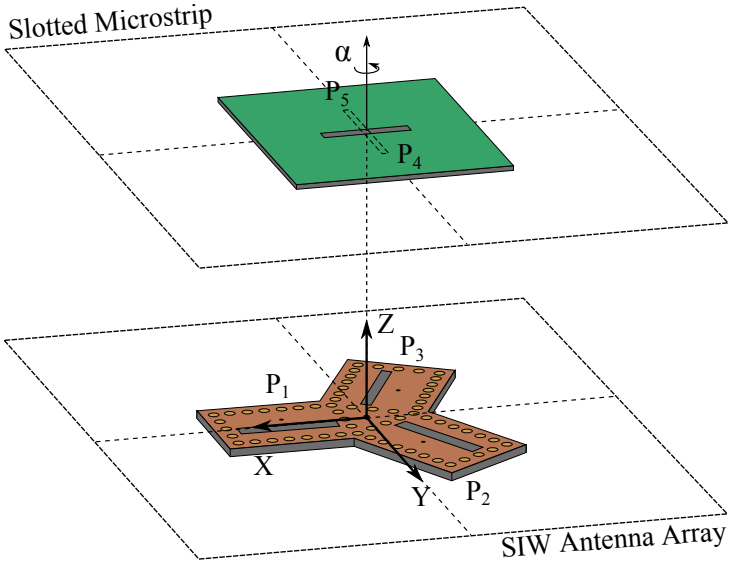

Figure 5.10: Three-element SIW antenna array interacting with a two-port slotted microstrip line for $\alpha = 0$.

The total simulation time in our novel method consists of about 30 min setup time (calculation of the radiation patterns and scattering parameters) and then it takes on average 0.21 s per sample of α. Calculating the scattering matrix for one rotation sample in CST MWS takes about 40 min, implying a speed-up factor compared to the novel method of about 460. This shows the efficiency of our method.

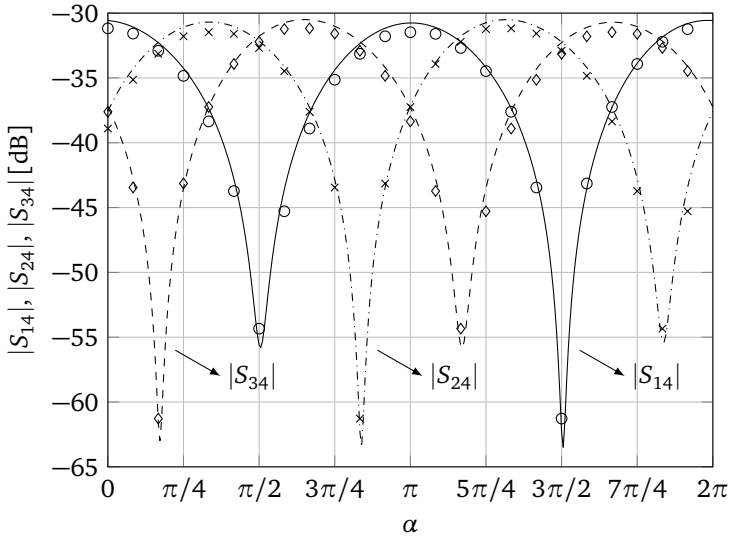

Figure 5.11: Scattering parameters of the link between the three-element array and the two-port microstrip (see Fig. 5.10 for port definitions). Lines: novel method; Markers: CST MWS.

Also a displacement relative to the three-element array can be performed by varying $\mathbf{r}_{\mathrm{TX,RX}}$ in (5.2). Here, first we align the microstrip line with the first antenna element P_1 ($\alpha = \pi/2$) and then the position of the microstrip is varied over the y-axis. This is done for Δy ranging from −100 mm to 100 mm, mimicking a realistic displacement of a user's laptop. The result for 1000 sample points of $|S_{15}|$ is shown in Fig. 5.12. A good agreement between full-wave simulations and our approach is observed. For this simulation, no new setup time was needed and calculating the 5×5 scattering matrix for one sample takes on average 2 ms, which shows that translations can be performed very efficiently.

5.5 Conclusions

In this chapter, a new approach was presented that enables the efficient and accurate modeling of the interaction between multiport devices. The method solely relies on the knowledge of the radiation patterns at each port of the devices to model their EMC behavior when positioned in each other's radiative near-field (Fresnel

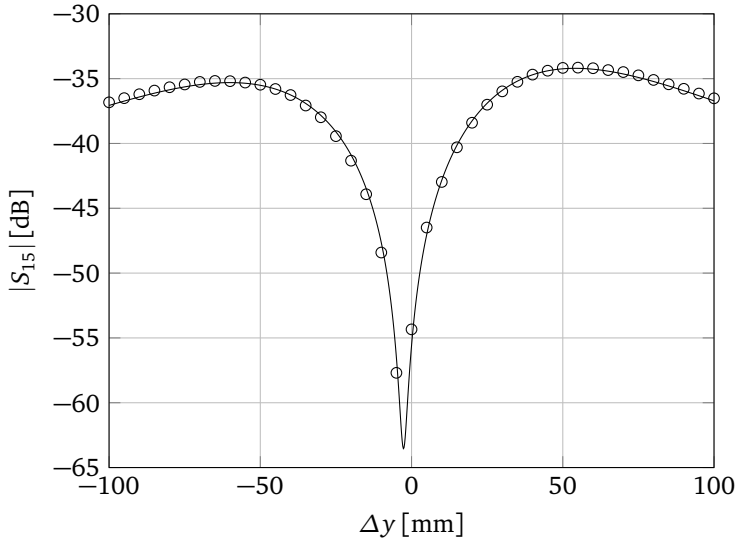

Figure 5.12: $|S_{15}|$ when the microstrip line is translated on the y-axis from -100 mm to 100 mm for $\alpha = \pi/2$ (see Fig. 5.10 for port definitions). Line: novel method; Marker: CST MWS.

region) or far-field (Fraunhofer region). Whereas in conventional simulation tools a repositioning or rotation of the devices would require a completely new (expensive) simulation, the advocated approach allows translating the devices without a large computational cost. Also rotations are performed very efficiently in the spherical harmonics domain. It is important to stress that, in contrast to previous work dealing with singleport devices (i.e., single antennas), the novel method can account for intricate multiport devices. However, thereto, the devices' embedded and active radiation patterns need to be constructed and exploited appropriately, as was detailed in this chapter. The novel method was thoroughly validated by comparison with a full-wave MoM solver, demonstrating its accuracy and efficiency. Moreover, a real-life scenario of an SIW three-element antenna array, being a subsystem of an MIMO transmitting device, disturbing a slotted microstrip line, being a part of a MU's laptop, was examined, as such illustrating the appositeness of the technique for EMI assessment early in the design cycle of new products.

References

[1] P. Li and L. J. Jiang, "Source reconstruction method-based radiated emission characterization for PCBs", *IEEE Transactions on Electromagnetic Compatibility*, vol. 55, no. 5, pp. 933–940, Oct. 2013.

[2] P. Kralicek, W. John, R. De Smedt, K. Vervoort, and H. Garbe, "A voltage controlled emission model of electromagnetic emission of IC for system analysis", in *IEEE International Symposium on Electromagnetic Compatibility*, Montreal, Quebec, 13-17 Aug. 2001, pp. 1197–1202.

[3] I. Erdin, M. Nakhla, and R. Achar, "Circuit analysis of electromagnetic radiation and field coupling effects for networks with embedded full-wave modules", *IEEE Transactions on Electromagnetic Compatibility*, vol. 42, no. 4, pp. 449–460, Nov. 2000.

[4] M. Tang, J. Lu, J. Mao, and L. Jiang, "A systematic electromagnetic-circuit method for EMI analysis of coupled interconnects on dispersive dielectrics", *IEEE Transactions on Microwave Theory and Techniques*, vol. 61, no. 1, pp. 1–13, Jan. 2013.

[5] Y. Bayram and J. Volakis, "Hybrid S-parameters for transmission line networks with linear/nonlinear load terminations subject to arbitrary excitations", *IEEE Transactions on Microwave Theory and Techniques*, vol. 55, no. 5, pp. 941–950, May 2007.

[6] Z. Khan, Y. Bayram, and J. Volakis, "EMI/EMC analysis of printed circuit boards subject to near-zone illuminations", *IEEE Transactions on Electromagnetic Compatibility*, vol. 51, no. 2, pp. 406–408, May 2009.

[7] Y. Shao, Z. Peng, and J.-F. Lee, "Signal integrity analysis of high-speed interconnects by using nonconformal domain decomposition method", *IEEE Transactions on Components, Packaging and Manufacturing Technology*, vol. 2, no. 1, pp. 122–130, Jan. 2012.

[8] Z. Peng, K.-H. Lim, and J.-F. Lee, "Nonconformal domain decomposition methods for solving large multiscale electromagnetic scattering problems", *Proceedings of the IEEE*, vol. 101, no. 2, pp. 298–319, Feb. 2013.

[9] C. Della Giovampaola, E. Martini, A. Toccafondi, and S. Maci, "A hybrid PO/generalized-scattering-matrix approach for estimating the reflector induced mismatch", *IEEE Transactions on Antennas and Propagation*, vol. 60, no. 9, pp. 4316–4325, Sep. 2012.

[10] T. Flisgen, H. Glock, and U. Van Rienen, "Compact time-domain models of complex RF structures based on the real eigenmodes of segments", *IEEE Transactions on Microwave Theory and Techniques*, vol. 61, no. 6, pp. 2282–2294, Jun. 2013.

[11] H. Wu and A. Cangellaris, "A finite-element domain-decomposition methodology for electromagnetic modeling of multilayer high-speed interconnects", *IEEE Transactions on Advanced Packaging*, vol. 31, no. 2, pp. 339–350, May 2008.

[12] G.-J. Stockman, H. Rogier, and D. Vande Ginste, "Efficient modeling of interactions between radiating devices with arbitrary relative positions and orientations", *IEEE Transactions on Electromagnetic Compatibility*, vol. 56, no. 6, pp. 1313–1321, Dec. 2014.

[13] ——, "Efficient full-wave modeling of radiative near-field interactions in semi-anechoic conditions", in *IEEE International Symposium on Electromagnetic Compatibility (EMC), 2015*, Aug. 2015, pp. 524–528.

[14] ——, "Efficient full-wave modeling of electromagnetic interference in the presence of multiple non-collocated noise sources", in *International Conference on Electromagnetics in Advanced Applications (ICEAA), 2015*, Sep. 2015, pp. 175–178.

[15] W. C. Chew, J.-M. Jin, E. Michielssen, and J. Song, *Fast and efficient algorithms in computational electromagnetics*. Artech House Publishers, 2001.

[16] R. Hoover, A. Maciejewski, and R. Roberts, "Pose detection of 3-D objects using images sampled on SO(3), spherical harmonics, and Wigner-D matrices", in *IEEE International Conference on Automation Science and Engineering, CASE.*, Arlington, Virginia, 23-26 Aug. 2008, pp. 47–52.

[17] Z. Gimbutas and L. Greengard, "A fast and stable method for rotating spherical harmonic expansions", *Journal of Computational Physics*, vol. 228, pp. 5621–5627, May 2009.

[18] J. Rahola, F. Belloni, and A. Richter, "Modelling of radiation patterns using scalar spherical harmonics with vector coefficients", in *3rd European Conference on Antennas and Propagation, EuCAP*, Berlin, Germany, 23-27 Mar. 2009, pp. 3361–3365.

[19] T. F. Eibert, "A diagonalized multilevel fast multipole method with spherical harmonics expansion of the k-space integrals", *IEEE Transactions on Antennas and Propagation*, vol. 53, no. 2, pp. 814–817, Feb. 2005.

[20] *NIST digital library of mathematical functions*, http://dlmf.nist.gov/, Release 1.0.5 of 2012-10-01.

[21] D. Pozar, *Microwave Engineering*. Wiley, 2004.

[22] W. C. Gibson, *The Method of Moments in Electromagnetics*. Chapman & Hall/CRC, 2008, ch. 4, pp. 73–79.

[23] S. Lemey, T. Castel, P. V. Torre, T. Vervust, J. Vanfleteren, P. Demeester, D. Vande Ginste, and H. Rogier, "Threefold rotationally symmetric siw antenna array for ultra-short-range mimo communication", *IEEE Transactions on Antennas and Propagation*, Early Access, DOI 10.1109/TAP.2016.2536163.

Part II

Efficiency Modeling of Wireless Power Transfer Systems

When designing Wireless Power Transfer (WPT) systems, the efficient modeling of the link efficiency up until the radiative near-field is of great importance. This helps the designer to estimate the overall performance of a WPT system and assists in making early design choises. In Chapters 6 and 7, the novel method described in Part I is combined with circuit and antenna theory to assess the complete link efficiency of WPT systems, i.e. the conversion efficiency from transmitted Alternating Current (AC) power to received Direct Current (DC) power.

6

Dedicated Model for the Efficient Assessment of Wireless Power Transfer in the Radiative Near-Field

Based on "Dedicated model for the efficient assessment of wireless power transfer in the radiative near-field," Gert-Jan Stockman, Hendrik Rogier and Dries Vande Ginste, *International Journal of Numerical Modelling: Electronic Networks, Devices and Fields*, 2016.

★ ★ ★

In this chapter, a novel method to efficiently calculate the power transfer efficiency of a wireless power transfer system in the radiative near-field is proposed. The technique allows repositioning of the antennas without large additional cost. It relies on a single simulation (or measurement) of the radiation pattern of the antennas used. Thanks to its high computational efficiency, it can be used in multi-transmitter and multi-receiver scenarios when there is no coupling between devices via the reactive near-field. Our method is applied to the latter to demonstrate its accuracy and computational efficiency.

6.1 Introduction

Due to its use in Radio Frequency Identification (RFID) systems, near-field Wireless Power Transfer (WPT) is a research topic that has gained more and more interest

over the past years. The research done on WPT can be divided into three different groups, based on the distance between the antennas employed in the system. First, in the reactive near-field, an often used method to determine the Power Transfer Efficiency (PTE) of a WPT system is by making use of coupled mode theory. In the region of coupled mode resonance, the coupling between the antennas is strong and a very high PTE can be obtained ($> 80\%$) [1], [2]. However, the coupling distance needs to be very small and furthermore, an optimal design in this region is very hard since the optimal resonant frequency and the load impedance are strongly dependent on the distance between the antennas. Coupled mode resonance has been widely investigated over the years [3], as well as lateral and angular coil misalignment [4] and multiple-receiver scenarios [5], [6].

Second, in the radiative near-field (Fresnel region), beyond the coupled mode resonance region, the PTE decreases rapidly with distance. Nonetheless, for low-power applications such as sensor networks, a sufficiently high PTE can still be obtained. The coupling in this region is much weaker and can be modeled using a spherical mode expansion. This expansion allows the assessment of angular misalignment between the different devices of the WPT system [7]. It is also shown that in order to achieve a PTE close to the theoretical upper bound, electrically small antennas with high radiation efficiency are needed [7], [8]. The theoretical upper bound has been extended to multiple transmitters in [1].

Third, in the far-field (Fraunhofer region) the PTE can be modeled using the traditional Friis formula [9]. To alleviate orientation dependence of these systems, antennas are designed to be circularly polarized in order to maximize the polarization efficiency component of the link budget. The question remains if this approach is still suitable when the antennas are brought into the near-field region [3].

To gain better insight in the PTE of WPT systems in the radiative near-field region, several methods developed to mimic the electromagnetic problem with reduced computational complexity are leveraged. Emission modeling is realized using the source reconstruction method or by expanding the electromagnetic field in multipoles [10], [11]. Susceptibility modeling focuses more on hybrid techniques such as model reduction combined with full-wave solvers [12]. Finally, Domain Decomposition Methods (DDMs) reduce the computational resources by dividing the electromagnetic problem into different domains. Each of these domains is solved seperately using an efficient technique specific to the domain after which the different solutions are combined [13], [14]. Another method to model the interaction between radiating devices with a low computational complexity is presented in this chapter. It is shown that the electromagnetic interaction for arbitrarily positioned devices can be computed using a single simulation (or measurement) of the individual radiation patterns of the devices. This information is sufficient to model any configuration without requiring new simulations every time a device is repositioned. In contrast to [7], these devices are not necessarily electrically small. By taking into account higher-order multipole interactions, any type of antenna may be used (via its radiation pattern). As such, for all possible configurations, our

method allows the efficient modeling of the PTE in a realistic WPT system in the radiative near-field (and beyond) with high accuracy.

The structure of this chapter is as follows. In Section 6.2, the formalism of our method is explained. The electromagnetic interaction between a transmitting and receiving device in a WPT setup is described in order to obtain an expression for the wireless link efficiency. Thereto, we also briefly discuss what makes up the rectenna efficiency. Section 6.3 applies and validates this theory by means of a practical WPT example in the radiative near-field, illustrating how to combine all the different power efficiencies to come to a PTE of the complete WPT system. Moreover, the efficiency of the advocated method is demonstrated. Finally, Section 6.4 concludes this chapter.

In the sequel, all sources and fields are assumed to be time harmonic with angular frequency ω and with time dependencies $e^{j\omega t}$ suppressed. Unit vectors are denoted with a "hat", e.g. $\hat{\mathbf{v}}$.

6.2 Formalism

To obtain the wireless link efficiency between two devices, arbitrarily positioned in space, we first model the electromagnetic interaction between them. We start from the very general problem geometry shown in Fig. 6.1, consisting of a transmitting and receiving device, represented by current density sources $\mathbf{j}_{\text{TX}}$ and $\mathbf{j}_{\text{RX}}$ contained in volumes V_{TX} and V_{RX}, respectively. To each device's phase center, $\mathcal{O}_{\text{TX}}$ and $\mathcal{O}_{\text{RX}}$, a local coordinate system is attached (($x_{\text{TX}}, y_{\text{TX}}, z_{\text{TX}}$) and ($x_{\text{RX}}, y_{\text{RX}}, z_{\text{RX}}$)). The electric field $\mathbf{e}(\mathbf{r})$ generated by the sources is given by the Electric Field Integral Equation

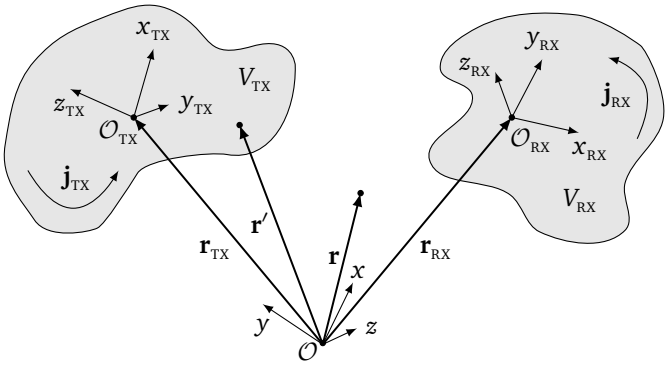

Figure 6.1: Two devices with arbitrary phase centers $\mathcal{O}_{\text{TX}}$ and $\mathcal{O}_{\text{RX}}$.

(EFIE) [15]:

$$\mathbf{e}(\mathbf{r}) = -j\omega\mu \int_V \mathcal{G}(\mathbf{r},\mathbf{r}') \cdot \mathbf{j}(\mathbf{r}')\,\mathrm{d}\mathbf{r}', \tag{6.1}$$

where $\mathbf{j}(\mathbf{r}')$ represents both current densities $\mathbf{j}_{\mathrm{TX}}(\mathbf{r}')$ and $\mathbf{j}_{\mathrm{RX}}(\mathbf{r}')$. μ is the permeability of the background medium, and $\mathcal{G}(\mathbf{r},\mathbf{r}')$ the three-dimensional dyadic Green's function given by

$$\mathcal{G}(\mathbf{r},\mathbf{r}') = \Big[\mathcal{I} + \frac{1}{k^2}\nabla\nabla\Big]\frac{e^{-jk|\mathbf{r}-\mathbf{r}'|}}{4\pi|\mathbf{r}-\mathbf{r}'|}. \tag{6.2}$$

Here, $k = \omega\sqrt{\epsilon\mu}$ is the wavenumber of the background medium and ϵ its permittivity. The integration domain V extends over both devices (denoted as transmitter TX and receiver RX), i.e. $V = V_{\mathrm{TX}} \cup V_{\mathrm{RX}}$, allowing the decomposition of the EFIE into two components:

$$\mathbf{e}(\mathbf{r}) = -j\omega\mu \int_{V_{\mathrm{TX}}} \mathcal{G}(\mathbf{r},\mathbf{r}') \cdot \mathbf{j}_{\mathrm{TX}}(\mathbf{r}')\,\mathrm{d}\mathbf{r}' - j\omega\mu \int_{V_{\mathrm{RX}}} \mathcal{G}(\mathbf{r},\mathbf{r}') \cdot \mathbf{j}_{\mathrm{RX}}(\mathbf{r}')\,\mathrm{d}\mathbf{r}'. \tag{6.3}$$

For devices positioned in each other's Fresnel or Fraunhofer region, the field incident on the receiving device can be accurately approximated by the first term in (6.3), taking $\mathbf{j}_{\mathrm{TX}}(\mathbf{r}')$ as the stand-alone current density of the single element. We assume that these devices are spaced sufficiently far from each other, so there is no coupling via the reactive near-field.

We proceed by considering the scalar 3-D Green's function and by using Gegenbauer's addition theorem [16], [17]:

$$\frac{e^{-jk|\mathbf{D}+\mathbf{d}|}}{|\mathbf{D}+\mathbf{d}|} = -jk\sum_{l=0}^{\infty}(-1)^l(2l+1)j_l(k|\mathbf{d}|)h_l^{(2)}(k|\mathbf{D}|)P_l(\hat{\mathbf{d}}\cdot\hat{\mathbf{D}}). \tag{6.4}$$

Here, $j_l(\cdot)$ is the l-th order spherical Bessel function of the first kind, $h_l^{(2)}(\cdot)$ the l-th order spherical Hankel function of the second kind and $P_l(\cdot)$ the Legendre polynomial of degree l. The product $j_l(k|\mathbf{d}|)P_l(\hat{\mathbf{d}}\cdot\hat{\mathbf{D}})$ can be expanded into plane waves as [18]

$$4\pi(-j^l)j_l(k|\mathbf{d}|)P_l(\hat{\mathbf{d}}\cdot\hat{\mathbf{D}}) = \iint_{\Omega} e^{-j\mathbf{k}\cdot\mathbf{d}}P_l(\hat{\mathbf{k}}\cdot\hat{\mathbf{D}})\,\mathrm{d}\hat{\mathbf{k}}, \tag{6.5}$$

where we integrate over the Ewald sphere Ω and $\mathbf{k}$ is the wave vector in spherical coordinates:

$$\mathbf{k} = k\hat{\mathbf{k}} = k(\sin\theta\cos\phi\,\hat{\mathbf{x}} + \sin\theta\sin\phi\,\hat{\mathbf{y}} + \cos\theta\,\hat{\mathbf{z}}). \tag{6.6}$$

In the configuration under study (Fig. 6.1), $\mathbf{r}_{\mathrm{TX}}$ and $\mathbf{r}_{\mathrm{RX}}$ refer to the positions of the phase centers $\mathcal{O}_{\mathrm{TX}}$ and $\mathcal{O}_{\mathrm{RX}}$ of the transmitter and receiver, respectively, with respect to the common origin $\mathcal{O}$. Introducing $\mathbf{D} = \mathbf{r}_{\mathrm{TX,RX}} = \mathbf{r}_{\mathrm{RX}} - \mathbf{r}_{\mathrm{TX}}$, $\mathbf{d} = (\mathbf{r} - \mathbf{r}_{\mathrm{RX}}) - (\mathbf{r}' - \mathbf{r}_{\mathrm{TX}})$ and thus $(\mathbf{D} + \mathbf{d}) = (\mathbf{r} - \mathbf{r}')$ into (6.4) and (6.5) yields an expression for the kernel of the EFIE (6.1):

$$\frac{e^{-jk|\mathbf{r}-\mathbf{r}'|}}{|\mathbf{r}-\mathbf{r}'|} = \frac{-jk}{4\pi} \iint\limits_{\Omega} e^{-j\mathbf{k}\cdot(\mathbf{r}-\mathbf{r}_{\mathrm{RX}})} T(\mathbf{r}_{\mathrm{TX,RX}}, \hat{\mathbf{k}}) e^{+j\mathbf{k}\cdot(\mathbf{r}'-\mathbf{r}_{\mathrm{TX}})} \, \mathrm{d}\hat{\mathbf{k}}. \tag{6.7}$$

The operator $T(\mathbf{r}_{\mathrm{TX,RX}}, \hat{\mathbf{k}})$ is calculated as

$$T(\mathbf{r}_{\mathrm{TX,RX}}, \hat{\mathbf{k}}) \approx \sum_{l=0}^{L} (2l+1) j^{-l} h_l^{(2)}(k|\mathbf{r}_{\mathrm{TX,RX}}|) P_l(\hat{\mathbf{k}} \cdot \hat{\mathbf{r}}_{\mathrm{TX,RX}}). \tag{6.8}$$

The interchange of summation and integration, which was performed to obtain (6.7), is only allowed if the infinite sum is truncated to a finite number of terms L. Traditional guidelines to select this number, which determines the accuracy, are found in [16]. Note that, for (6.7) to be valid, $|\mathbf{d}| < |\mathbf{D}|$ or equivalently $|(\mathbf{r} - \mathbf{r}_{\mathrm{RX}}) - (\mathbf{r}' - \mathbf{r}_{\mathrm{TX}})| < |\mathbf{r}_{\mathrm{TX,RX}}|$ must hold. By taking into account these higher-order multipole interactions, the traditional far-field approximation can be extended into the radiative near-field with high accuracy. Using the EFIE (6.1) and the kernel (6.7), we obtain an approximate expression for the electric field incident on the receiver, caused by the transmitter:

$$\mathbf{e}^{\mathbf{inc}}(\mathbf{r}) \approx -\frac{\omega k}{4\pi} \iint\limits_{\Omega} e^{-j\mathbf{k}\cdot(\mathbf{r}-\mathbf{r}_{\mathrm{RX}})} T(\mathbf{r}_{\mathrm{TX,RX}}, \hat{\mathbf{k}}) \left[\mathcal{I} - \hat{\mathbf{k}}\hat{\mathbf{k}}\right] \cdot \mathbf{N}_{\mathrm{TX}}(\hat{\mathbf{k}}) \, \mathrm{d}\hat{\mathbf{k}}, \tag{6.9}$$

where $\mathbf{N}_{\mathrm{TX}}(\hat{\mathbf{k}})$ is given by

$$\mathbf{N}_{\mathrm{TX}}(\hat{\mathbf{k}}) = \frac{\mu}{4\pi} \int\limits_{V_{\mathrm{TX}}} e^{j\mathbf{k}\cdot(\mathbf{r}'-\mathbf{r}_{\mathrm{TX}})} \mathbf{j}(\mathbf{r}') \, \mathrm{d}\mathbf{r}'. \tag{6.10}$$

We define the radiation pattern $\mathbf{F}_{\mathrm{TX}}(\hat{\mathbf{k}})$ of the transmitting device as

$$\begin{aligned} \mathbf{F}_{\mathrm{TX}}(\hat{\mathbf{k}}) &= F_{\mathrm{TX},\theta}(\hat{\mathbf{k}})\hat{\theta} + F_{\mathrm{TX},\phi}(\hat{\mathbf{k}})\hat{\phi} \\ &= j\omega\hat{\mathbf{k}} \times [\hat{\mathbf{k}} \times \mathbf{N}_{\mathrm{TX}}(\hat{\mathbf{k}})], \end{aligned} \tag{6.11}$$

and hence,

$$\begin{aligned} \left[\mathcal{I} - \hat{\mathbf{k}}\hat{\mathbf{k}}\right] \cdot \mathbf{N}_{\mathrm{TX}}(\hat{\mathbf{k}}) &= \mathbf{N}_{\mathrm{TX}}(\hat{\mathbf{k}}) - \hat{\mathbf{k}}[\hat{\mathbf{k}} \cdot \mathbf{N}_{\mathrm{TX}}(\hat{\mathbf{k}})] \\ &= -\hat{\mathbf{k}} \times [\hat{\mathbf{k}} \times \mathbf{N}_{\mathrm{TX}}(\hat{\mathbf{k}})] \\ &= -\frac{1}{j\omega} \mathbf{F}_{\mathrm{TX}}(\hat{\mathbf{k}}). \end{aligned} \tag{6.12}$$

Consequently, the incident electric field (6.9) can be written in terms of $\mathbf{F}_{\mathrm{TX}}(\hat{\mathbf{k}})$.

Assume now, for simplicity, that the transmitter and receiver in our WPT configuration are one-port devices such as single antenna elements. Then, an equivalent circuit representation [15] of a WPT system is shown in Fig. 6.2. Here, Z_{TX} and Z_{RX} are the radiation impedances of the transmit and receive antenna respectively.

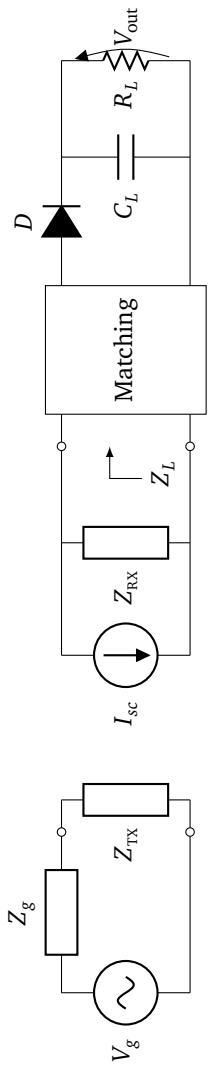

Figure 6.2: Equivalent circuit of a WPT link, i.e. a transmit antenna and a receive antenna with rectifier (rectenna).

The transmitter is driven by means of a Thévenin generator composed of a sinusoidal voltage source V_g with internal impedance Z_g. The Norton equivalent of the receiver consists of a load impedance Z_L and a short-circuit current I_{sc}, computed as

$$I_{sc} = -\frac{1}{V_0} \int_{V_{\text{RX}}} \mathbf{e}^{\text{inc}}(\mathbf{r}) \cdot \mathbf{j}(\mathbf{r}) \, \mathrm{d}\mathbf{r}, \tag{6.13}$$

where V_0 is the pertinent normalization factor, evolving from the reciprocity theorem, depending on the normalized radiation pattern when operating the antenna in transmit mode (see [19] for a detailed explanation). As the antennas' radiation patterns scale linearly with V_0, this parameter can be chosen to be 1 V. Defining the radiation pattern $\mathbf{F}_{\text{RX}}(\hat{\mathbf{k}})$ of the receiver in a similar way as (6.11) and substituting (6.9) and (6.12) into (6.13), yields the following expression for the short-circuit current:

$$I_{sc} \approx -\frac{1}{ZV_0} \iint_{\Omega} T(\mathbf{r}_{\text{TX,RX}}, \hat{\mathbf{k}}) \mathbf{F}_{\text{TX}}(\hat{\mathbf{k}}) \cdot \mathbf{F}_{\text{RX}}(-\hat{\mathbf{k}}) \, \mathrm{d}\hat{\mathbf{k}}, \tag{6.14}$$

where $Z = \sqrt{\frac{\mu}{\epsilon}}$ is the wave impedance of the background medium.

The above result allows us to calculate the short-circuit current of a receiving antenna by using only the single element radiation patterns $\mathbf{F}_{\text{TX}}(\hat{\mathbf{k}})$ and $\mathbf{F}_{\text{RX}}(\hat{\mathbf{k}})$ of transmit and receive antenna respectively. The operator $T(\mathbf{r}_{\text{TX,RX}}, \hat{\mathbf{k}})$ allows efficient translations between the two antennas. When devices are repositioned in space, only the original radiation patterns are needed. The interaction between devices is efficiently calculated for any set of positions of the devices, whereas for traditional simulation tools or measurements, a new computation or measurement is needed for every repositioning [20]. Our method also allows the use of electrically large antennas by taking into account higher-order multipole interactions.

Using the expression for the short-circuit current (6.14), the power delivered to the receiving antenna's load Z_L is written as

$$P_{\text{RX}} = \frac{1}{2} \Re \left(Z_L \left| I_{sc} \right|^2 \left| \frac{Z_{\text{RX}}}{Z_{\text{RX}} + Z_L} \right|^2 \right). \tag{6.15}$$

Knowing that the power emitted by the transmitter with radiation pattern $\mathbf{F}_{\text{TX}}(\hat{\mathbf{k}})$ is calculated as

$$P_{\text{TX}} = \frac{1}{2Z} \iint_{\Omega} \left| \mathbf{F}_{\text{TX}}(\hat{\mathbf{k}}) \right|^2 \mathrm{d}\hat{\mathbf{k}}, \tag{6.16}$$

the power efficiency η_{link} of the wireless link between transmitter and receiver is described by

$$\eta_{\text{link}} = \frac{P_{\text{RX}}}{P_{\text{TX}}} = \frac{\frac{1}{2}\Re\left(Z_L \left|I_{sc}\right|^2 \left|\frac{Z_{\text{RX}}}{Z_{\text{RX}}+Z_L}\right|^2\right)}{\frac{1}{2Z}\iint\limits_{\Omega} |\mathbf{F}_{\text{TX}}(\hat{\mathbf{k}})|^2 \, \mathrm{d}\hat{\mathbf{k}}}, \tag{6.17}$$

In the context of WPT, an interesting conclusion is now readily derived from (6.14) and (6.17): to calculate the wireless link efficiency η_{link} between a transmitting device and a receiving device, it is sufficient to have access to either their measured or simulated radiation patterns. This is true for any relative position between the two devices, indicated by $\mathbf{r}_{\text{TX,RX}}$, as long as there is no coupling via the reactive near-field, hence $|\mathbf{r}_{\text{TX,RX}}|$ should be larger than, say, at least a sixth of the wavelength.

The PTE of a WPT system such as the one schematically shown in Fig. 6.2, is defined as the ratio of Direct Current (DC) power dissipated in the load R_L at the receiving side to the Alternating Current (AC) power delivered to the transmit antenna. Assuming no radiation losses, this AC power equals P_{TX} given by (6.16). The DC power delivered to the load is found by combining the link efficiency calculated in (6.17) with the efficiency of the rectenna. Here it is important to note that the latter is not only made up by the efficiency of the rectifier but also by the efficiency of a potential matching circuit between the antenna and the rectifier. Since the input impedance Z_L of nonlinear circuits depends on the incoming power, this matching efficiency η_{match} will also be a function of the incoming power. The matching efficiency can, for a known rectifier circuit, be simulated using commercial tools such as Advanced Design System (ADS). The efficiency of the rectifier circuit itself can be calculated by comparing the DC power, delivered to the load resistor R_L, to the incoming power $P_{\text{inc}} = \eta_{\text{match}} \cdot P_{\text{RX}}$, injected into the rectifier circuit. The DC power P_{DC} delivered to the load R_L is calculated as

$$P_{\text{DC}} = \frac{V_{\text{out}}^2}{R_L}. \tag{6.18}$$

The DC output voltage V_{out} may be found from simulation tools such as ADS or from an analytical expression describing the behavior of diode detectors [21]. By clever alteration of the parameters of such expressions, also voltage doublers can be taken into account [22].

6.3 Application to a Wireless Power Transfer System

6.3.1 Description of the Wireless Power Transfer system

To demonstrate the efficiency and appositeness of the formalism, an application example is considered consisting of a multi-receiver scenario. In this example, a

large Standard Gain Horn (SGH) antenna is applied as transmitter, transferring power to an array of patch antennas. These receiving antennas are embedded into a wall in order to supply power to a sensor network (Fig. 6.3). Each patch

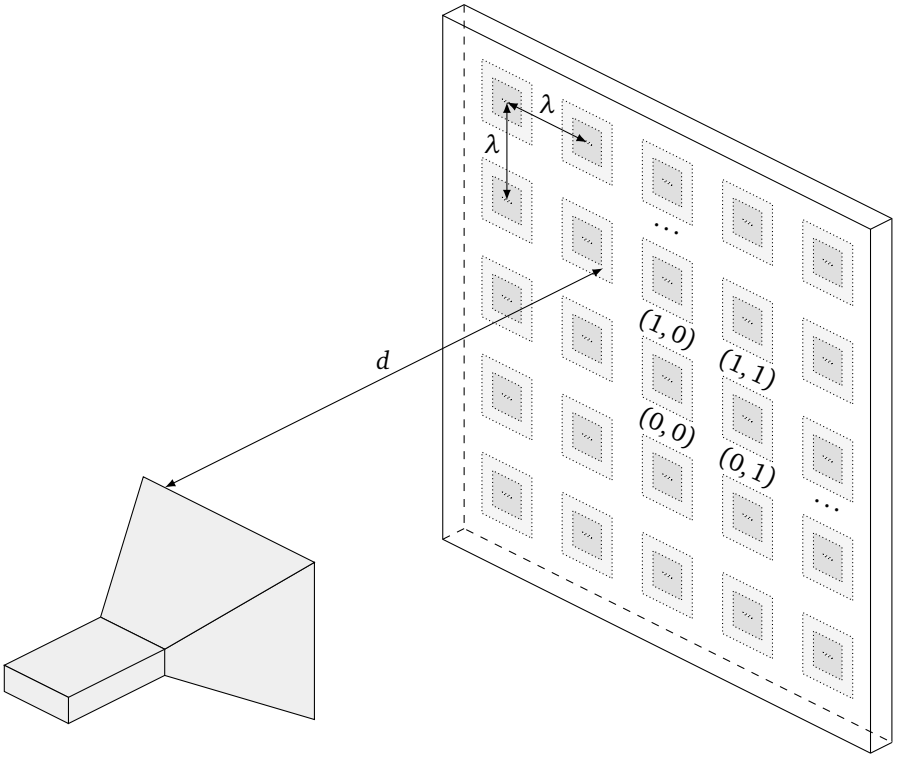

Figure 6.3: An antenna aray embedded into a brick wall used to wirelessly power a sensor network. The antenna elements are dual polarized textile patch antennas, spaced at least one wavelength λ from each other. The transmitting antenna is an SGH transmitting at $f = 2.45\,\text{GHz}$. It is separated from the brick wall by a distance d.

antenna is a dual polarized textile antenna for operation in the Industrial, Scientific and Medical (ISM) band at frequency $f = 2.45\,\text{GHz}$ [23]. The antennas in the array are spaced sufficiently apart such that their mutual coupling is negligible (the separation distance between phase centers is minimally one wavelength λ). The patch antennas are located inside a brick wall as shown in Fig. 6.4. There is 1 cm of spacer in front of the antenna followed by 4 cm of brick wall ($\epsilon_r = 3.7$ and $\mu_r = 1$ [24]). The radiation pattern of a single antenna element embedded into the brick wall is calculated using ADS-Momentum. Using an analytical expression for the radiation pattern of the horn antenna (see the appendix of [20], where here we chose $a = 369\,\text{mm}$, $b = 273\,\text{mm}$, $\rho_1 = 344\,\text{mm}$ and $\rho_2 = 363\,\text{mm}$ for our SGH-1.7). The SGH's phase center is aligned to the phase center of the center antenna element of the array (= antenna element $(0, 0)$). The negligible coupling

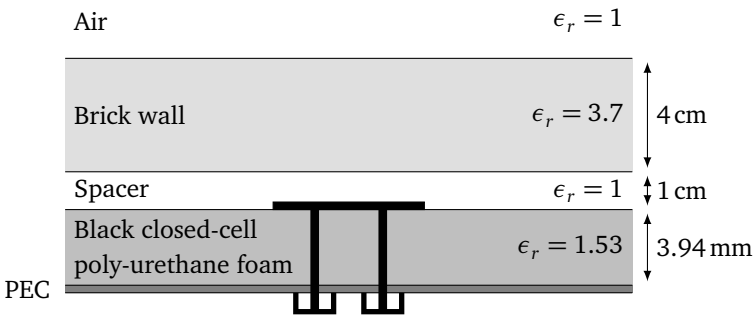

Figure 6.4: Cross-section of the dual polarized textile antenna embedded inside a brick wall with a PEC ground plane (not on scale). More information on the antenna is found in [23].

between antenna elements is confirmed by a full-wave simulation, as the mutual coupling between any two elements in the array is always less than −25 dB (with the brick wall and possible surface wave coupling taken into account).

6.3.2 Validation example

In order to validate the proposed formalism, we first consider an example where the horn antenna is used as transmitter and a dual polarized patch antenna as receiver. The results of measurements and simulations of the transmission coefficient S_{21} will be compared. The transmission coefficient is relevant in this discussion since it is directly related to the efficiency of the wireless link as $\eta_{\text{link}} = |S_{21}|^2$. The brick wall is omitted for ease of measurement, but this does not detract from the generality of the method. The measurement has been performed in an anechoic chamber and a Vector Network Analyzer (VNA), i.e. the PNA-X N5242A of Agilent Technologies, is hereby used. The distance between the transmit and receive antenna d is varied up to 2λ, to cover the radiative near-field. The obtained results are shown in Fig. 6.5, where also a comparison with the Friis formula is presented. Simulations (with $L = 15$) using the advocated formalism and measurements yield an absolute error of only 1 dB, which can be attributed to the lossless horn antenna used in the simulations and to horn, connector and cable loss in the measurements. It is clear that, in the reactive near-field, the traditional Friis formula produces a huge overestimation and that it is only usable in the far-field, where it indeed converges to our novel formalism.

6.3.3 Calculation of the PTE

To calculate the PTE for the multi-receiver scenario in Fig. 6.3, we first compute the power efficiency of the link η_{link} using the formalism explained in Section 6.2. The novel method easily allows a repositioning of the used antennas which, e.g., allows a sweep of the wireless link efficiency over different separation distances d

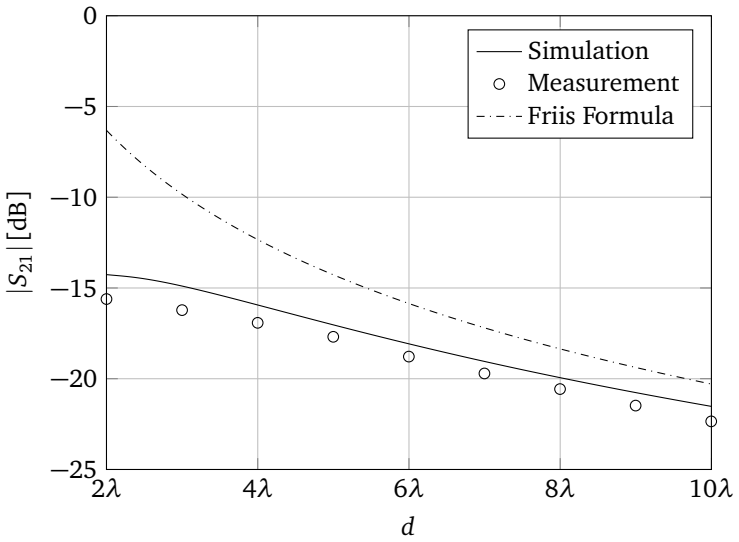

Figure 6.5: Comparison of simulation, measurement and Friis formula of S_{21} in a single-receiver scenario.

between horn and the antennas in the wall. The resulting efficiency in function of the separation distance is shown in Fig. 6.6. Element $(0,0)$ is the center element which is perfectly aligned with the phase center of the horn antenna. Element $(0,1)$ is located one wavelength to the right of the center element, and elements $(2,0)$ and $(2,1)$ are located two wavelengths above elements $(0,0)$ and $(0,1)$, with one row of antennas in between. For certain antenna elements that are not aligned to the phase center of the SGH, an optimal distance d_{opt} exists where the wireless link efficiency is at its highest. For the aligned element (the center element) the efficiency of the link increases monotonically with decreasing separation distance d. For large distances d, all efficiencies converge to the same value, which is also the value predicted by the traditional Friis formula. The advantage of our method is that, by accounting for higher-order multipole interactions, a high accuracy is also obtained in the radiative near-field (Fresnel region), whereas the Friis formula can only lead to good results when the two devices are situated in each others far-field (Fraunhofer zone).

In this example, simulations have been carried out on an Intel® Core™ i7-2600 processor running at 3.40 GHz with 16 GB of memory. Calculation of the link efficiencies of the 5×5 elements of the antenna array using (6.17) for one fixed separation distance d between SGH and the wall only takes 0.25 s. This indicates the computational efficiency of our method. Indeed, for different antenna elements of the array, only the translation operator $T(\mathbf{r}_{\text{TX,RX}}, \hat{\mathbf{k}})$ has to be recalculated.

In a complete WPT system, every antenna element embedded in the wall is used as

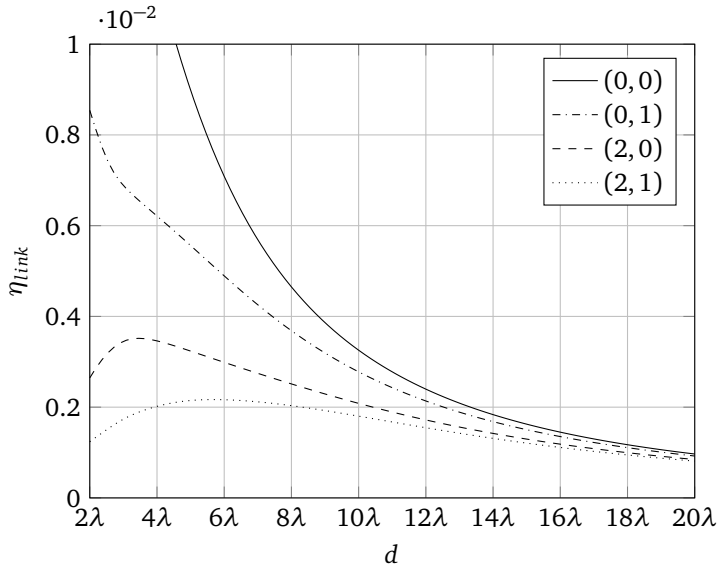

Figure 6.6: Efficiency of the wireless link η_{link} between the transmitting SGH and several receiving antenna elements embedded into the wall.

rectenna by connecting it via a matching circuit to a voltage doubler and rectifier circuit. This circuit converts the incoming AC power to DC power that is delivered to the load R_L. To obtain the complete PTE of the WPT system, the wireless link efficiency η_{link} should now be combined with the rectenna efficiency [22]. To compute the latter, a rectenna is designed and simulated in ADS. The circuit is shown in Fig. 6.7 and it is an often used configuration for rectennas used in WPT systems.

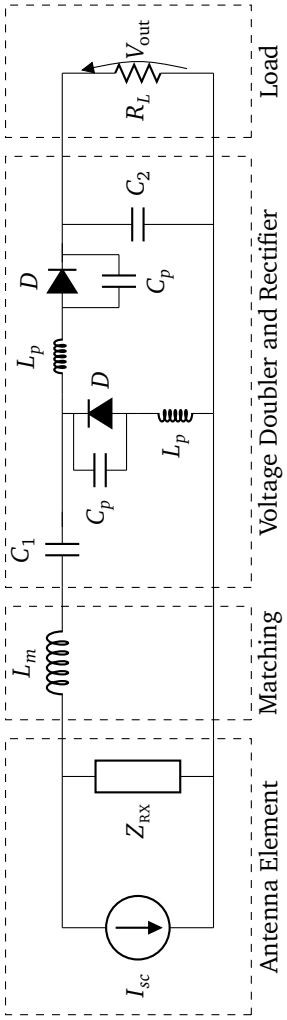

Figure 6.7: The complete schematic of a rectenna element as designed and simulated in ADS.

The receiving antenna element is replaced by its Norton equivalent. The resulting short-circuit current I_{sc} is given by (6.14) and the input impedance Z_{RX} is found using ADS. The antenna and the voltage doubler and rectifier circuit are matched using an inductor $L_m = 5\,\mathrm{nH}$. The voltage doubler and rectifier circuit itself consists of two HSMS-2850 Schottky diodes together with their package parasitics $C_p = 0.08\,\mathrm{pF}$ and $L_p = 2\,\mathrm{nH}$. For these diodes a pertinent SPICE model was used. The capacitors used are $C_1 = C_2 = 100\,\mathrm{pF}$ and this example was designed for a load resistance of $R_L = 100\,\Omega$. The matching circuit was designed to have optimal matching for $P_{\mathrm{RX}} = -10\,\mathrm{dBm}$. Since the input impedance of the voltage doubler and rectifier circuit depends on incoming power, due to the nonlinear diodes, the matching efficiency η_{match} also depends on the incoming power P_{RX}. Using a Harmonic Balance (HB) simulation in ADS, the input impedance of the voltage doubler and rectifier circuit is calculated for different incoming powers, from which the matching efficiency is then calculated as

$$\eta_{\mathrm{match}} = 1 - |\Gamma|^2 \tag{6.19}$$

$$= 1 - \left| \frac{Z_L - Z_{\mathrm{RX}}^*}{Z_L + Z_{\mathrm{RX}}} \right|^2 . \tag{6.20}$$

Here, Z_L is the input impedance of the matching circuit, which depends on P_{RX}. It should be noted that matching is performed for the groundtone of the HB simulation. The resulting matching efficiency is shown in Fig. 6.8. Furthermore, the efficiency of the voltage doubler and rectifier circuit η_{rect} is simply calculated by dividing the DC power delivered to the load by the AC power delivered to the input of the circuit. The total efficiency η_{tot} of the rectenna is found by combining both efficiencies as $\eta_{\mathrm{tot}} = \eta_{\mathrm{match}} \cdot \eta_{\mathrm{rect}}$. The results shown in Fig. 6.8 are similar to results shown in Fig. 7 and Fig. 10 in [22], indicating that we also consider a realistic voltage doubler and rectifier circuit. Using this voltage doubler and rectifier circuit on the measured and simulated data for the example considered in Fig. 6.5 ($P_{\mathrm{SGH}} = 10\,\mathrm{dBm}$, no brick wall), the DC power delivered to the load of the center antenna element is found and shown in Fig. 6.9. This again validates the method as a good agreement is observed. The error of about 1 dB is again attributed to losses of the horn antenna, connectors, and cables, which are not taken into account in the simulation. The total PTE of a single antenna element in the array inside the brick wall is found by combining the wireless link efficiency and the rectenna efficiency. The result is shown in Fig. 6.10 for different antenna elements. The power delivered to the transmitting SGH is again $P_{\mathrm{SGH}} = 10\,\mathrm{dBm}$. For the center element the efficiency rises with a lower separation distance d, but for certain other (misaligned) elements, there is an optimal distance d_{opt} at which the PTE becomes maximal. The large difference in PTE between the different elements of the array is obviously due to the directive nature of the radiation pattern of the SGH. If a more omnidirectional transmit antenna was chosen, the efficiency of the different elements would be more similar. It is now possible to obtain an efficiency of the complete WPT system by combining all the different single element PTEs.

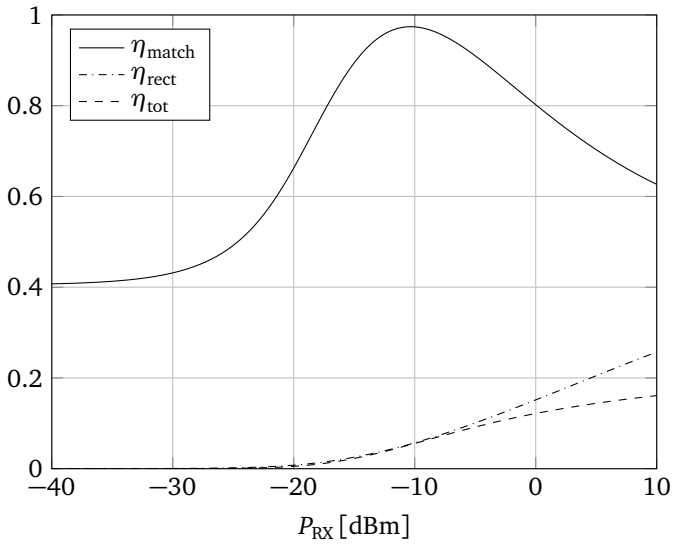

Figure 6.8: Matching efficiency (η_{match}), voltage doubler and rectifier efficiency (η_{rect}) and total efficiency (η_{tot}) of the rectenna. The matching network was designed for optimal matching when $P_{RX} = -10\,\text{dBm}$. The matching efficiency and the voltage doubler and rectifier efficiency are calculated using an HB simulation in ADS. The total efficiency of the rectenna is calculated as $\eta_{tot} = \eta_{match} \cdot \eta_{rect}$.

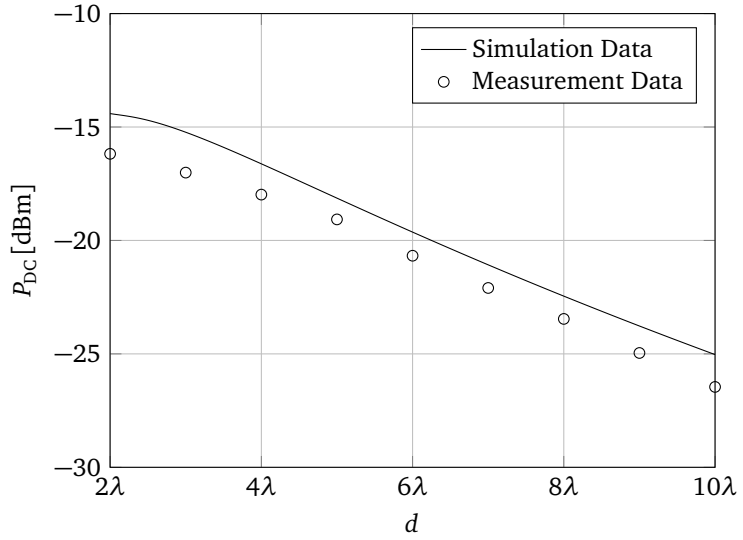

Figure 6.9: DC power delivered to the load of the center antenna element for measured and simulated data of the wireless link efficiency when the power delivered to the SGH is $P_{SGH} = 10\,\text{dBm}$ and no brick wall is present.

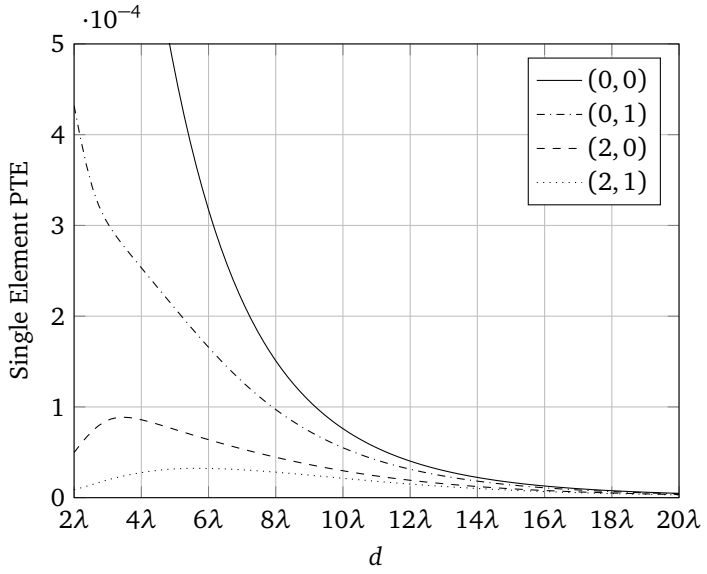

Figure 6.10: The PTE between the transmitting SGH and different receiving antenna elements embedded into the wall. For elements not aligned with the phase center of the SGH an optimal distance is again observed.

The result is shown in Fig. 6.11 where the PTE of the complete system is given by

$$\mathrm{PTE} = \frac{\sum_{i,j} P_{\mathrm{DC},ij}}{P_{\mathrm{TX}}}, \tag{6.21}$$

with $P_{\mathrm{DC},ij}$ the DC power delivered to the load of rectenna element $(i, j = -2, -1, 0, 1, 2)$.

6.4 Conclusions

In this chapter, we have presented a method to calculate the PTE of a WPT system in the radiative near-field. The method is computationally effective as it merely relies only on a single simulation (or measurement) of the radiation pattern of the antennas in the system. As long as there is no coupling via the reactive near-field between two transmitters, repositioning of the antennas can be done without large additional cost, making our method suitable for multi-receiver scenarios, as was abundantly shown in the application example. This example also demonstrated that investigating the behavior of WPT systems in the radiative near-field is imperative as the PTE does not always monotonically decrease with increasing distance between the antennas. Instead, for certain antenna elements, an optimal distance

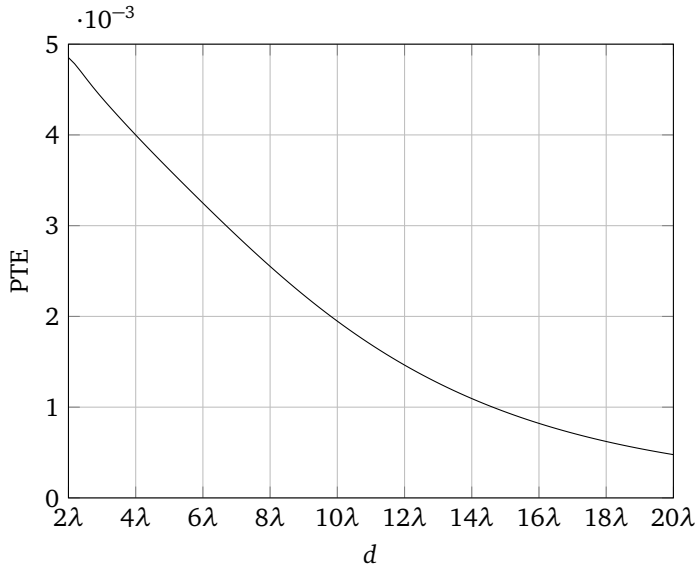

Figure 6.11: The total PTE of the complete WPT system. This includes the link efficiency, matching efficiency and efficiency of the voltage doubler and rectifier circuit.

where the PTE is maximal is found and the designers and users should be aware of this.

References

[1] I.-J. Yoon and H. Ling, "Investigation of near-field wireless power transfer under multiple transmitters", *IEEE Antennas and Wireless Propagation Letters*, vol. 10, pp. 662–665, 2011.

[2] ——, "Investigation of near-field wireless power transfer in the presence of lossy dielectric materials", *IEEE Transactions on Antennas and Propagation*, vol. 61, no. 1, pp. 482–488, Jan. 2013.

[3] ——, "Design of an electrically small circularly polarised turnstile antenna and its application to near-field wireless power transfer", *IET Microwaves, Antennas Propagation*, vol. 8, no. 5, pp. 308–314, Apr. 2014.

[4] K. Fotopoulou and B. Flynn, "Wireless power transfer in loosely coupled links: Coil misalignment model", *IEEE Transactions on Magnetics*, vol. 47, no. 2, pp. 416–430, Feb. 2011.

[5] B. Cannon, J. Hoburg, D. Stancil, and S. Goldstein, "Magnetic resonant coupling as a potential means for wireless power transfer to multiple small receivers", *IEEE Transactions on Power Electronics*, vol. 24, no. 7, pp. 1819–1825, Jul. 2009.

[6] A. Kurs, R. Moffatt, and M. Soljacic, "Simultaneous mid-range power transfer to multiple devices", *Applied Physics Letters*, vol. 96, no. 4, pp. 044 102–044102–3, Jan. 2010.

[7] J. Lee and S. Nam, "Fundamental aspects of near-field coupling small antennas for wireless power transfer", *IEEE Transactions on Antennas and Propagation*, vol. 58, no. 11, pp. 3442–3449, Nov. 2010.

[8] I.-J. Yoon and H. Ling, "Realizing efficient wireless power transfer using small folded cylindrical helix dipoles", *IEEE Antennas and Wireless Propagation Letters*, vol. 9, pp. 846–849, 2010.

[9] C. Balanis, *Antenna theory: Analysis and design*. Wiley, 1982.

[10] P. Li and L. J. Jiang, "Source reconstruction method-based radiated emission characterization for PCBs", *IEEE Transactions on Electromagnetic Compatibility*, vol. 55, no. 5, pp. 933–940, Oct. 2013.

[11] P. Kralicek, W. John, R. De Smedt, K. Vervoort, and H. Garbe, "A voltage controlled emission model of electromagnetic emission of IC for system analysis", in *IEEE International Symposium on Electromagnetic Compatibility*, Montreal, Quebec, 13-17 Aug. 2001, pp. 1197–1202.

[12] I. Erdin, M. Nakhla, and R. Achar, "Circuit analysis of electromagnetic radiation and field coupling effects for networks with embedded full-wave modules", *IEEE Transactions on Electromagnetic Compatibility*, vol. 42, no. 4, pp. 449–460, Nov. 2000.

[13] Y. Shao, Z. Peng, and J.-F. Lee, "Signal integrity analysis of high-speed interconnects by using nonconformal domain decomposition method", *IEEE Transactions on Components, Packaging and Manufacturing Technology*, vol. 2, no. 1, pp. 122–130, Jan. 2012.

[14] Z. Peng, K.-H. Lim, and J.-F. Lee, "Nonconformal domain decomposition methods for solving large multiscale electromagnetic scattering problems", *Proceedings of the IEEE*, vol. 101, no. 2, pp. 298–319, Feb. 2013.

[15] J. Van Bladel, *Electromagnetic Fields*. John Wiley & Sons, 2007.

[16] W. C. Chew, J.-M. Jin, E. Michielssen, and J. Song, *Fast and efficient algorithms in computational electromagnetics*. Artech House Publishers, 2001.

[17] W. C. Gibson, *The Method of Moments in Electromagnetics*. Chapman & Hall/CRC, 2008, ch. 4, pp. 73–79.

[18] J. Stratton, *Electromagnetic Theory*. McGraw-Hill, 1941.

[19] J. Van Bladel, "On the equivalent circuit of a receiving antenna", *IEEE Antennas and Propagation Magazine*, vol. 44, no. 1, pp. 164–165, Feb. 2002.

[20] G.-J. Stockman, H. Rogier, and D. Vande Ginste, "Efficient modeling of interactions between radiating devices with arbitrary relative positions and orientations", *IEEE Transactions on Electromagnetic Compatibility*, vol. 56, no. 6, pp. 1313–1321, Dec. 2014.

[21] R. Harrison and X. Le Polozec, "Nonsquarelaw behavior of diode detectors analyzed by the Ritz-Galerkin method", *IEEE Transactions on Microwave Theory and Techniques*, vol. 42, no. 5, pp. 840–846, May 1994.

[22] H. Visser and R. Vullers, "RF energy harvesting and transport for wireless sensor network applications: Principles and requirements", *Proceedings of the IEEE*, vol. 101, no. 6, pp. 1410–1423, Jun. 2013.

[23] L. Vallozzi, H. Rogier, and C. Hertleer, "Dual polarized textile patch antenna for integration into protective garments", *IEEE Antennas and Wireless Propagation Letters*, vol. 7, pp. 440–443, 2008.

[24] S. Stavrou and S. Saunders, "Review of constitutive parameters of building materials", in *Twelfth International Conference on Antennas and Propagation, 2003. (ICAP 2003)*, vol. 1, Mar. 2003, 211–215 vol.1.

7

Efficient Modeling of the Wireless Power Transfer Efficiency for Varying Positions and Orientations between Transmitter and Receiver

Based on "Efficient modeling of the wireless power transfer efficiency for varying positions and orientations between transmitter and receiver," Gert-Jan Stockman, Dries Vande Ginste and Hendrik Rogier, *IEEE MTT-S International Conference on Numerical Electromagnetic and Multiphysics Modeling and Optimization (NEMO)*, pp. 1-3, August 2015.

★ ★ ★

A method that efficiently calculates the Power Transfer Efficiency (PTE) of a Wireless Power Transfer (WPT) system is described in this chapter. It allows for arbitrary relative positions and orientations between devices in the system, both in far-field and radiative near-field configurations. The method uses a single simulation or measurement of the radiation patterns of the antennas employed in the WPT system, from which the interaction between devices at any relative position and orientation can be modeled. A spherical harmonics decomposition, together with Wigner-D rotation matrices, is applied to perform efficient translations and rotations of the devices used in the WPT system.

7.1 Introduction

Near-field Wireless Power Transfer (WPT) has gained more interest over the years due to its use in Radio Frequency Identification (RFID) systems [1]–[3]. In this chapter, we discuss a method to efficiently model the interaction between devices in the radiative near-field. In particular, it is shown that the electromagnetic interaction between devices in a WPT system with arbitrary position and orientation can be computed using a single simulation or measurement of the individual radiation patterns of these devices. This information is sufficient to model the Power Transfer Efficiency (PTE) in a realistic WPT system in the radiative near-field (and beyond) with high accuracy, for different possible configurations of the devices in the system. A meaningful application example illustrates the outlined theory.

In the sequel, all sources and fields are assumed to be time harmonic with angular frequency ω and with time dependencies $e^{j\omega t}$ suppressed. Unit vectors are denoted with a "hat", e.g. $\hat{\mathbf{v}}$.

7.2 Formalism

Consider two antennas, a transmitter TX and a receiver RX, with radiation patterns $\mathbf{F}_{\text{TX}}(\hat{\mathbf{k}})$ and $\mathbf{F}_{\text{RX}}(\hat{\mathbf{k}})$, respectively, where $\hat{\mathbf{k}} = \sin\theta\cos\phi\,\hat{\mathbf{x}} + \sin\theta\sin\phi\,\hat{\mathbf{y}} + \cos\theta\,\hat{\mathbf{z}}$. Then it was shown in [4] that, in the radiative near-field, the short-circuit current I_{sc} at the terminals of the receiver can be described as

$$I_{sc} = -\frac{1}{ZV_0}\int_{\Omega} T(\mathbf{r}_{\text{TX,RX}}, \hat{\mathbf{k}})\mathbf{F}_{\text{TX}}(\hat{\mathbf{k}}) \cdot \mathbf{F}_{\text{RX}}(-\hat{\mathbf{k}})\,\mathrm{d}\hat{\mathbf{k}}. \tag{7.1}$$

Here, we integrate over the Ewald sphere Ω. Furthermore, V_0 is a normalization factor, Z the wave impedance of the background medium, $\mathbf{r}_{\text{TX,RX}}$ the vector between the phase center of the receiver and the phase center of the transmitter, and $T(\mathbf{r}_{\text{TX,RX}}, \hat{\mathbf{k}})$ the translation operator. Expression (7.1) is valid as long as the two antennas (devices) are not positioned in each other's reactive near-field. We will now extend the above result into a formalism that is of practical use for the calculation of the PTE in a WPT system. Thereto, first, we want to be able to efficiently turn the antennas about their phase center. This can be done by applying the appropriate rotation $\mathcal{R}$ to the radiation patterns of the devices. The rotation is efficiently performed in the spherical harmonics domain ($\mathcal{R}_{\text{SH}}$), as shown in Fig 7.1. The transformation to the spherical harmonics domain $\mathcal{F}$ and its inverse $\mathcal{F}^{-1}$ are given by (7.2) and (7.3), respectively:

$$\begin{aligned}\mathcal{F} \longleftrightarrow \begin{Bmatrix} A_{pq} \\ B_{pq} \end{Bmatrix} = \frac{-1}{p(p+1)} \int_0^{2\pi}\int_0^{\pi} \Bigg[q \begin{Bmatrix} jF_\phi(\theta,\phi) \\ -F_\theta(\theta,\phi) \end{Bmatrix} Y_{pq}^*(\theta,\phi) \\ + \sin\theta \begin{Bmatrix} -F_\theta(\theta,\phi) \\ jF_\phi(\theta,\phi) \end{Bmatrix} \frac{\mathrm{d}Y_{pq}^*(\theta,\phi)}{\mathrm{d}\theta} \Bigg] \mathrm{d}\theta\,\mathrm{d}\phi,\end{aligned} \tag{7.2}$$

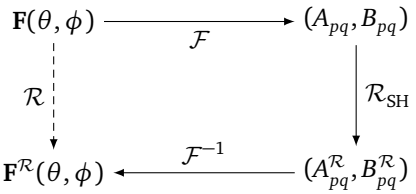

Figure 7.1: Rotation of $\mathbf{F}(\theta,\phi)$ to $\mathbf{F}^{\mathcal{R}}(\theta,\phi)$ using the spherical harmonics domain.

$$\mathcal{F}^{-1}\longleftrightarrow\begin{Bmatrix}F_\theta(\theta,\phi)\\F_\phi(\theta,\phi)\end{Bmatrix}=\sum_{p=0}^{P}\sum_{|q|\leq p}\left[\begin{Bmatrix}A_{pq}\\jB_{pq}\end{Bmatrix}\frac{\mathrm{d}Y_{pq}(\theta,\phi)}{\mathrm{d}\theta}+\begin{Bmatrix}B_{pq}\\jA_{pq}\end{Bmatrix}\frac{qY_{pq}(\theta,\phi)}{\sin\theta}\right]. \tag{7.3}$$

Here, $Y_{pq}(\theta,\phi)$ are the orthonormalized scalar spherical harmonics and P is a parameter that determines the accuracy.

In Fig. 7.1, the transformation $\mathcal{R}$ represents the desired rotation in the spatial domain. The rotation itself is performed in the spherical harmonics domain by the transformation $\mathcal{R}_{\mathrm{SH}}$ that makes use of Wigner D-matrices. The rotated coefficients of the spherical harmonics expansion are calculated as [5]

$$\mathcal{R}_{\mathrm{SH}}\longleftrightarrow\begin{Bmatrix}A^{\mathcal{R}}_{pq}\\B^{\mathcal{R}}_{pq}\end{Bmatrix}=\begin{Bmatrix}A_{pq}\\B_{pq}\end{Bmatrix}\sum_{|r|\leq p}e^{-jq\gamma}d^{r}_{pq}(\beta)e^{-jr\alpha}, \tag{7.4}$$

with $d^{r}_{pq}(\beta)$ the Wigner small d-matrix, given by [6]

$$\begin{aligned}d^{r}_{pq}(\beta)=&(-1)^{r-q}\sqrt{(p+r)!(p-r)!(p+q)!(p-q)!}\\&\cdot\sum_{s}(-1)^{s}\frac{\left(\cos\frac{\beta}{2}\right)^{2(p-s)+q-r}\left(\sin\frac{\beta}{2}\right)^{2s-q+r}}{(p+q-s)!s!(r-q+s)!(p-r-s)!}.\end{aligned} \tag{7.5}$$

Here, the range of s is determined by the condition that all factorials are nonnegative, thus $s\in[\max(0,q-r),\min(p+q,p-r)]$. In (7.4)-(7.5), α, β and γ are the standard Euler angles that define the rotation using the $z-y-z$ convention in a right-handed frame. The Euler angles (α,β,γ) are readily related to the desired inclination and azimuthal angles θ and ϕ, by choosing $\alpha=\phi$, $\beta=\theta$ and $\gamma=0$.

Second, the rotation mechanism of Fig. 7.1 can be combined with a translation, by simply changing $\mathbf{r}_{\mathrm{TX,RX}}$ in the translation operator $T(\mathbf{r}_{\mathrm{TX,RX}},\hat{\mathbf{k}})$ in (7.1). Consequently, we are now able to calculate the wireless link efficiency between devices in a WPT system, positioned anywhere in space, and with any relative orientation. To calculate the wireless link efficiency, we need the power delivered to the receiving antenna. Fig. 6.2 represents the equivalent circuit of a WPT link. The wireless

link efficiency can now be written as

$$\eta_{\text{link}} = \frac{P_{\text{RX}}}{P_{\text{TX}}} = \frac{\frac{1}{2}\Re\left(Z_L \left|I_{sc}\right|^2 \left|\frac{Z_{\text{RX}}}{Z_{\text{RX}}+Z_L}\right|^2\right)}{\frac{1}{2Z}\int\limits_{\Omega} |\mathbf{F}_{\text{TX}}(\hat{\mathbf{k}})|^2 \, \mathrm{d}\hat{\mathbf{k}}}, \tag{7.6}$$

with the numerator representing the power delivered to the receiving antenna's load Z_L and the denominator the power emitted by the (rotated) transmitter with (rotated) radiation pattern $\mathbf{F}_{\text{TX}}(\hat{\mathbf{k}})$.

To extend the wireless link efficiency to the PTE, we need the ratio of Direct Current (DC) power dissipated in the load R_L at the receiving side to the Alternating Current (AC) power delivered to the transmit antenna. Assuming no radiation losses, this AC power equals P_{TX}. The DC power delivered to the load is found by combining the link efficiency calculated in (7.6) with the efficiency of the matching circuit and of the rectifier. Since the input impedance Z_L of a nonlinear circuit depends on the incoming power, the efficiency of the matching network, denoted η_{match}, will also have this dependency. This matching efficiency can be simulated using commercial tools such as Advanced Design System (ADS). The efficiency of the rectifier circuit itself can be calculated by comparing the DC power, delivered to the load resistor R_L, to the incoming power $P_{\text{inc}} = \eta_{\text{match}} \cdot P_{\text{RX}}$, injected into the rectifier circuit, i.e. $\eta_{\text{rect}} = P_{\text{inc}}/P_{\text{DC}}$. The DC power P_{DC} delivered to the load R_L is calculated as $P_{\text{DC}} = V_{\text{out}}^2/R_L$ where the DC output voltage V_{out} may also be found from simulation tools such as ADS. The PTE of the complete system is given by $\text{PTE} = P_{\text{DC}}/P_{\text{TX}} = \eta_{\text{link}} \cdot \eta_{\text{match}} \cdot \eta_{\text{rect}}$.

7.3 Application Example

To demonstrate the practical applicability and the efficiency of our method, an application example is considered. As the transmitting device, we choose a Standard Gain Horn (SGH) antenna radiating at 1.5 GHz with a power of 10 dBm. As the receiving device, an inset fed microstrip patch antenna, also designed to resonate at 1.5 GHz, is used. The antennas are placed at a separation distance $d = 5\lambda$ as shown in Fig. 7.2. The patch antenna is rotated using the $z-y-z$ convention in a right-handed frame over $-\pi/2 \leq \alpha = \phi \leq \pi/2$, $-\pi/2 \leq \beta = \theta \leq \pi/2$ and $\gamma = 0$ for a total of 91×91 points. At the receiving end, a rectifier was attached to the patch antenna to form a rectenna. This complete rectenna was designed in ADS and consists of a matching network, a voltage doubler and a rectifier as shown in Fig. 6.7.

The antenna and the voltage doubler and rectifier circuit are matched using an inductor $L_m = 5$ nH. The voltage doubler and rectifier circuit itself consists of two HSMS-2850 Schottky diodes together with their package parasitics $C_p = 0.08$ pF and $L_p = 2$ nH. For these diodes a pertinent SPICE model was used. The capacitors used are $C_1 = C_2 = 100$ pF and this example was designed for a load resistance of

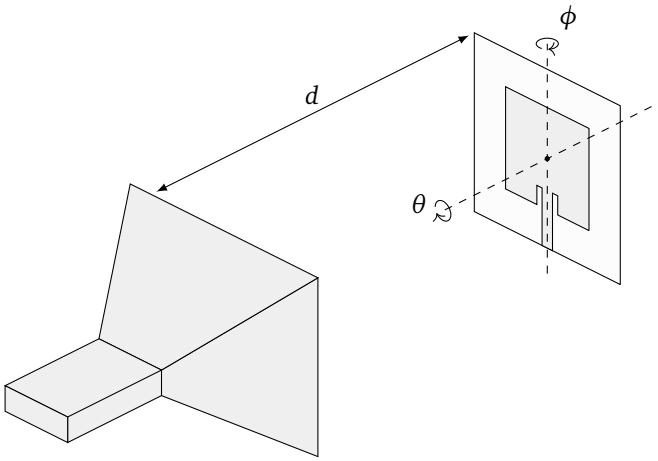

Figure 7.2: Simulation setup where an SGH acts as transmitter and a patch antenna as receiver.

$R_L = 100\,\Omega$. The matching circuit was designed to have optimal matching when $P_{\text{RX}} = -10\,\text{dBm}$. Since the input impedance of the voltage doubler and rectifier circuit depends on incoming power, due to the nonlinear diodes, the matching efficiency η_{match} also depends on the incoming power P_{RX}. Using a harmonic balance simulation in ADS, the input impedance of the voltage doubler and rectifier circuit is calculated for different incoming powers, from which the matching efficiency is then calculated as

$$\eta_{\text{match}} = 1 - \left| \frac{Z_L(P_{\text{RX}}) - Z_{\text{RX}}^*}{Z_L(P_{\text{RX}}) + Z_{\text{RX}}} \right|^2 . \tag{7.7}$$

Here, $Z_L(P_{\text{RX}})$ is the input impedance of the matching circuit, depending on the incoming power to the matching circuit. Furthermore, the efficiency of the voltage doubler and rectifier circuit η_{rect} is simply calculated by dividing the DC power delivered to the load by the AC power delivered to the input of this circuit. Subsequently, these efficiencies can be combined with the wireless link efficiency η_{link} to obtain the complete PTE over all angles, by substituting the appropriate rotated radiation patterns of the devices in (7.1). Here, the radiation pattern of the SGH is calculated analytically and the radiation pattern of the patch antenna is obtained using ADS. The rotations are performed using the spherical harmonics domain as explained above with $P = 10$. The resulting PTE for all 91×91 angles is given in Fig. 7.3. The average simulation time per sample is 92 ms. All simulations have been carried out on an Intel® Core™ i7-2600 processor running at 3.40 GHz and with 16 GB of memory.

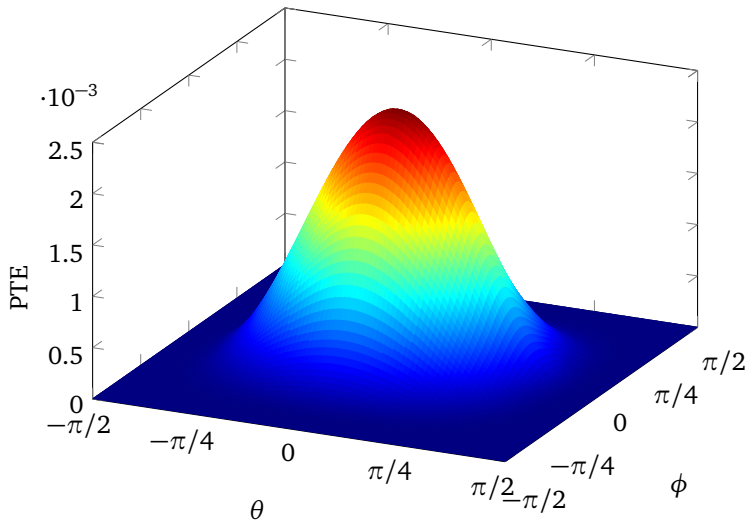

Figure 7.3: PTE of the complete WPT system calculated for $-\pi/2 \leq \phi \leq \pi/2$ and $-\pi/2 \leq \theta \leq \pi/2$ and a separation distance $d = 5\lambda$.

7.4 Conclusions

We have proposed a method to efficiently predict the PTE of a complete WPT system in the radiative near-field. The method relies on a single measurement or simulation of the radiation patterns of the devices in the system. The formalism explained in this chapter, allows to account for any relative position or orientation of the devices without requiring a new simulation for every alteration.

References

[1] A. Buffi, P. Nepa, and G. Manara, "Analysis of near-field coupling in UHF-RFID systems", in *2011 IEEE-APS Topical Conference on Antennas and Propagation in Wireless Communications (APWC)*, Sep. 2011, pp. 931–934.

[2] J. Lee and S. Nam, "Fundamental aspects of near-field coupling small antennas for wireless power transfer", *IEEE Transactions on Antennas and Propagation*, vol. 58, no. 11, pp. 3442–3449, Nov. 2010.

[3] H. Visser and R. Vullers, "RF energy harvesting and transport for wireless sensor network applications: Principles and requirements", *Proceedings of the IEEE*, vol. 101, no. 6, pp. 1410–1423, Jun. 2013.

[4] G.-J. Stockman, H. Rogier, and D. Vande Ginste, "Efficient modeling of interactions between radiating devices with arbitrary relative positions and orientations", *IEEE Transactions on Electromagnetic Compatibility*, vol. 56, no. 6, pp. 1313–1321, Dec. 2014.

[5] R. Hoover, A. Maciejewski, and R. Roberts, "Pose detection of 3-D objects using images sampled on SO(3), spherical harmonics, and Wigner-D matrices", in *IEEE International Conference on Automation Science and Engineering, CASE.*, Arlington, Virginia, 23-26 Aug. 2008, pp. 47–52.

[6] Z. Gimbutas and L. Greengard, "A fast and stable method for rotating spherical harmonic expansions", *Journal of Computational Physics*, vol. 228, pp. 5621–5627, May 2009.

8 Conclusion

8.1 General Conclusions

In this dissertation, a novel method was developed that allows the efficient modeling of electromagnetic interactions between electronic devices or systems up until the radiative near-field. The method was proven to be accurate and efficient in comparison to commercial full-wave solvers, especially when the devices are subject to translation or rotation. Our novel technique was demonstrated for two types of applications, i.e., modeling of the Electromagnetic Compatibility (EMC) behavior, either as a form of pre-compliance testing or to assess interactions within an electronic system and modeling of the link efficiency in Wireless Power Transfer (WPT) systems. However, the method is in general applicable to any application domain where interactions between devices in close proximity are playing a prominent role.

In Part I, the method was elaborated and used in the context of predicting the inter- and intra-system EMC behavior in simulation as a form of flexible and inexpensive pre-compliance testing. To this end, the formalism was first described in Chapter 2 where the basic case of two one-port devices in an anechoic chamber was considered. The complexity of the problem was tackled and reduced by writing the interaction between electronic devices or systems in terms of their radiation patterns. It also allowed for highly efficient rotations of the devices by using the transformation to the spherical harmonics domain where rotations can be performed using Wigner-D matrices with low computational cost. Furthermore, the method was proven to be accurate up until the radiative near-field. Subsequently, the formalism was extended to account for multiple non-collocated noise source in Chapter 3 and also to semi-anechoic conditions in Chapter 4. All this has led to efficient modeling of inter-system EMC behavior and thus to mimicking compliance tests. In Chapter 5, we focused on the intra-system EMC behavior, i.e., the

electromagnetic interactions within a system itself, by extending the novel method to account for multiport devices. This multiport approach, for which new definitions for the radiation patterns of the devices were introduced, proved to be highly efficient as the novel techniques that were introduced in Chapters 2–4 for one-port devices were still applicable. Using several application and validation examples, by means of measurements as well as simulations, the efficiency and appositeness of our novel method has been demonstrated thoroughly. Since the operating frequency and complexity of electronic systems keep increasing, these forms of pre-compliance testing will prove to be invaluable in the future.

Another domain in which the efficient modeling of electromagnetic interactions is necessary, is in the development of WPT systems. In these systems energy is transmitted wirelessly to a receiving device, to remove the need for power cabling. This is useful for several applications such as the powering of sensor networks. WPT systems are often applied in the radiative near-field, making our novel method very suitable. In Chapters 6 and 7, the novel method that models the electromagnetic interactions between devices up until the radiative near-field was combined with circuit and antenna theory to obtain a prediction of the link efficiency of such a WPT system, i.e., the amount of Direct Current (DC) power obtained at the receiving device due to the transmitted Alternating Current (AC) power by a transmitting device. Again, application and validation examples demonstrate the accuracy and efficiency of this method, proving its applicability during the design of WPT systems. The design of these systems is of increasing importance and it is predicted that in the near future, an almost unlimited number of monitoring applications will require large-scale development of cooperative wireless microsystems with sensing capabilities. In this regard, computer-aided design of WPT systems is important and the advocated novel method will play a crucial role in this process.

8.2 Future Work

While the proposed technique allows for the efficient modeling of the electromagnetic interactions of complex Printed Circuit Boards (PCBs) and complete electronic products, it is in essence a frequency-domain technique, meaning only a single frequency is analyzed at a time. Dealing simultaneously with several frequencies or a frequency band would allow for studying broadband systems or systems with multiple frequency components. This would for example pave the way for taking nonlinearities in the system into account, which in turn yields the modeling of active components by considering multiple higher order frequency components. In this way, complex digital electronic circuits or systems, consisting of several Integrated Circuits (ICs) could be characterized, as long as their nonlinear models are available.

To optimize the modeling of complete PCBs, also surface waves, excited and traveling in the substrate of a PCB, should also be taken into account. Clearly, in this case, only considering the radiation patterns is no longer sufficient.

In this work, the method has been applied to anechoic and semi-anechoic conditions. These are conditions that exist only in a laboratory environment, such as an EMC test. In certain applications that take place outside of a lab environment (such as indoor positioning), the channel can exhibit multipath. An extension could be made that allows any generic channel model to be integrated in the formalism, as such broadening the range of applications of our technique.

The presented technique is valid up until the radiative near-field. For interactions in the non-radiative (or reactive) near-field, the method could potentially be adjusted by making use of a multipole description instead of using the far-field radiation patterns. This could perhaps lead to an efficient and accurate technique for applications such as inductive charging of electronic devices or Near-Field Communication.

All of the above proposed extensions, to account for multiple frequencies, nonlinearities, surface waves in PCBs, complex channel characteristics, and for reactive near-field interactions, will require thorough validation. Thereto, when commercial full-wave solvers can not yield a reference solution, accurate and novel measurement techniques will have to be devised.

Finally, the formalism described in this work was implemented in MATLAB®. However, it is possible to describe it as an extended S-parameter model approach. In such an approach, the scattering parameters of a device are extended by adding an extra radiation port. This radiation port takes the interaction between devices in the system into account by leveraging the presented technique. Right now, conventional circuit solvers only calculate the interaction via conductive paths. Consequently, integration of the advocated method into commercial circuit solvers, by using an extra port in their standard S-parameter description, is interesting to further investigate.

A

Spherical Harmonics Expansion

To find the coefficients A_{pq} and B_{pq} of the spherical harmonics expansion (2.16) we first note that

$$jqF_{\phi}(\theta,\phi)+\frac{\mathrm{d}}{\mathrm{d}\theta}\big[\sin\theta F_{\theta}(\theta,\phi)\big]=-\sum_{p=0}^{P}\sum_{|q|\leq p}\Big[p(p+1)A_{pq}Y_{pq}(\theta,\phi)\sin\theta\Big] \quad \text{(A.1)}$$

$$\frac{\mathrm{d}}{\mathrm{d}\theta}\big[\sin\theta F_{\phi}(\theta,\phi)\big]-jqF_{\theta}(\theta,\phi)=-j\sum_{p=0}^{P}\sum_{|q|\leq p}\Big[p(p+1)B_{pq}Y_{pq}(\theta,\phi)\sin\theta\Big] \quad \text{(A.2)}$$

which has been obtained by the use of the following recursive properties of the scalar spherical harmonics:

$$\frac{dY_{pq}(\theta,\phi)}{d\theta}=\frac{p\cos\theta Y_{pq}(\theta,\phi)-\sqrt{p^2-q^2}\sqrt{\frac{2p+1}{2p-1}}Y_{p-1,q}(\theta,\phi)}{\sqrt{1-\cos^2\theta}} \quad \text{(A.3)}$$

and

$$Y_{pq}(\theta,\phi)\sqrt{\frac{2p-1}{2p+1}}\sqrt{p^2-q^2}=Y_{p-1,q}(\theta,\phi)(2p-1)\cos\theta - Y_{p-2,q}(\theta,\phi)\sqrt{\frac{2(p-1)+1}{2(p-1)-1}}\sqrt{(p-1)^2-q^2}, \quad \text{(A.4)}$$

where $\sqrt{1-\cos^2\theta}=\sin\theta$ over the Ewald sphere Ω ($\theta\in[0,\pi]$) and where $Y_{pq}(\theta,\phi)$ are the orthonormalized scalar spherical harmonics given by [1]

$$Y_{pq}(\theta,\phi)=\sqrt{\frac{(2p+1)}{4\pi}\frac{(p-q)!}{(p+q)!}}P_p^q(\cos\theta)e^{jq\phi}. \quad \text{(A.5)}$$

Here, $P_p^q(\cdot)$ is the associated Legendre polynomial of degree p and order q. If we now multiply the left- and right-hand side of (A.1) and (A.2) with $Y^*_{p'q}(\theta,\phi)$, integrate both sides over the Ewald's sphere and use the following orthonormality property of the orthonormalized spherical harmonics:

$$\int_{\phi=0}^{2\pi}\int_{\theta=0}^{\pi} Y_{pq}(\theta,\phi)Y^*_{p'q'}(\theta,\phi)\sin\theta\,\mathrm{d}\theta\,\mathrm{d}\phi = \delta_{pp'}\delta_{qq'}, \tag{A.6}$$

where $*$ denotes the complex conjugate, δ the Kronecker delta and together with the fact that

$$\begin{aligned}
&\int_{\theta=0}^{\pi}\frac{\mathrm{d}}{\mathrm{d}\theta}\Big[\Big(\sin\theta F_\theta(\theta,\phi)\Big)Y_{pq}(\theta,\phi)\Big]\mathrm{d}\theta \\
&= \int_{\theta=0}^{\pi} Y_{pq}(\theta,\phi)\frac{\mathrm{d}}{\mathrm{d}\theta}\Big(\sin\theta F_\theta(\theta,\phi)\Big)\mathrm{d}\theta + \int_{\theta=0}^{\pi}\sin\theta F_\theta(\theta,\phi)\frac{\mathrm{d}Y_{pq}(\theta,\phi)}{\mathrm{d}\theta}\mathrm{d}\theta && \text{(A.7)}\\
&= \Big[\Big(\sin\theta F_\theta(\theta,\phi)\Big)Y_{pq}(\theta,\phi)\Big]\Big|_{\theta=\pi} - \Big[\Big(\sin\theta F_\theta(\theta,\phi)\Big)Y_{pq}(\theta,\phi)\Big]\Big|_{\theta=0} && \text{(A.8)}\\
&= 0 && \text{(A.9)}
\end{aligned}$$

such that

$$\int_{\theta=0}^{\pi} Y_{pq}(\theta,\phi)\frac{\mathrm{d}}{\mathrm{d}\theta}\Big(\sin\theta F_\theta(\theta,\phi)\Big)\mathrm{d}\theta = -\int_{\theta=0}^{\pi}\sin\theta F_\theta(\theta,\phi)\frac{\mathrm{d}Y_{pq}(\theta,\phi)}{\mathrm{d}\theta}\mathrm{d}\theta. \tag{A.10}$$

Then we obtain the following expressions for the sought-for coefficients:

$$A_{pq} = -\frac{1}{p(p+1)}\int_{\phi=0}^{2\pi}\int_{\theta=0}^{\pi}\Big[jqF_\phi(\theta,\phi)Y^*_{pq}(\theta,\phi) - F_\theta(\theta,\phi)\frac{\mathrm{d}Y^*_{pq}(\theta,\phi)}{\mathrm{d}\theta}\sin\theta\Big]\mathrm{d}\theta\mathrm{d}\phi, \tag{A.11}$$

$$B_{pq} = -\frac{j}{p(p+1)}\int_{\phi=0}^{2\pi}\int_{\theta=0}^{\pi}\Big[jqF_\theta(\theta,\phi)Y^*_{pq}(\theta,\phi) + F_\phi(\theta,\phi)\frac{\mathrm{d}Y^*_{pq}(\theta,\phi)}{\mathrm{d}\theta}\sin\theta\Big]\mathrm{d}\theta\mathrm{d}\phi. \tag{A.12}$$

For the special limit case $p = q = 0$, the coefficients A_{00} and B_{00} become

$$A_{00} = -\frac{1}{2\sqrt{\pi}} \int_{\phi=0}^{2\pi} \int_{\theta=0}^{\pi} \Big[jF_{\phi}(\theta,\phi) - \frac{\sin 2\theta}{2} F_{\theta}(\theta,\phi) \Big] \mathrm{d}\theta \mathrm{d}\phi, \tag{A.13}$$

$$B_{00} = -\frac{j}{2\sqrt{\pi}} \int_{\phi=0}^{2\pi} \int_{\theta=0}^{\pi} \Big[\frac{\sin 2\theta}{2} F_{\phi}(\theta,\phi) + jF_{\theta}(\theta,\phi) \Big] \mathrm{d}\theta \mathrm{d}\phi. \tag{A.14}$$

References

[1] *NIST digital library of mathematical functions*, http://dlmf.nist.gov/, Release 1.0.5 of 2012-10-01.

B

Method of Moments for Wire Antennas

For an introduction to the modeling of wire antennas, the reader is referred to [1]. In this work, we start from the Electric Field Integral Equation (EFIE), where the boundary integral equations are solved by the Method of Moments (MoM) [2]. In this appendix we mainly focus on the computation of the pertinent system matrix, evolving from the MoM.

The set of equations to solve in the MoM is given by the matrix equation $V = Z \cdot I$, where Z is the so-called system or impedance matrix, V the known source excitation vector and I the sought-for current vector. The expression for an element Z_{mn} of the interaction matrix is given by [1]

$$Z_{mn} = -j\omega\mu\Big[\int_{\mathbf{f}_m} f_m(l)\hat{\mathbf{t}}(l) \cdot \int_{\mathbf{f}_n} f_n(l')\hat{\mathbf{t}}(l')G(\mathbf{r},\mathbf{r}')\,\mathrm{d}l'\,\mathrm{d}l - \frac{1}{k^2}\int_{\mathbf{f}_m} \dot{f}_m(l)\int_{\mathbf{f}_n} \dot{f}_n(l')G(\mathbf{r},\mathbf{r}')\,\mathrm{d}l'\,\mathrm{d}l\Big], \tag{B.1}$$

where $f_m(l)$ and $f_n(l')$ are scalar triangle functions expressed in terms of the parametrized wire location l, $\dot{f}_m(l)$ and $\dot{f}_n(l)$ are their derivatives with respect to l, and $\hat{\mathbf{t}}(l)$ and $\hat{\mathbf{t}}(l')$ are the associated wire tangent vectors. For ascending and descending triangle functions of the form l/Δ and $(\Delta - l)/\Delta$, the derivatives are $1/\Delta$ and $-1/\Delta$, respectively. Here, Δ is the length of one discretization segment (assuming all segments have the same length). For near interactions, i.e. for position vectors $\mathbf{r}$ and $\mathbf{r}'$ in (B.1) that are close to each other, we rewrite the 3D Green's function

as a sum of its regular and singular part.

$$G(\mathbf{r},\mathbf{r}') = \frac{e^{-jk|\mathbf{r}-\mathbf{r}'|}}{4\pi|\mathbf{r}-\mathbf{r}'|} = \underbrace{\frac{e^{-jk|\mathbf{r}-\mathbf{r}'|}-1}{4\pi|\mathbf{r}-\mathbf{r}'|}}_{\text{regular}} + \underbrace{\frac{1}{4\pi|\mathbf{r}-\mathbf{r}'|}}_{\text{singular}}. \tag{B.2}$$

Integrals including the regular part can be calculated numerically, e.g., by Gaussian quadrature sampling. When the singular part forms the kernel of the integral, the integral should be evaluated analytically. For far interactions, the Green's function does not need to be decomposed, and the corresponding integrals are also computed numerically.

Self-Patch

Self-patch interactions occur when $m = n$ in (B.1), and hence, these are the near interactions that lead to the elements on the diagonal of Z. For a self-patch, four types of contributions are considered (see Fig. B.1). Due to symmetry, the con-

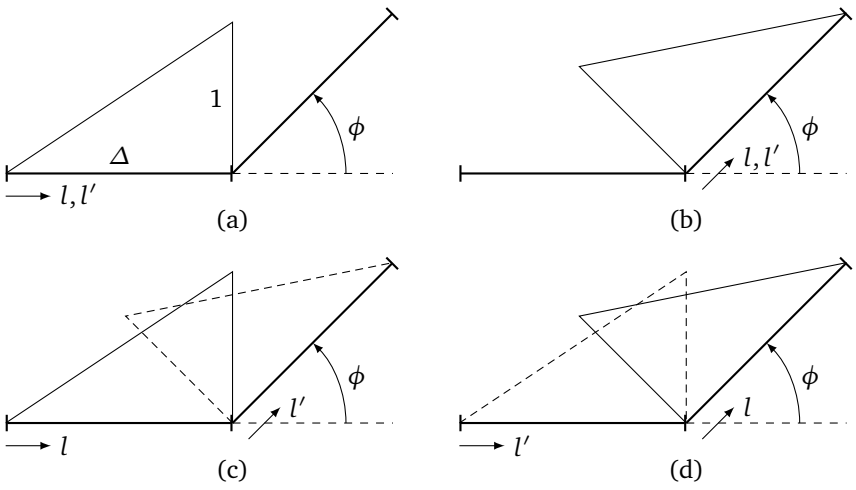

Figure B.1: Different contributions to the self-patch (triangles = rooftop functions). (a) up-up; (b) down-down; (c) up-down; (d) down-up.

tribution Z_{mn} to the system matrix for contributions (a) and (b) are identical, as well as (c) and (d). We now calculate Z_{mn} for the contributions (a) and (b), using

(B.1). For the first term of (B.1) we get

$$Z_{mn,1} = \frac{1}{4\pi} \int_{l=0}^{\Delta} \frac{l}{\Delta} \int_{l'=0}^{\Delta} \frac{l'}{\Delta} \frac{e^{-jkr}}{r} \, \mathrm{d}l' \, \mathrm{d}l \tag{B.3}$$

$$= \frac{1}{4\pi} \Big[\underbrace{\int_{l=0}^{\Delta} \frac{l}{\Delta} \int_{l'=0}^{\Delta} \frac{l'}{\Delta} \frac{e^{-jkr}-1}{r} \, \mathrm{d}l' \, \mathrm{d}l}_{\zeta_1} + \int_{l=0}^{\Delta} \frac{l}{\Delta} \int_{l'=0}^{\Delta} \frac{l'}{\Delta} \frac{1}{r} \, \mathrm{d}l' \, \mathrm{d}l \Big]. \tag{B.4}$$

Here we use $r = \sqrt{(l-l')^2 + a^2}$, with a the radius of the antenna wire. The first term ζ_1 is regular and is calculated numerically. After performing analytical integration (over l') of the second term, we get

$$Z_{mn,1} = \frac{1}{4\pi} \Big[\zeta_1 + \int_{l=0}^{\Delta} \frac{l}{\Delta} \Big[\frac{1}{\Delta} \Big(\sqrt{a^2 + (\Delta - l)^2} - \sqrt{a^2 + l^2} + l \ln \Big[\frac{(\Delta - l) + \sqrt{a^2 + (\Delta - l)^2}}{\sqrt{a^2 + l^2} - l} \Big] \Big) \Big] \mathrm{d}l \Big] \tag{B.5}$$

$$= \frac{1}{4\pi} \Big[\zeta_1 + \int_{l=0}^{\Delta} \frac{l}{\Delta} S_1(l) \, \mathrm{d}l \Big]. \tag{B.6}$$

Note that the singularity has now vanished. Hence (B.6) can be calculated numerically with Gaussian quadrature integration (M weights w_p and sample points l_p) as

$$Z_{mn,1} = \frac{1}{4\pi} \Big[\zeta_1 + \sum_{p=1}^{M} w_p(l_p) \frac{l_p}{\Delta} S_1(l_p) \Big]. \tag{B.7}$$

For the second term of (B.1) we obtain

$$Z_{mn,2} = -\frac{1}{k^2}\cdot\frac{1}{4\pi}\int_{l=0}^{\Delta}\frac{1}{\Delta}\int_{l'=0}^{\Delta}\frac{1}{\Delta}\frac{e^{-jkr}}{r}\,\mathrm{d}l'\,\mathrm{d}l \tag{B.8}$$

$$= -\frac{1}{k^2\Delta^2}\cdot\frac{1}{4\pi}\Big[\underbrace{\int_{l=0}^{\Delta}\int_{l'=0}^{\Delta}\frac{e^{-jkr}-1}{r}\,\mathrm{d}l'\,\mathrm{d}l}_{\zeta_2} + \int_{l=0}^{\Delta}\int_{l'=0}^{\Delta}\frac{1}{r}\,\mathrm{d}l'\,\mathrm{d}l\Big] \tag{B.9}$$

$$= -\frac{1}{k^2\Delta^2}\cdot\frac{1}{4\pi}\Big[\zeta_2 + \int_{l=0}^{\Delta}\ln\Big[\frac{(\Delta-l)+\sqrt{a^2+(\Delta-l)^2}}{\sqrt{a^2+l^2}-l}\Big]\mathrm{d}l\Big] \tag{B.10}$$

$$= -\frac{1}{k^2\Delta^2}\cdot\frac{1}{4\pi}\Big[\zeta_2 + \int_{l=0}^{\Delta}S_2(l)\,\mathrm{d}l\Big] \tag{B.11}$$

$$= -\frac{1}{k^2\Delta^2}\cdot\frac{1}{4\pi}\Big[\zeta_2 + \sum_{p=1}^{M}w_p(l_p)S_2(l_p)\Big]. \tag{B.12}$$

Combining the two contributions $Z_{mn,1}$ and $Z_{mn,2}$ and taking into account that contributions (a) and (b) from Fig. B.1 give identical results, we obtain

$$Z_{mn,(a)} = Z_{mn,(b)} = Z_{mn,1} + Z_{mn,2} \tag{B.13}$$

$$= \frac{1}{4\pi}\Big[\zeta_1 - \frac{\zeta_2}{k^2\Delta^2} + \frac{1}{\Delta}\sum_{p=1}^{M}w_p(l_p)\Big(l_pS_1(l_p) - \frac{S_2(l_p)}{k^2\Delta}\Big)\Big]. \tag{B.14}$$

Let us now calculate the contribution (c) and (d) to the self-patch. Since our integration axes do not coincide, r now equals

$$r = \sqrt{a^2 + \big(l - (l'\cos\phi + \Delta)\big)^2 + \big(l'\sin\phi\big)^2}. \tag{B.15}$$

For the first term of (B.1) we obtain

$$Z_{mn,1} = \frac{1}{4\pi} \int_{l=0}^{\Delta} \frac{l}{\Delta} \int_{l'=0}^{\Delta} \frac{\Delta - l'}{\Delta} \frac{e^{-jkr}}{r} \, \mathrm{d}l' \, \mathrm{d}l \tag{B.16}$$

$$= \frac{1}{4\pi} \Big[\underbrace{\int_{l=0}^{\Delta} \frac{l}{\Delta} \int_{l'=0}^{\Delta} \frac{\Delta - l'}{\Delta} \frac{e^{-jkr} - 1}{r} \, \mathrm{d}l' \, \mathrm{d}l}_{\eta_1} + \int_{l=0}^{\Delta} \frac{l}{\Delta} \int_{l'=0}^{\Delta} \frac{\Delta - l'}{\Delta} \frac{1}{r} \, \mathrm{d}l' \, \mathrm{d}l \Big] \tag{B.17}$$

$$= \frac{1}{4\pi} \Big[\eta_1 + \int_{l=0}^{\Delta} \frac{l}{\Delta} \Big[\underbrace{\int_{l'=0}^{\Delta} \frac{1}{r} \, \mathrm{d}l'}_{S_3(l)} - \underbrace{\int_{l'=0}^{\Delta} \frac{l'}{\Delta} \frac{1}{r} \, \mathrm{d}l'}_{S_4(l)} \Big] \mathrm{d}l \Big] \tag{B.18}$$

$$= \frac{1}{4\pi} \Big[\eta_1 + \int_{l=0}^{\Delta} \frac{l}{\Delta} \big[S_3(l) - S_4(l) \big] \, \mathrm{d}l \Big]. \tag{B.19}$$

Here $S_3(l)$ and $S_4(l)$ are given by

$$S_3(l) = \ln \Big[\frac{(\Delta - l)\cos\phi + \Delta + \sqrt{a^2 + 2\Delta(\Delta - l)(1 + \cos\phi) + l^2}}{(\Delta - l)\cos\phi + \sqrt{a^2 + (\Delta - l)^2}} \Big], \tag{B.20}$$

$$S_4(l) = \frac{1}{\Delta} \Big(\sqrt{a^2 + 2\Delta(\Delta - l)(1 + \cos\phi) + l^2} - \sqrt{a^2 + (\Delta - l)^2} + (\Delta - l)\cos\phi \cdot \ln \Big[\frac{(\Delta - l)\cos\phi + \Delta + \sqrt{a^2 + 2\Delta(\Delta - l)(1 + \cos\phi) + l^2}}{(\Delta - l)\cos\phi + \sqrt{a^2 + (\Delta - l)^2}} \Big] \Big). \tag{B.21}$$

For the second term of (B.1) we get

$$Z_{mn,2} = -\frac{1}{k^2} \cdot \frac{1}{4\pi} \int_{l=0}^{\Delta} \frac{1}{\Delta} \int_{l'=0}^{\Delta} \frac{-1}{\Delta} \frac{e^{-jkr}}{r} \, \mathrm{d}l' \, \mathrm{d}l$$

$$= \frac{1}{4\pi} \cdot \frac{1}{k^2 \Delta^2} \Big[\underbrace{\int_{l=0}^{\Delta} \int_{l'=0}^{\Delta} \frac{e^{-jkr} - 1}{r} \, \mathrm{d}l' \, \mathrm{d}l}_{\eta_2} + \int_{l=0}^{\Delta} \int_{l'=0}^{\Delta} \frac{1}{r} \, \mathrm{d}l' \, \mathrm{d}l \Big]$$

$$= \frac{1}{4\pi} \cdot \frac{1}{k^2 \Delta^2} \Big[\eta_2 + \int_{l=0}^{\Delta} S_3(l) \, \mathrm{d}l \Big]. \tag{B.22}$$

Combining these two contributions and taking into account that contributions (c) and (d) from Fig. B.1 give identical results, we obtain

$$Z_{mn,(c)} = Z_{mn,(d)} = Z_{mn,1} + Z_{mn,2} \tag{B.23}$$

$$= \frac{1}{4\pi}\Big[\eta_1 + \frac{\eta_2}{k^2\Delta^2} + \frac{1}{\Delta}\int_{l=0}^{\Delta}\Big(\big(l + \frac{1}{k^2\Delta}\big)S_3(l) - lS_4(l)\Big)\,\mathrm{d}l\Big] \tag{B.24}$$

$$= \frac{1}{4\pi}\Big[\eta_1 + \frac{\eta_2}{k^2\Delta^2} + \frac{1}{\Delta}\sum_{p=1}^{M} w_p(l_p)\Big(\big(l_p + \frac{1}{k^2\Delta}\big)S_3(l_p) - l_pS_4(l_p)\Big)\Big]. \tag{B.25}$$

To obtain the complete contribution to Z_{mn}, we have to add all contributions, leading to

$$Z_{mn} = Z_{mn,(a)} + Z_{mn,(b)} + Z_{mn,(c)} + Z_{mn,(d)} \tag{B.26}$$

$$= \frac{1}{2\pi}\Big[(\zeta_1 + \eta_1) + \frac{-\zeta_2 + \eta_2}{k^2\Delta^2} + \frac{1}{\Delta}\sum_{p=1}^{M} w_p(l_p)\Big(l_p\big(S_1(l_p) + S_3(l_p) - S_4(l_p)\big) - \frac{1}{k^2\Delta}\big(S_2(l_p) - S_3(l_p)\big)\Big)\Big]. \tag{B.27}$$

In summary, the self-patch elements Z_{mn} $(m = n)$ of the system matrix are given by:

$$Z_{mn} = \frac{1}{2\pi}\Big[(\zeta_1 + \eta_1) + \frac{-\zeta_2 + \eta_2}{k^2\Delta^2} + \frac{1}{\Delta}\sum_{p=1}^{M} w_p(l_p)\Big(l_p\big(S_1(l_p) + S_3(l_p) - S_4(l_p)\big) - \frac{1}{k^2\Delta}\big(S_2(l_p) - S_3(l_p)\big)\Big)\Big], \tag{B.28}$$

with

$$\zeta_1 = \int_{l=0}^{\Delta}\frac{l}{\Delta}\int_{l'=0}^{\Delta}\frac{l'}{\Delta}\frac{e^{-jkr}-1}{r}\,\mathrm{d}l'\,\mathrm{d}l,\quad r = \sqrt{(l-l')^2 + a^2}, \tag{B.29}$$

$$\zeta_2 = \int_{l=0}^{\Delta}\int_{l'=0}^{\Delta}\frac{e^{-jkr}-1}{r}\,\mathrm{d}l'\,\mathrm{d}l,\quad r = \sqrt{(l-l')^2 + a^2}, \tag{B.30}$$

$$\eta_1 = \int_{l=0}^{\Delta}\frac{l}{\Delta}\int_{l'=0}^{\Delta}\frac{\Delta - l'}{\Delta}\frac{e^{-jkr}-1}{r}\,\mathrm{d}l'\,\mathrm{d}l,\quad r = \sqrt{a^2 + \big(l - (l'\cos\phi + \Delta)\big)^2 + \big(l'\sin\phi\big)^2}, \tag{B.31}$$

$$\eta_2 = \int_{l=0}^{\Delta}\int_{l'=0}^{\Delta} \frac{e^{-jkr}-1}{r}\,\mathrm{d}l'\,\mathrm{d}l,\quad r=\sqrt{a^2+\big(l-(l'\cos\phi+\Delta)\big)^2+\big(l'\sin\phi\big)^2}, \tag{B.32}$$

$$S_1(l)=\frac{1}{\Delta}\Big(\sqrt{a^2+(\Delta-l)^2}-\sqrt{a^2+l^2}+l\ln\Big[\frac{(\Delta-l)+\sqrt{a^2+(\Delta-l)^2}}{\sqrt{a^2+l^2}-l}\Big]\Big), \tag{B.33}$$

$$S_2(l)=\ln\Big[\frac{(\Delta-l)+\sqrt{a^2+(\Delta-l)^2}}{\sqrt{a^2+l^2}-l}\Big], \tag{B.34}$$

$$S_3(l)=\ln\Big[\frac{(\Delta-l)\cos\phi+\Delta+\sqrt{a^2+2\Delta(\Delta-l)(1+\cos\phi)+l^2}}{(\Delta-l)\cos\phi+\sqrt{a^2+(\Delta-l)^2}}\Big], \tag{B.35}$$

$$\begin{aligned}S_4(l)=\frac{1}{\Delta}\Big(&\sqrt{a^2+2\Delta(\Delta-l)(1+\cos\phi)+l^2}-\sqrt{a^2+(\Delta-l)^2}\\&+(\Delta-l)\cos\phi\ln\Big[\frac{(\Delta-l)\cos\phi+\Delta+\sqrt{a^2+2\Delta(\Delta-l)(1+\cos\phi)+l^2}}{(\Delta-l)\cos\phi+\sqrt{a^2+(\Delta-l)^2}}\Big]\Big),\end{aligned} \tag{B.36}$$

where ζ_1, ζ_2, η_1 and η_2 should be calculated numerically.

Overlapping Neighbour-Patch

To calculate contributions to the overlapping neighbour-patch, where the basis- and test functions partially overlap, a similar approach as with the self-patch is adopted. Taking into account symmetry, four new contributions have to be considered. These are seen in Fig. B.2 as AC (up-up), AD (up-down), BC (down-up) and BD (down-down). For contribution BC, l and l' overlap and the calculation of

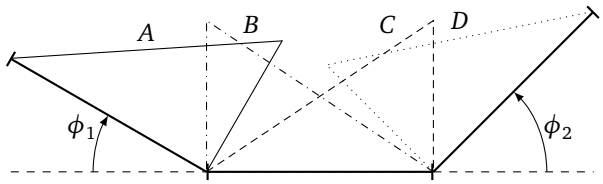

Figure B.2: Configurations for the overlapping neighbour patch (triangles = rooftop functions).

Z_{mn} is performed analytically. The other contributions are calculated numerically.

For the analytical part we use $r = \sqrt{(l-l')^2 + a^2}$. For the analytical contribution BC, the first term of (B.1) equals

$$Z_{mn,BC,1} = \frac{1}{4\pi} \int_{l=0}^{\Delta} \frac{\Delta - l}{\Delta} \int_{l'=0}^{\Delta} \frac{l'}{\Delta} \frac{e^{-jkr}}{r} \, \mathrm{d}l' \, \mathrm{d}l \tag{B.37}$$

$$= \frac{1}{4\pi} \Big[\underbrace{\int_{l=0}^{\Delta} \frac{\Delta - l}{\Delta} \int_{l'=0}^{\Delta} \frac{l'}{\Delta} \frac{e^{-jkr} - 1}{r} \, \mathrm{d}l' \, \mathrm{d}l}_{\chi_1} + \int_{l=0}^{\Delta} \frac{\Delta - l}{\Delta} \int_{l'=0}^{\Delta} \frac{l'}{\Delta} \frac{1}{r} \, \mathrm{d}l' \, \mathrm{d}l \Big] \tag{B.38}$$

$$= \frac{1}{4\pi} \Big[\chi_1 + \int_{l=0}^{\Delta} \frac{\Delta - l}{\Delta} S_1(l) \, \mathrm{d}l \Big], \tag{B.39}$$

where $S_1(l)$ is the same as in the self-patch case. For the second term we obtain

$$Z_{mn,BC,2} = -\frac{1}{k^2} \cdot \frac{1}{4\pi} \int_{l=0}^{\Delta} \frac{-1}{\Delta} \int_{l'=0}^{\Delta} \frac{1}{\Delta} \frac{e^{-jkr}}{r} \, \mathrm{d}l' \, \mathrm{d}l \tag{B.40}$$

$$= \frac{1}{4\pi} \cdot \frac{1}{k^2 \Delta^2} \Big[\underbrace{\int_{l=0}^{\Delta} \int_{l'=0}^{\Delta} \frac{e^{-jkr} - 1}{r} \, \mathrm{d}l' \, \mathrm{d}l}_{\zeta_2} + \int_{l=0}^{\Delta} \int_{l'=0}^{\Delta} \frac{1}{r} \, \mathrm{d}l' \, \mathrm{d}l \Big]$$

$$= \frac{1}{4\pi} \cdot \frac{1}{k^2 \Delta^2} \Big[\zeta_2 + \int_{l=0}^{\Delta} S_2(l) \, \mathrm{d}l \Big]. \tag{B.41}$$

For the total contribution of BC we get

$$Z_{mn,BC} = Z_{mn,BC,1} + Z_{mn,BC,2} \tag{B.42}$$

$$= \frac{1}{4\pi} \Big[\chi_1 + \frac{\zeta_2}{k^2 \Delta^2} + \frac{1}{\Delta} \int_{l=0}^{\Delta} \Big((\Delta - l) S_1(l) + \frac{S_2(l)}{k^2 \Delta} \Big) \mathrm{d}l \Big] \tag{B.43}$$

$$= \frac{1}{4\pi} \Big[\chi_1 + \frac{\zeta_2}{k^2 \Delta^2} + \frac{1}{\Delta} \sum_{p=1}^{M} w_p(l_p) \Big((\Delta - l_p) S_1(l_p) + \frac{S_2(l_p)}{k^2 \Delta} \Big) \Big]. \tag{B.44}$$

The other contributions (AC, AD and BD) are calculated numerically.

References

[1] W. C. Gibson, *The Method of Moments in Electromagnetics*. Chapman & Hall/CRC, 2008, ch. 4, pp. 73–79.

[2] R. Harrington, *Field Computation by Moment Methods*. Krieger Pub Co, 1968.

C
Horn Antenna

The tangential components of the fields in the aperture of a pyramidal horn antenna are given by [1]

$$e_y(x,y) = E_0 \cos\Big(\frac{\pi x}{a}\Big) e^{-jk[\frac{x^2}{2\rho_2}+\frac{y^2}{2\rho_1}]}, \tag{C.1a}$$

$$h_x(x,y) = -\frac{E_0}{Z_{TE,1}} \cos\Big(\frac{\pi x}{a}\Big) e^{-jk[\frac{x^2}{2\rho_2}+\frac{y^2}{2\rho_1}]}. \tag{C.1b}$$

Here, a is the aperture length in the x-direction and b is the aperture width in the y-direction as depicted in Fig. C.1. Furthermore, ρ_1 and ρ_2 are the distance from the phase centers to the aperture of the horn in the E- and H-plane respectively. The characteristic impedance $Z_{TE,1}$ in the aperture is defined as $Z_{TE,1} = \frac{Z_c}{\sqrt{1-(\frac{\lambda}{2a})^2}}$. As the aperture length a is normally chosen large compared to the wavelength λ, in the aperture of the horn antenna the characteristic impedance approximates the characteristic impedance of free space Z_c. Therefore, the approximation $Z_{TE,1} = Z_c$ is sometimes made. The tangential magnetic field $\hat{\mathbf{n}}(\mathbf{r}) \times \mathbf{h}(\mathbf{r})$ over the aperture S can be seen as an equivalent current $\mathbf{j}_S(\mathbf{r})$ generating a vector $\mathbf{N}(\theta, \phi)$:

$$\mathbf{N}(\theta,\phi) = \frac{\mu}{4\pi} \int_S \mathbf{j}_S(\mathbf{r}') e^{j\mathbf{k}\cdot\mathbf{r}'} \, \mathrm{d}\mathbf{r}' \tag{C.2}$$

$$= \frac{\mu}{4\pi} \int_S \hat{\mathbf{n}}(\mathbf{r}') \times \mathbf{h}(\mathbf{r}') e^{j\mathbf{k}\cdot\mathbf{r}'} \, \mathrm{d}\mathbf{r}'. \tag{C.3}$$

Likewise, we can introduce the dual vector $\mathbf{M}(\theta, \phi)$, characterizing the far-field generated by the tangential electric field $\mathbf{e}(\mathbf{r}) \times \hat{\mathbf{n}}(\mathbf{r})$ over the aperture S:

$$\mathbf{M}(\theta,\phi) = \frac{\epsilon}{4\pi} \int_S \mathbf{e}(\mathbf{r}') \times \hat{\mathbf{n}}(\mathbf{r}') e^{j\mathbf{k}\cdot\mathbf{r}'} \, \mathrm{d}\mathbf{r}'. \tag{C.4}$$

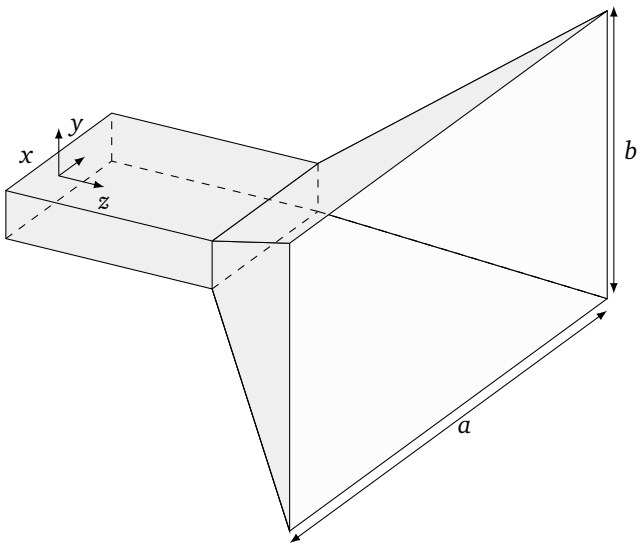

Figure C.1: Pyramidal horn antenna.

The Fourier transform of the electric aperture field and the Fourier transform of the magnetic aperture field are found to be ($\hat{\mathbf{n}} = \hat{\mathbf{z}}$)

$$\begin{aligned}\mathbf{N}(\theta,\phi) &= \hat{\mathbf{y}}\frac{\mu}{4\pi}\int_{x=-\frac{a}{2}}^{\frac{a}{2}}\int_{y=-\frac{b}{2}}^{\frac{b}{2}} h_x(x,y)e^{j\mathbf{k}\cdot\hat{\mathbf{x}}x}e^{j\mathbf{k}\cdot\hat{\mathbf{y}}y}\,\mathrm{d}y\,\mathrm{d}x \\ &= -\frac{\mu E_0}{4\pi Z_{TE,1}}\hat{\mathbf{y}}\int_{x=-\frac{a}{2}}^{\frac{a}{2}}\cos\Big(\frac{\pi x}{a}\Big)e^{j\mathbf{k}\cdot\hat{\mathbf{x}}x}e^{-jk\frac{x^2}{2\rho_2}}\,\mathrm{d}x \\ &\quad\cdot\int_{y=-\frac{b}{2}}^{\frac{b}{2}} e^{j\mathbf{k}\cdot\hat{\mathbf{y}}y}e^{-jk\frac{y^2}{2\rho_1}}\,\mathrm{d}y, \end{aligned} \tag{C.5a}$$

$$\begin{aligned}\mathbf{M}(\theta,\phi) &= \hat{\mathbf{x}}\frac{\epsilon}{4\pi}\int_{x=-\frac{a}{2}}^{\frac{a}{2}}\int_{y=-\frac{b}{2}}^{\frac{b}{2}} e_y(x,y)e^{j\mathbf{k}\cdot\hat{\mathbf{x}}x}e^{j\mathbf{k}\cdot\hat{\mathbf{y}}y}\,\mathrm{d}y\,\mathrm{d}x \\ &= \frac{\epsilon E_0}{4\pi}\hat{\mathbf{x}}\int_{x=-\frac{a}{2}}^{\frac{a}{2}}\cos\Big(\frac{\pi x}{a}\Big)e^{j\mathbf{k}\cdot\hat{\mathbf{x}}x}e^{-jk\frac{x^2}{2\rho_2}}\,\mathrm{d}x \\ &\quad\cdot\int_{y=-\frac{b}{2}}^{\frac{b}{2}} e^{j\mathbf{k}\cdot\hat{\mathbf{y}}y}e^{-jk\frac{y^2}{2\rho_1}}\,\mathrm{d}y. \end{aligned} \tag{C.5b}$$

Taking both contributions into account, the radiation pattern generated by the pyramidal horn antenna is given by

$$\mathbf{F}(\theta,\phi) = j\omega\hat{\mathbf{k}} \times [\hat{\mathbf{k}} \times \mathbf{N}(\theta,\phi)] + j\omega Z_c \hat{\mathbf{k}} \times \mathbf{M}(\theta,\phi). \tag{C.6}$$

Finally, the magnitude of E_0 is obtained via the conservation of power, by stating that the total radiated power of the antenna equals the power transmitted through the aperture of the waveguide:

$$P_{\text{rad}} = \frac{1}{2}\Re \int_S [\mathbf{e}(x,y) \times \mathbf{h}^*(x,y)] \cdot \hat{\mathbf{z}}\, \mathrm{d}x\, \mathrm{d}y \tag{C.7}$$

$$= \frac{|E_0|^2}{4Z_{TE,1}} ab. \tag{C.8}$$

References

[1] C. Balanis, *Antenna Theory: Analysis and Design*. John Wiley & Sons, 2005.